Optical properties of surface plasmon polaritons and semiconductor based quantum system

Von der Fakultät für Maschinenbau

der Gottfried Wilhelm Leibniz Universität

Hannover zur

Erlangung des akademischen Grades

Doktor-Ingenieurin

genehmigte Dissertation

von

MEng. Parva Chhantyal

geboren am 07.08.1986 in Gurja, Nepal

2017

Zusammenfassung

Aktuell ist die Untersuchung der Sensormaterialien ein zukunftstragenden Forschungsthema, die sie sich mit der Fragestellung der Entwicklung von preiswerten- und umweltfreundlichen Sensoren beschäftigt. Die Suche nach geeigneten Materialien befasst sich mit Herausforderungen der Miniaturisierung der Sensoren und dennoch deren effizienterer Leistungsfähigkeit. Der Fokus dieser Arbeit liegt auf der Untersuchung der optischen Eigenschaften der Materialien mit dem Ziel diese Materialien in ferner Zukunft als Sensoren einzusetzen. Die Ergebnisse dieser Arbeit können ferne für ein breites Spektrum an Sensoren angewendet werden. Die optischen Eigenschaften der Sensormaterialien werden in dieser Arbeit durch zwei verschiedene Techniken untersucht; (i) durch Oberflächen-Plasmon-Polaritonen (SPPs) auf metallischen Filmen und (ii) Anregung von Halbleiter-Nanopartikeln (NPs).

Die SPPs, die auf den metallischen Filmen oszillieren, haben die Fähigkeit, sich entlang der Oberfläche zu propagieren, bis sie von den Metallen absorbiert werden. Allerdings ist aufgrund der Insuffizienz der SPPs-Progagationslänge die Leistung der plasmonischen Geräte begrenzt. Die Untersuchung von SPPs und deren Progagationslänge (L_{SPP}) auf polykristallinen Metallfilmen (Gold- und Silber) erfolgte im Rahmen dieser Arbeit in Bezug auf die Herstellungsprozesse der Metallfilme. Ferne beschäftigt sich diese Arbeit mit Verwendung von Halbleiter-Nanopartikeln als Sensormaterialien. Dünne Schichten unterschiedlicher quantisierter Halbleiter-NPs wie Quantenpunkte (QDs), Quantenstäbe (QRs) und Quantenmulden (NPLs) wurden hergestellt und mittels Fluoreszenz- und Emissionsspektroskopie charakterisiert. Die optischen Eigenschaften wurden in Abhängigkeit der Größe und Morphologie der NPs sowie des verwendeten Lasersystems untersucht. Außerdem wurde der Temperatureinfluss auf die optischen Eigenschaften der bestmöglichen NPs untersucht.

Zusätzlich wurde eine Methode zum Einbetten der NPs in ein Polymer entwickelt, um die NPs stabil zu halten und für die additive Fertigung praktikabel zu machen. Abschließend wurden metallische Filme und Halbleiter-NPs als Sensormaterialien für die Applikationen bei den kleinen und großen Sensoren untersucht.

Schlagworte: Oberflächen-Plasmon-Polaritonen, Halbleiter-Nanopartikeln, Laser

Abstract

Sensor materials are the fascinating investigative subjects in response to the demand of affordable and environmentally favourable sensors. The analysis on these materials also confronts crucial challenge raised in miniaturising sensors with yet efficient outcome. This thesis focuses on investigating optical properties of the materials with a conclusion to understand their abilities as sensors in remote future. Upon accomplishing this concept, their applications can be broadened, that is adaptable into the wide range of small and large scale sensors. The optical properties are investigated by two different techniques; (i) through surface plasmon polaritons (SPPs) on metallic films and (ii) excitation of semiconductor nanoparticles (NPs).

The SPPs, oscillating on the metallic films have an ability to propagate along the surface until they are absorbed by the metals. However, due to insufficiency in SPPs length, the performances of the plasmonic devices are limited and practically challenging for recent technologies. The study of SPPs and their propagation length (L_{SPP}) on polycrystalline metals (gold and silver) films is performed with respect to evaporation and sputtering deposition approaches on the glass substrates.

To enhance the scope further into the waveguide, and considering the convenience of using alternative pumping sources and system , this thesis investigates possibility of semiconductor NPs as sensor materials. The continuous films of different quantised semiconductor NPs, such as quantum dots (QDs), quantum rods (QRs) and quantum wells (NPLs) are produced, and a fluorescence and emission spectra are measured. The optical properties are evaluated based on the sizes and morphology of the NPs as well as the laser system adopted. Afterwards, the temperature influence on the optical properties of the best performing NPs is investigated.

Furthermore, a method to embed NPs into polymer to make these NPs stable and practical for additive manufacturing is generated. In conclusion, metallic films and semiconductor NPs are investigated as sensor materials in the prospective media of small and large-scale sensors.

Keywords: Surface plasmon polaritons, semiconductor nanoparticles, Laser

Table of contents

List of figures

List of tables

Nomenclature

Physics Constants

$m*_e$ Effective mass of electron, 1.18×10^{-31} kg

$m*_h$ Effective mass of hole, 4.09×10^{-31} kg

c   Speed of light, $299,792,458 \ ms^{-1}$

e   Euler's number, 2.71828183

h   Plank's constant, $6.63 \times 10^{-34} \ m^2\text{kg}s^{-1}$

Chemistry Abbreviations

SiO_2 Silicon dioxide

CdS   Cadmium Sulphide

CdSe   Cadmium Selenide

Cr   Chromium

D-H_2O   Deionised water

EG   Ethylene Glycol

GaN   Gallium nitride

HCL   Hydrochloric acid

IR   Irgacure

MAPTMS   Methacryloxypropyltrimethoxysilane

MMA   Methyl Methacrylate

ORMOCER'S Organically modified ceramics

ORMOSIL Organically modified Silica

PI   Photoinitiator

PMMA poly(methyl methacrylate)

ZnS   Zinc Sulphide

ZPO   Zirconium n-proxide

Other Abbreviations

Ag^E Evaporated Silver

Ag^S Sputtered Silver

AR   Auger recombination

ASE   Amplified Spontaneous Emission

ATR   Attenuated-Total-Reflection

Au^E Evaporated Gold

Au^F Atomically flat Crystalline Gold Flakes

Au^S Sputtered Gold

FIB   Focused Ion Beam

FRET Fluorescence Resonance Energy Transfer

FWHM Full Width Half Maximum

L_{SPP} Propagation Length

LD   Lorentz-Drude model

LRM Leakage Radiation Microscopy

LSPRs localised surface plasmon resonance

ML   Monolayers

MPP Microscope Projection Photolithography

Nd:YAG Neodymium-doped yttrium aluminium garnet

NPs   Nanoparticles

PAu^F Poly-crystalline gold flakes

PL   Photoluminescence

QDs   Quantum dots

QRs   Quantum rods

QWs   Quantum wells

QY   Quantum Yield

rcf   Relative Centrifugal Force

RPM   Revolution per minute

rps   Revolution per second

SPPs   Surface plasmon polaritons

Ti:Sa   Titanium:Sapphire

Chapter 1

Introduction

1.1 Nanotechnology

'What would happen if we could arrange the atoms one by one the way we want them?' [1]

In 1959, noble prize winner Physicist, Richard Feynman asked the question above to the audience while he was giving a lecture called 'Plenty of room at the bottom' [2] at the meeting of American Physical Society [3]. The lecture focused on possibility of adjusting size of a material to achieve required properties. However, it was not until late 20th century that the importance of nanoparticles (NPs) with size ranging from 1 to 100 nm was accomplished in the research.

The word "nano" derived from the Greek word "nanos", meaning "dwarf" was first used by Professor Norio Taniguchi [4] in 1974. Later, Dr. K.E. Drexler familiarised the word in his book; Engines of creation: the coming era of nanotechnology in 1986 [5]. Since then, 'Nanotechnology' has been popularly categorised in the field of modern science.

A nanometer is a billionth of a meter. The concept of nanotechnology field is to manipulate a matter in an atomic and molecular scale. The precise manipulation and accomplishment of desired properties possess the technological goal of fabricating products in nano and microscale. In addition to this, the field nanotechnology also focuses in engineering the functional systems at the molecular scale. As the particle size decreases, their area to volume ratio increases [6]. This results in greater quantity of atoms to expose to the surface. Due to the fact that the chemical reactions occur at the surfaces, small NPs will be much more reactive in comparison to larger particles.

The Lycurgus cup [7], 4th century Roman glass, shown in Fig.1.1 represents the remarkable aspects of the nanotechnology. The cup shows green colour (Fig.1.1(a)) when it reflects the light, but red (Fig. 1.1(b)) when transmits. This effect, known as the dichroic effect is

achieved by dispersing small amount (ppm) of gold and silver NPs in colloidal form in glass. This idea opens the way to captivate the fact that change in the size and composition of the NPs can manipulate the properties of materials. This property is regarded as highly significant in many fields, such as in terms of investigating the behaviour of light in the nanoscale.
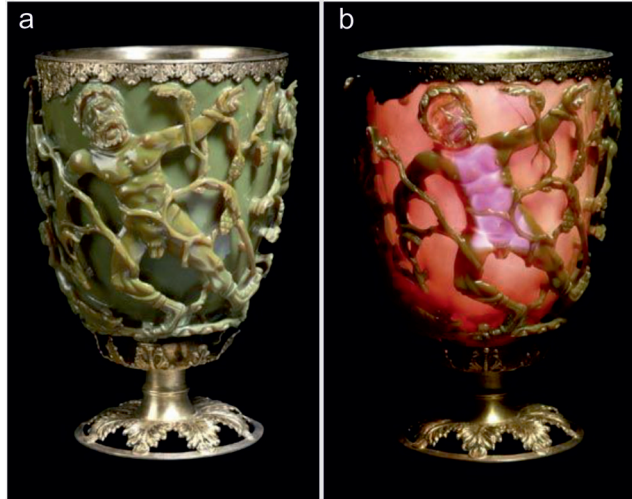
Fig. 1.1 Demonstration of (a) Reflected light and (b) Transmitted light through the Lycurgus cup [7]. The gold component being mainly responsible for the reddish transmission and the silver for the green reflection.

1.2   Surface plasmon polaritons

A plasmon is an oscillation of free electrons in matter with respect to fixed positive ions. When an electromagnetic wave hits the electron clouds around the lattice of positive ions, the conductive electrons are impelled by the electric field. As a result, they oscillate coherently at their resonant frequency relative to positive ions. This phenomena determines the optical properties of metals. Most metals and semiconductors have plasmon frequency in ultraviolet region, which means the incident light is absorbed [8]. Due to this, the visible range can be reflective.

Surface plasmon polaritons (SPPs) are the electromagnetic excitation that consists of a surface plasmon and a photon, and exists on the surface of the metals [9]. As shown in Fig. 1.2, when the momentum of an incoming photon (hv) matches with the momentum of SPPs [10], they are excited. Due to the fact that relative permittivity of a metal is normally larger than that of dielectric medium (air in this case), SPPs field has a shorter penetration depth in a metal in comparison to adjacent dielectric [9]. The dispersion curve [10] for the SPPs suggest that a defect is needed for incoming photons to upgrade its momentum and match with the exciting electrons. Consequent to this circumstances, the electromagnetic waves propagate along a dielectric-metal interface while decaying exponentially into both the neighbouring media [10–14].
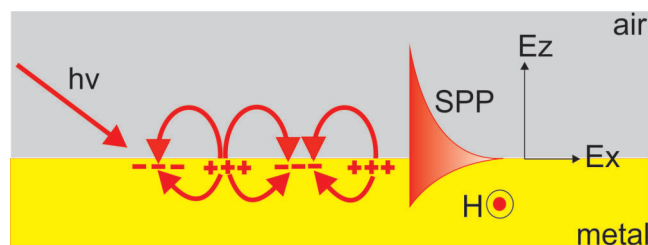
Fig. 1.2 The surface plasmon polaritons on metal film interface. The incoming photon (hv) hits the electron cloud. The electrons oscillate and propagate along the surface until the energy is damped.

1.3   Semiconductor nanoparticles

Semiconductor NPs with size less than 10 nm are of great interest due to their quantum confinement properties [15]. In contrast to the continuous absorption spectrum of a bulk semiconductor, the size confined NPs have discrete absorption spectrum in valence and conduction bands. This spectrum is susceptible to the size and becomes more discrete with decrease in size. Another consequence of the confinement effect is an increase in the energy levels. According to the Brus equation [16], the energy band gap of small spherical QDs is proportional to $1/R^2$, where, R is the radius of the particle. This effect of the quantum confinement endorses a significant influence on introducing new properties to the materials by tuning their size and composition [15, 6].

When the materials are in nanometer size, their physical and chemical properties differ incomparably from those of the atomic-molecular of the same composition [17]. As the size of the NPs decreases, their surface/volume ratio increases [15, 6]. Table 1.1 illustrates the influence of the surface area as their size decreases, demonstrated by Fig. 1.3.
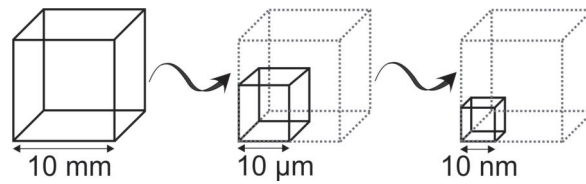
Fig. 1.3 The size dependent change in surface area of a cube. As the size of the cube decreases from 10 mm to 10 nm (left to right), the area increases with respect to the original size.

Table 1.1 The size dependent change in surface area and number of cubes (considering the same material mass).

Size	Number of cubes	Total Area/m^2
10 mm	1	$6x10^{-4}$
10 μm	10^9	0.6
10 nm	10^{18}	600

The concept, adapted from [18] is to visualise a cube that has a size of 10 mm. It has a total surface area of $6x10^{-4}$ m^2. When the length of this cube is decreased to 10 μm, considering the same material mass, the total of 10^9 cube can be integrated with respect to the original cube. This provides a total area to be 0.6 m^2. Furthermore, when the length is decreased to 10 nm, the area of the total cubes can be increased to 600 m^2 with the total of 10^{18} cubes. This effect provokes the dominance of the surface properties, such as surface interaction, interfacial and agglomeration. As a result, dangling bonds that have higher energy

are exposed to their surface. The efficient use of these dangling bond to alter the material properties endorse huge advantage in telecommunication, solar cells, nanoscale electronic devices, laser technology, waveguide, chemical, sensors, photonic and medical applications [19].

In addition, the properties of NPs can be further modified according to the need by embedding them into a dispersible polymer. This procedure makes the materials more stable and adaptable to the surrounding. Depending on size, shapes and chemical nature of NPs, following polymer/NPs properties can be modified [6];

- Electrical and thermal conductivity

- Thermal stability

- Mechanical properties: stiffness, Young's modulus, fatigue

- Chemical properties: reactivity, solubility, density

- Physical properties: magnetic, optic, dielectric constants

This dissertation was carried out within the framework of ***hsn-energy***[1], which emphasises on the field of nanotechnology by focusing on the solution to ever-increasing demand for energy. The aim of the subproject *Nanoparticles for Enhanced Photovoltaics, Nanoheating and Sensors* is to understand nanomaterials and their engineering ability with regards to developing existing or inventing new applications.

The investigations presented in this thesis deal with improving fundamental energy process at nano and micro-scale. The main properties of metal and semiconductor NPs; their resonant responses to a reaction on external optical fields, concentrating energy inside and around the particles, making them very attractive for different practical applications, such as sensor technology and efficiency enhancement in photovoltaic devices. In this work, different types of metals and semiconductor NPs, with different confinement and morphology is studied by use of different lasers, in continuous or pulsed system. The outcome will be generalised with respect to their possible future applications in sensing.

---

[1]The research project *hsn-enegry* is granted by the Hannover School for Nanotechnology (HSN).

Chapter 2

State of the art and theory

The recent progress in nanotechnology is an impulse to replace slow electronic devices with fast photonic mechanism [9]. Such branch of nanotechnology is called nanophotonics. This technology requires efficient advancement of an optical analogue that is capable of controlling and processing optical signals. It also expands the study of plasmonic properties of the materials, broadening the technology into exciting new area by merging favourable properties between faster electronics and smaller photonics. The improved photonic circuits will be applicable for carrying optical signals and electric currents faster in quantised circuits [20]. The study of these approaches to photonic integration are based on so-called surface plasmons optics [9], which will be described more in detail in *Section 2.1*.

Another development in the field of Nanotechnology is the evolution of electronic devices based on semiconductor NPs, such as quantum dots (QDs), quantum rods (QRs) and quantum wells (QWs) [9]. This branch of nanotechnology, known as nano-materials studies the behaviour of the materials in nanoscale [3]. The alteration of material properties with respect to their sizes, and use of those properties in different applications is the key focus of this branch. The materials, structured at the nanoscale remarkably have unique optical, electronic, or mechanical properties that are very useful in an application of highly sensitive sensors.

2.1   Properties of surface plasmon polaritons

'I was astounded to find that under certain conditions, the drop from maximum illumination to minimum, a drop certainly of from 10 to 1, occurred within a range of wavelengths not greater than the distance between the sodium lines'- Wood 1902

The phenomena of SPPs were first discovered by Wood in 1902 when he witnessed the spectrum of a continuous light source, diffracted by metallic gratings [21]. However, the evanescent electromagnetic fields were discovered by Newton in 1704 when he brought a prism in contact with convex lens to bend light by total internal reflection [22]. In latter stage, the study of electromagnetic properties of metallic NPs at metal-dielectric interfaces played an enormous interest in science since the works of Gustav Mie [23].

After the work of Wood [21], Zenneck and Sommerfeld demonstrated theoretically that the surface electromagnetic waves appear at the border of two different dielectric medium [24, 25]. In 1936, Fano proposed that surface electromagnetic waves were accountable for the irregularities in the diffraction spectra of metallic gratings [26]. Since then, SPPs are widely recognised in the field of surface science. However, it was only in 1957 when Ritchie predicted the characteristics of an energy loss by electrons by investigating the impact of film boundaries on the production of collective excitations [27] The presence of these excitations are demonstrated by Powell and Swan [28], which was later named as the surface plasmons by Stern and Ferrell [29].

One of the most promising aspects of SPPs is an ability to focus and lead the electromagnetic waves using nanostructures [12], opening concept to many applications across many fields, such as spectroscopy [30], nanophotonics [31–33], circuits [34, 35], imaging [36] and biosensing [37]. This opens the way of adopting SPPs based waveguides [38–41] to guide the light energy beyond diffraction limit [42, 43]. This is generally advantageous while miniaturising chip photonic circuits at a nanoscale since the traditional photonic devices is susceptible to diffraction limit. However, due to the fact that the Ohmic losses is high, these kind of arrangements also face some challenges. This complication encourages investigating possible ways to increase propagation length (L_{SPP}) of SPPs to compensate the losses.

To understand the properties of SPPs, it is important to discuss some key theories related to SPPs.

2.1.1 Dispersion relation

The magnetic field in SPPs wave is parallel to the surface and perpendicular to the propagation direction, whereas the electric field is perpendicular to the surface and parallel to the propagation direction [20]. To achieve the condition for excitation of SPPs on metal surface, the interface with two materials with different dielectric properties, consisting of both positive and negative permittivity are supposedly considered [44]. Metal such as gold and silver are good examples that has a negative real part of permittivity in optical range while a dielectric is opted due to its positive permittivity. Using Maxwell equations, the dispersion relation of the SPPs can be derived [10], that provides essential information regarding the properties of the SPPs. The schematic result of the dispersion relation of SPPs on flat surface is shown in Fig. 2.1.
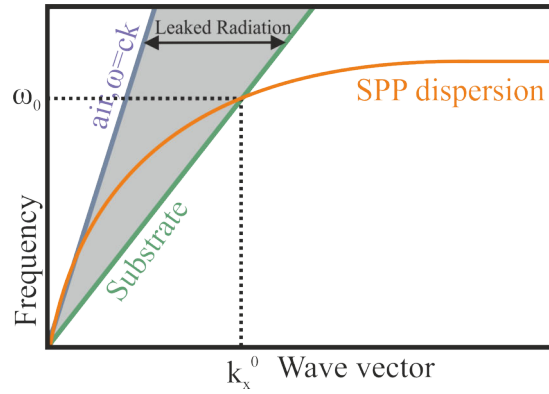
Fig. 2.1 The dispersion relation of SPPs shows the air line (blue), substrate line (green) and the SPPs line (orange). The grey part (in cone shape) represents the area where SPPs lose energy via leakage radiation. Here, ω_0 is the resonant frequency, k_x^0 is the resonant wave vector.

For visible light, once the frequency reaches to the limiting value, explained by frequency of SPPs (ω_0), the dispersion curve bends the right side of the light line. At these point, the SPPs can be excited by p-polarised light when wave vector of photon in dielectric is equal to the wave vector of SPPs (shown by dotted line).

The condition of SPPs in terms of the chosen materials is satisfied when; Re[ε_2]<0, ε_1>0, where ε_1 is the dielectric constant of dielectric part and ε_2 is the dielectric constant of the metal part. These dielectric constants, related with wave-vector expression of the p-polarised electric field, propagating along the surface is given by: $k_{SPP} = k'_{SPP} + ik''_{SPP}$, where, the real

and imaginary parts of k_{SPP} vectors are related by,

$$k'_{SPP} = \frac{\omega}{c} \sqrt{\frac{\varepsilon'_2 \varepsilon_1}{\varepsilon'_2 + \varepsilon_1}} \tag{2.1}$$

and

$$k''_{SPP} = \frac{\omega}{c} \left(\frac{\varepsilon'_2 \varepsilon_1}{\varepsilon'_2 + \varepsilon_1} \right)^{3/2} \frac{\varepsilon''_2}{2(\varepsilon'_2)^2} \tag{2.2}$$

where, ω is the frequency of incoming light and c= 299,792,458 ms^{-1} is the speed of light in vacuum.

2.1.2   Dielectric constant of metal

In order to study SPPs on metal surface, this thesis considers a classical semi-infinite approach, which consists of two infinite media, separated by a planar interface. The two media are a dielectric medium and a metal. In spite of being considered as the plasmonic materials [45], gold and silver are restrained by their absorption properties, described by the electromagnetic field dependent dielectric constant (equation 2.3).

$$\varepsilon = \varepsilon^i + i\varepsilon^{ii} \tag{2.3}$$

The imaginary part (ε^{ii}) of the dielectric constant represents absorption, denoting ohmic losses. The real part (ε^i) on the other hand illustrates the propagation of waves from the film surface. The frequency dependent dielectric constant is associated with the refractive index of the material by the following formula:

$$\varepsilon^i = (n^2 - k^2), \varepsilon^{ii} = 2nk \tag{2.4}$$

Here, 'n' is the refractive index, which is responsible for the dispersion in the medium and the imaginary part 'k' represents the absorption coefficient.

   The wavelength dependent dielectric function of the free electrons is described by the Drude model [46, 47] (equation 2.5). The model considers the assumption of metal with a mass of positively charged ions, with number of free electrons around. When the external electromagnetic field is applied to this electron cloud, the electrons oscillate at their resonant frequency and collide with lattice phonons. The theory is later improved by considering inter and intra band transitions inside the metal due to external field, explained by equation 2.7.

This theory is commonly known as Lorentz-Drude model (LD) [48, 49].

$$\varepsilon(\omega)_{LD} = \varepsilon(\omega)_D + \varepsilon(\omega)_L \qquad (2.5)$$

where,

$$\varepsilon(\omega)_D = 1 - \frac{\Omega_p^2}{\omega(\omega - i\gamma_0)} \qquad (2.6)$$

$$\varepsilon(\omega)_L = \sum_{j=1}^{k} \frac{f_j \omega_p^2}{(\omega_j^2 - \omega^2) + i\omega\gamma_j} \qquad (2.7)$$

In equations (2.5-2.7), ω_p is the plasma frequency, k is the number of oscillators with frequency ω_j, f_j is the strength, $1/\gamma_j$ is the lifetime, $\Omega_p = \sqrt{f_0}\omega_p$ is the plasma frequency associated with intraband transitions with oscillator strength f_0 and damping constant γ_0.

Fig. 2.2 represents the real (a) and imaginary (b) parts of dielectric functions of gold, obtained from experimental values of [50] (blue dots), [51] (red dash) and [52] (green), and fitted with theoretical values of the LD. The experiment carried out by [50] consist of prepared metal films on quartz substrates by vacuum evaporation at the rate of $\approx$60 Å/sec at room temperature. The materials used were 99.9% pure metals and were evaporated at pressures below 4x 10^{-6} Torr. The optical constants were calculated by measuring reflection and transmission measurements on the films. On the other hand, [51] used the refractive index values of the gold from [53] and silver's from [54]. The metals have purity of over 99.99 %. The gold films were prepared by evaporating onto fused silica substrates in ultrahigh vacuum (10^{-10}-10^{-11} Torr). Afterwards, the samples were annealed from 100°C to 150°C. The silver on other hand were electrolytically and chemically polished, followed by vacuumed annealing at 700 K for more than four hours. The optical constants were obtained by using polarimetric method. Finally, the samples from [52] were prepared by evaporating in an electron-beam evaporator at an average rate of 0.6 nmmin^{-1}-0.1 nms^{-1} at a base pressure of 2.7×10^{-4} Pa. Post annealing was avoided in this case.
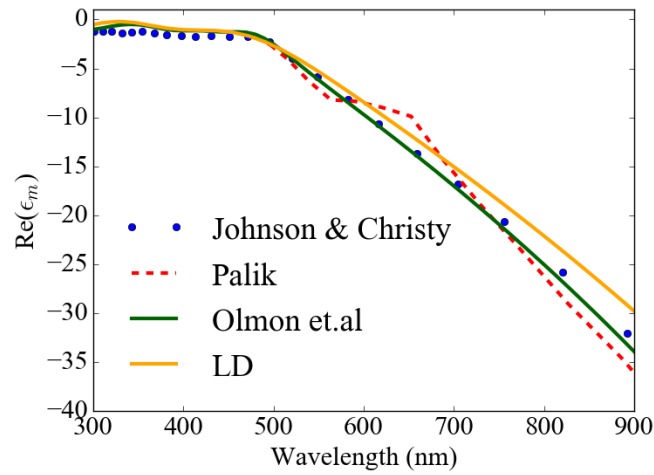
(a) Real part
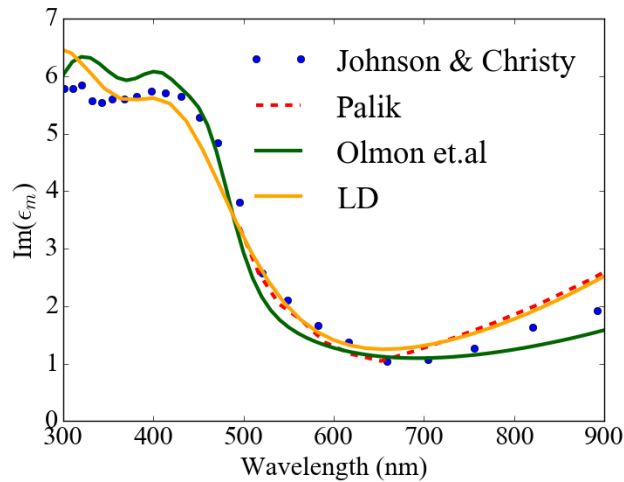
(b) Imaginary part

Fig. 2.2 Experimental values of real (a) and imaginary (b) parts of dielectric constants of gold, taken from [50] (blue dots), [51] (red dash) and [52] (green). They are labelled as Johnson & Christy, Palik and Olmon et.al, respectively. The yellow line represents the calculated values from the LD.

For real dielectric functions, the values from [50] and [52] are closely related to each other. The data from [51] shows slight variation after ≈560 nm although it crosses briefly with other data at around ≈725 nm again. For imaginary dielectric functions, all data are close to each other in between 450 nm and 650 nm. Outside this range, the data show disagreement. Beyond 650 nm, the differences in values increase as the wavelength increases. The disagreement in the sets of data may have come from the method of preparation. The real part of LD values give close approximation with other experimental data until ≈500 nm.

After this, the differences in data increases though value from LD and [51] cross each other briefly at 600 nm and 700 nm. The imaginary part of LD demonstrates good correlation with [50, 51]. The calculation parameters for the LD model for both gold and silver are given in appendix A.1.
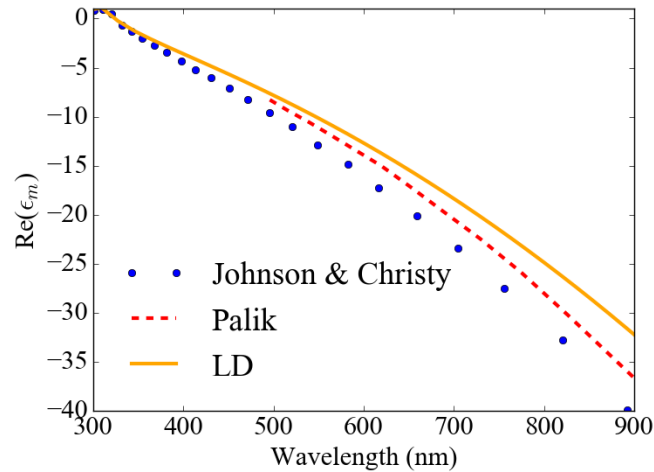
(a) Real part
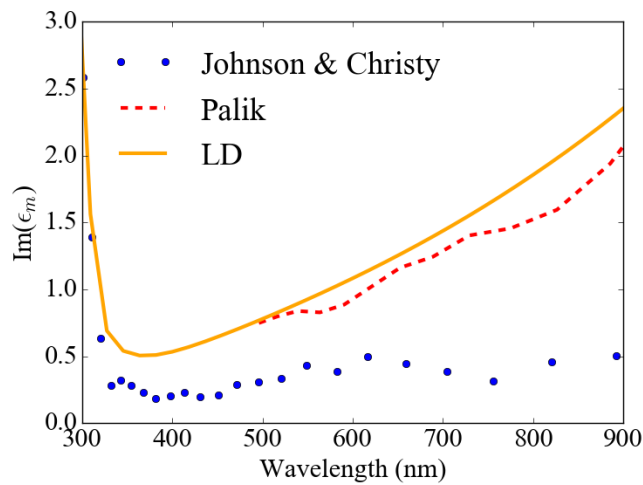
(b) Imaginary part

Fig. 2.3 Real (a) and imaginary (b) dielectric constants of silver, taken from [50] (blue dots) and [51] (red dash). They are labelled as Johnson & Christy, Palik and Olmon et.al, respectively. The yellow line represents the calculated values from the LD.

The dielectric functions of silver is approximated with the experimental data from [50] (blue dots) and [51] (red dash) only, and compared with theoretical data from the LD, as shown in Fig. 2.3. For real part of dielectric functions, the values from all three references

seem to diverse from each other as the wavelength increases. The imaginary data however showed huge deviation. The data from [51] has higher absorption than [50]. There is a slight overlap between [50] and values from LD until around 350 nm. Afterwards, LD model seems to provide values closer to [51] in comparison to [50]. So, it can be expected that in the case of [50], the SPPs will propagate longer. In comparison between gold and silver, lower absorption effect is observed in silver.

2.1.3 Excitation methods

The interaction of the electromagnetic wave with surface charges leads to the increase in the momentum of SPPs in comparison to the free-space photon of same frequency. Hence, SPPs in an ideal semi-infinite medium surface cannot be excited. In order to achieve an excitation of the SPPs, their momentum must match with the momentum of the incoming photon. At the exciting phase, since the momentum of SPPs is greater than the incoming photon, this inequality has to be conquered by upgrading the momentum of the light at impact point. There are several methods to generate this irregularities experimentally in order to assess SPPs. These methods are shown in Fig. 2.4.
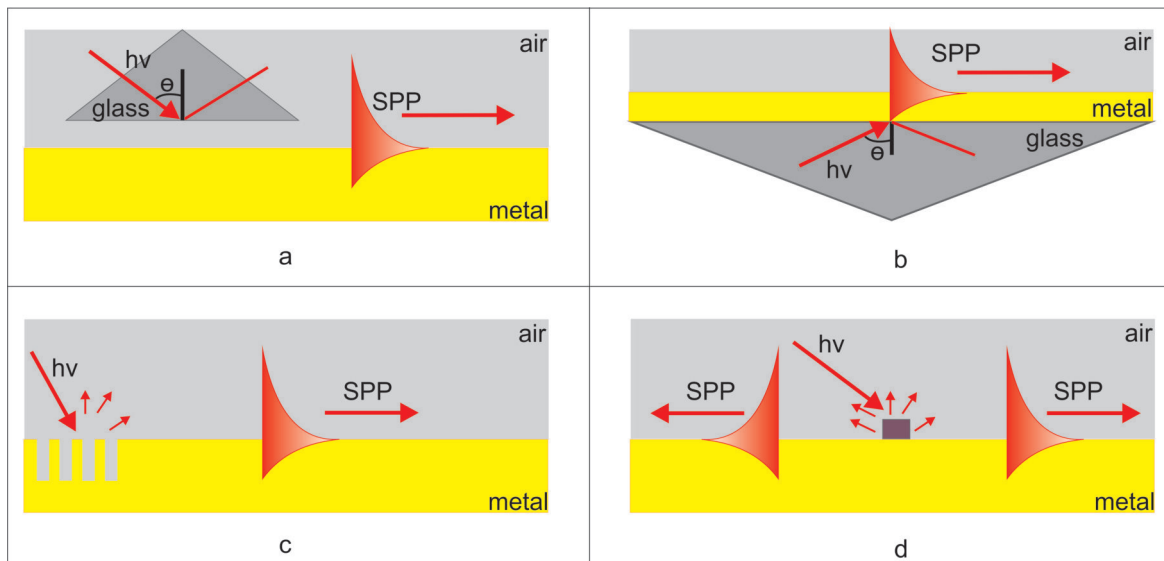
Fig. 2.4 Some examples of the evaluation methods of SPPs, such as (a) Otto Configuration, (b) Kretschmann-Raether Configuration, (c) Groove-Coupling Method and (d) Grating-Coupling Method.

- 2.4(a) Otto Configuration: The method, Attenuated-Total-Reflection (ATR) was first introduced by Otto in 1968 [55]. This sophisticated method couples the electromagnetic

waves to surface at optical frequencies. If certain conditions are met, the optical light enters a prism, made of a high refractive index infrared transmitting material (ATR crystal) and is reflected internally as shown in the figure. This reflectance wave creates an evanescent wave, which extends beyond the surface of the crystal into the sample. In regions of the infrared spectrum where the sample absorbs energy, the evanescent wave will be attenuated. In order to obtain the total internal reflection, the angle of incident radiation must be greater than the critical angle [9]. The advantage of this technique is that the intensity of the wave decays exponentially with distance from the surface of the ATR crystal. The distance between the metal surface and the crystal is normally in the order of microns, which makes this technique typically insensitive to sample thickness. As a result, this method can be applicable for investigating thick metals or strong absorbing materials [9].

- 2.4(b) Kretschmann-Raether Configuration: The ATR method was further improved by Kretschmann and Raether [56]. In this configuration, the metal film is deposited on top of a glass prism as shown in figure. The film is illuminated through dielectric prism at an incidence angle, θ where the in-plane component of the photon wave vector in the prism coincides with SPPs wave vector on an air/metal surface, and light is coupled to SPPs. Under these conditions, a sharp minimum is observed in the reflectivity at the angle at which the light can be coupled to SPPs with almost 100% efficiency. The SPPs on an interface between the prism and metal cannot be excited in this geometry as the wave vector of SPPs at this interface is greater than the photon wave vector in the prism at all angles of incidence. To excite SPPs on this interface, thin dielectric materials should be deposited in between. In such system, SPPs modes on both the surface and the interface can be excited. This method is usually applicable for investigating thin metals.

- 2.4(c, d) Groove-coupling and Grating-coupling Method: The SPPs excitation mechanism can be simplified further by using grooves (Fig. c) or gratings (Fig. d) instead of ATR. The mismatch in wave vector between the in-plane momentum of incoming photons and the SPPs can be overcome by using diffraction effects at a grating or grooves patterns on metal surface. They can be synthesised using different techniques, such as photolithography, e-beam lithography or focused ion beam (FIB). In the case of grooves, when they are significantly deep, compelling changes to the SPPs dispersion relations occur. In the case of gratings, the SPPs photonic bandgap is formed when the grating period is equal to half the wavelength of the SPP.

In this thesis, the assessment of SPPs L_{SPP} was carried out based on measuring exponentially decayed plasmons at different distances until the SPPs are absorbed completely. Considering this concept, this thesis considers gratings and grooves at specific chosen distances as to in-couple and out-couple light.

2.1.4 Propagation length

Once SPPs are excited, they have tendency to propagate along the ideal flat metal surface until their energy is being absorbed into the metal. The L_{SPP} is defined as the distance at where the SPPs intensity decays by a factor of 1/e, where e= 2.71828183. This condition is satisfied at a length, L_{SPP} [57, 10];

$$Ł_{SPP} = \frac{1}{2k_{SPP}^{''}} \tag{2.8}$$

where, $k_{SPP}^{''}$ is the imaginary part of k-vector, and is given by equation 2.2.

The L_{SPP} can also strongly depends on film quality, which is expected to be influenced by the fabrication methods [58]. By changing the deposition methods, the dielectric constants of the metals can be tuned, hence accomplishing enormous impact on optical properties of the metals. Depending upon the working condition, the film preparation methods can also introduce some dislocation [59], again strongly influencing material properties. The properties of the film, such as topography, thickness uniformity [59], crystal size distribution [60], porosity [61] and morphology [62] have previously received considerable attention for the investigation. Previous study of sputtering process has demonstrated that the sputtering process produces rough films, containing the mixture of polycrystalline or amorphous or combination of both [63, 64]. A comparative study between the properties of sputtered and evaporated, gold and silver films showed better film qualities with evaporation technique [59]. The evaporated film mostly contained wide range of crystal sizes. In contrast, crystal sizes were much more closely grouped in the sputtered film [59]. According to the group Hnatowicz [65], when the gold films are more than 10 nm thick, both evaporation and sputtering methods showed continuous and homogeneous surface, but their crystals shaped different. The evaporation developed round clusters whereas sputtering technique developed smaller but pointed clusters. These clusters have potential to develop porosity, generating both ohmic and scattering losses [62].
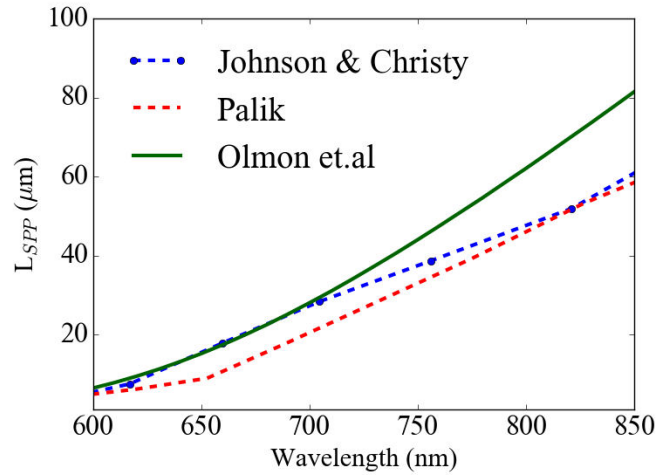
(a) Gold
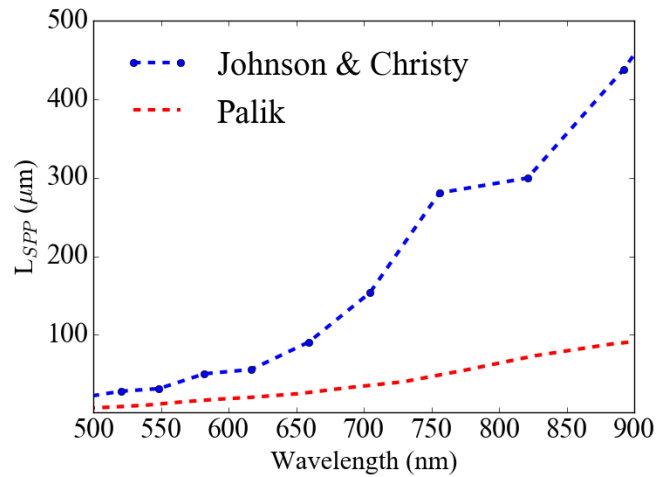
(b) Silver

Fig. 2.5 Theoretical propagation lengths, taking the dielectric constants from [50], [51], [52] for Gold (a), and [50], [51] for Silver (b). The references are labelled as Johnson & Christy, Palik and Olmon et.al, respectively in the graphs.

The L_{SPP} of bulk gold films with respect to the dielectric constants from [50], [51] and [52] is shown in 2.5(a). It can be observed that the data from [52] (green) contributes the longest L_{SPP} throughout the visible and near infrared wavelength range on gold films. This corresponds to the Fig. 2.2(b), where the data from [52] provides the lowest absorption effects. Similarly, the data from [50] (Johnson & Christy, blue dots) completely overlaps with [52] (Olmon et.al, green) until about 700 nm, after which it diverges and touches the data

from [51] (Palik, red dots) at around 825 nm. Overall, the data taken from Palik provides the shortest L_{SPP}.

On the other hand, the theoretical L_{SPP} of bulk silver films with respect to the dielectric constants from [50] and [51] is shown in 2.5(b). The bulk silver films represent huge divergence in the L_{SPP}. It can be observed from the figure that values from [50] (Johnson & Christy) estimated longest L_{SPP} throughout the range. This again corresponds to Fig. 2.3(b), which represents lowest absorption effects.

It can be observed that the L_{SPP} of SPPs increases with an increase in the wavelength. In comparison to gold, silver has higher L_{SPP} due to lower absorption. The L_{SPP} values are shown in Table 2.1.

Table 2.1 Theoretical values of surface plasmon polaritons propagation length for He-Ne laser (633 nm).

Metal	L_{SPP}	Dielectric constants taken from
Gold	$\approx$10 μm	[50]
	$\approx$7 μm	[51]
	$\approx$11 μm	[52]
Silver	$\approx$65 μm	[50]
	$\approx$22 μm	[51]

A recent research [66] has presented an innovative approach to amplify SPPs efficiently under electrical pumping without any loss. Another group has investigated the propagation of SPPs gold film dependent on the surface roughness [67]. In this research, the L_{SPP} was calculated for the gold and silver in the broad wavelength range. Experimentally, they demonstrated the L_{SPP} on 47 nm thick gold films at the excitation wavelength of 633 nm and 805 nm, using the Kretschmann-Raether configuration (*Section 2.1.3, 2.4b*). Their measurement showed 3.4 μm for 633 nm and 15 μm for 805 nm. This calculation was done taking into an account of roughness. Without a roughness, 4.4 μm, 3.7 μm and 2.7 μm were calculated at the wavelength of 633 nm, whereas 23 μm, 14 μm and 24 μm were calculated at the wavelength of 805 nm, considering the dielectric constants from [68, 69, 51], respectively. Their observations are listed in the Table 2.2 [67].

Table 2.2 Theoretical and experimental values of surface plasmon polaritons propagation length depending on roughness.

Wavelength	Calculation without roughness	Calculation with roughness	Experiment
633 nm	4.4 μm	3.6 μm	3 μm
	3.7 μm	2.5 μm	3.4 μm
	2.7 μm	2.3 μm	
805 nm	23 μm	17 μm	17 μm
	14 μm	11 μm	15 μm
	24 μm	18 μm	
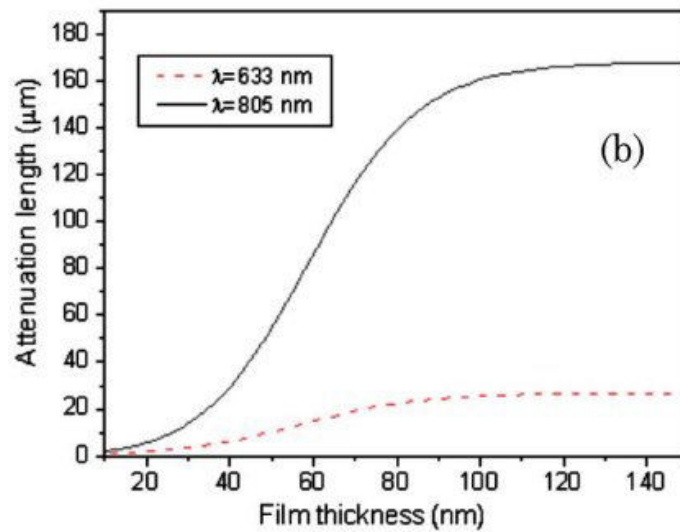
Fig. 2.6 Theoretical values of the thickness dependent L_{SPP} (Attenuation length in the graph) based on different wavelengths; 633 nm and 805 nm, taken from [67].

The same group also investigated the L_{SPP}, depending upon the metal thickness. Their result as shown in Fig. 2.6 represents that as the thickness of the film increases, the L_{SPP} increases (until ≈80 nm for λ=633 nm, and ≈100 nm for λ=805 nm). With the excitation wavelength of 633 nm, the longest L_{SPP} achieved is ≈20 μm. This is achieved around 70 nm film thickness. For 805 nm, the L_{SPP} can go as high as ≈160 μm, which is achieved in 90 nm thickness. Above these thicknesses, the L_{SPP} saturates.

Similarly, the propagation of SPPs was experimentally investigated by [62] on nanoporous gold films. The experiment carried out by leakage radiation microscopy (LRM) demonstrated that plasmonic response of gold can be altered by introducing different levels of porosity, as shown in Fig 2.7. The experiment was done on 50 nm bulk gold, 12 carat gold dealloyed in HNO_3 for 60 min Fig.2.7(a), Hexaporous Au film formed from Au deposition on 30 nm Alumina template 2.7(b) and 55 nm Alumina template etched in 50 wt% KOH Fig.2.7(c). The

exponential decay of each intensity profiles yielded the L_{SPP} to be 9.0 μm, 5.6 μm, 3.7 μm and 4.5 μm for bulk gold, 30 nm, 55 nm hexaporous gold, and dealloyed gold, respectively. This investigation concluded that high porosity of metal film strongly decreases the L_{SPP}.
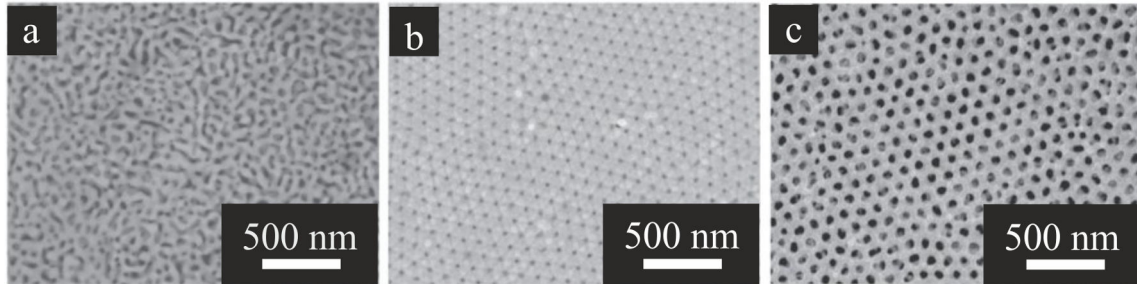
Fig. 2.7 SEM images of porous gold samples under investigation. (a) gold dealloyed in HNO_3 for 60 min. Hexaporous Au film formed from Au deposition on (b) 30 nm Alumina template (c) 55 nm Alumina template etched in 50 wt% KOH[62].

The L_{SPP} comparison on single-crystalline and polycrystalline gold films were studied by [60], using Cathodluminescence imaging spectroscopy. The result is shown in Fig. 2.8. The figure demonstrates that SPPs of the polycrystalline films (red lines) were affected by the roughness and grain boundaries, achieving shorter L_{SPP} for polycrystalline gold film in comparison to single-crystalline gold film (green lines).
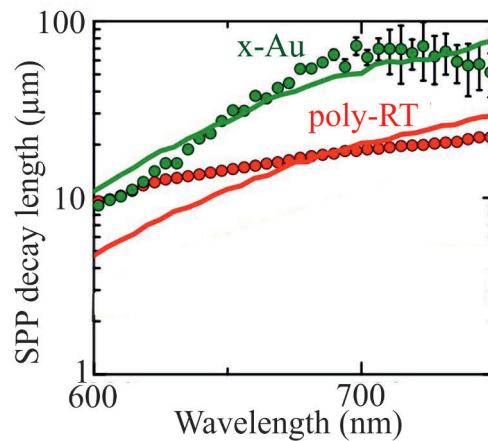
Fig. 2.8 The experimental (dotted lines) and theoretical (solid lines) propagation L_{SPP} of single-crystalline gold and polycrystalline gold as a function of wavelength. The green colour represents the single-crystalline gold x-Au and the red represents polycrystalline gold films deposited at room temperature (Poly-RT) [60].

2.1.5 Application

An ability of SPPs to lead and focus electromagnetic waves using nanostructures [12] opens concepts to many applications in different fields, such as spectroscopy [30], nanophotonics [31, 32], waveguides [38–41], circuits [34, 35], imaging [36] and biosensing [37]. Recent discovery of this technique is to understand the use of this phenomena in interaction of molecules and proteins. Since the excitation properties are strongly dependent on the refractive index of the surrounding medium, therefore, very small details of the variations in the analyte can be observed. To demonstrate the basic mechanism on which SPPs sensors are based on, the adaptation figure from [70] is shown in Fig. 2.9.
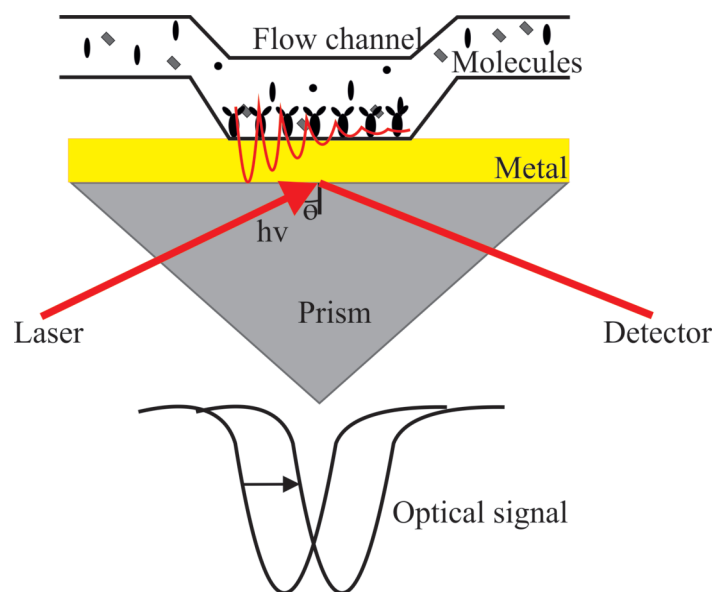
Fig. 2.9 The experimental illustration of application of SPPs as a biosensor adopted from [70] shows propagation of SPPs parallel to the metal surface. The change in optical signal (lower inset) demonstrates that change in the response upon the binding of the specific molecule in flow channel.

In this demonstration, the Kretschmann configuration is adopted, that requires incoming laser beam through the prism. When the momentum matching condition is satisfied, SPPs propagate, while the optical signal is being measured. When the inhibitor binds the molecule to be sensed, the change in the optical signal is demonstrated in lower inset of Fig. 2.9.
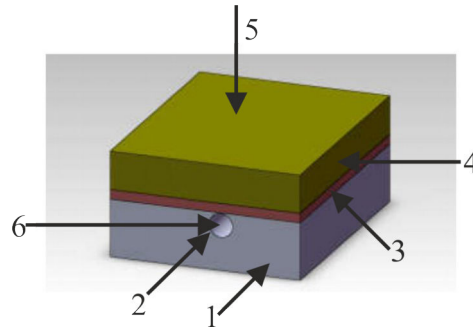
Fig. 2.10 In the figure, 1, 2, 3, 4, 5 and 6 represent silicon, GaN nanowires, magnesium fluoride dielectric layer, gold metal layer, incident beam and the laser, respectively. Incident light from the silicon surface with a vertical angle incident to the magnesium fluoride dielectric layer is concentrated in the electric field between the gold layer and GaN nanowires.

Further research [71] shows that SPPs can improve the characteristics of random laser, such as high threshold and low integration since SPPs can control the diffraction. A random laser structural model based on random particle scattering feedback mechanism was introduced with silicon-based parcel gallium nitride (GaN) nanowires as shown in Fig. 2.10. With the light pumped along the line of angle of incidence, metal is stimulated to produce electronic and photonic resonance. The gain of GaN nanowire and enhancement of SPPs results in formation of a laser on both sides of nanowires due to increase in population inversion. This outcome demonstrates that the SPPs mode and nanowire waveguides coupled into the low refractive index dielectric layer can store light energy like a capacitor. The waveguide mode field area and limiting factors show that the modeled laser can achieve sub-wavelength constraints of the output light field. These performance has a huge contribution into the field of nano-laser, with the huge potential applications, such as in optical, biological detection, medical treatment and data storage [71].

Additionally, the advantage of SPPs into the solar cells was also investigated [72]. The growing demand of photovoltaic devices as an environment-friendly energy has encouraged researchers to investigate possible role of SPPs into this factor. A research was carried out, based on optimised silver gratings to enhance light-trapping in organic solar cells and the comparison of absorption efficiencies was done between with 2D Ag gratings and without as shown in Fig. 2.11. The enhanced light absorption is clearly observed with Ag gratings (solid blue line) in comparison to without gratings (dotted line). The enhancement occurs due to the excitation of localised surface plasmon resonance (LSPRs) [73] near the grating and SPPs at the active layer/Ag back-contact interface. The investigation of the field distribution was also carried out, as shown in the insets of same figure. The enhancement in the range wavelength 340-490 nm is due to strong confinement of incoming light into SPP modes

at the active layer/Ag back-contact interface. The enhancement in the wavelength range 500-640 nm observes the domination of the excitation of LSPRs around the grating inside the active layer. The multiple resonance were achieved at wavelengths 650-800 nm due to strong coupling between LSPRs and SPPs. The 2D gratings contributed the broadband absorption enhancement of up to 18.5%, compared to 15.4% with 1D Ag gratings, researched by the same group [74].
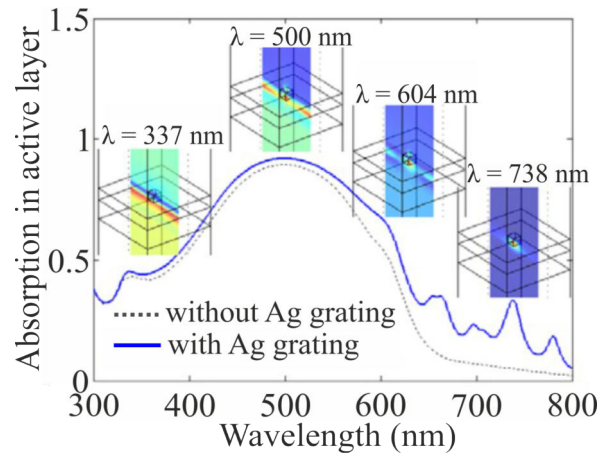
Fig. 2.11 Absorption in the active layer of organic solar cells with and without 2D Ag gratings integrated inside the active layer. The insets show the calculated Hy field amplitude distribution at different relevant wavelengths.

The advantage of SPPs are not limited to above chosen examples. Depending upon different applications, different working condition and design parameters of chosen material system and different laser systems are required. This emphasises the necessity of more research into the perspective of SPPs or to evaluate the alternative methods. In this context, the next section discusses semiconductor nanoparticles as an alternative sensor materials.

2.2   Properties of semiconductor nanoparticles

Besides many positive features of nanometer sized semiconductor materials, the confined NPs become susceptible to a strong size- and temperature-dependent Auger recombination (AR) [75–77]. This process interrupts the normal exciton mobility by extra losses. During this process the Coulomb interaction between the electron-hole pairs (excitons) is interrupted by the AR, resulting in increased heating of the material [78, 79, 19]. A previous research done on cadmium selenide/zinc sulphide (CdSe/ZnS) QRs and QDs showed the AR in QDs occurring on the picosecond timescale, which is faster than the exciton radiative lifetime in the nanosecond regime [80]. This results in fast reduction of the optical gain, detecting only fluorescence from the materials after optical pumping with long pulse durations in the order of nanoseconds. Nevertheless, amplified spontaneous emission (ASE) can still be achieved when the pumping process is faster than the AR at room temperature or when the material is cryogenically cooled. One of the common ways ASE is achieved is by using high power excitation pulse in the femtosecond regime [81]. However, recently low-threshold lasing in CdSe/ZnS QDs embedded into a thin layer of poly(methyl methacrylate) (PMMA) has also been demonstrated under nanosecond pumping at 355 nm using a distributed feedback structure in order to benefit from low gain [82].

Semiconductor NPs are classified according to their dimension, such as quantum confinement, morphology, homogeneity, distribution and ability to aggregate [3]. Their properties, that are mainly focused and are more susceptible to the objective of this thesis will be further discussed below.

2.2.1 Quantum confinement

The QDs (0-D) are the most commonly investigated NPs. These particles are spherical, and therefore, have zero degrees of freedom for its motion as the exciton is confined in all three dimensions. Hence, they propose no space for the exciton to take place. The particles confinement and degree of freedom of different NPs are shown in Table 2.3.

Table 2.3 Quantum NPs with their confinement and degree of freedom.

Nanoparticles	Quantum confinement	Degree of freedom
QDs	3-D	0-D
QRs	2-D	1-D
QWs	1-D	2-D

Another consequence of the confinement effect is an increase in energy levels. The relationship between the band gap energy with respect to the size of spherical NPs is shown in Fig. 2.12. As mentioned in *Chapter 1*, the energy band gap of confined QDs is inversely proportional to the radius of particle [16], given by the Brus equations, explained by equation 2.9 [83].

$$E_{QDs} = E_{bulk} + \frac{h^2}{8R^2}\left(\frac{1}{m*_e} + \frac{1}{m*_h}\right) \tag{2.9}$$

where, E_{QDs} is the energy bandgap at the specific size, E_{bulk} is the bandgap of the bulk material, h= 6.63 x 10^{-34} m^2kgs^{-1} is a Planck's constant, $m*_e$= 1.18×10^{-31} kg is the effective mass of electron and $m*_h$= 4.09×10^{-31} kg is the effective mass of hole. For the semiconductor NPs opted in this thesis; CdSe and Cadmium Sulphide (CdS), the E_{bulk} are 1.74 ev [84] and 2.42 ev [85] respectively. As the size of this NPs decreases as demonstrated in Fig. 2.12(b), increase in bandgap is observed. This requires high excitation energy for emission to take place, contributing to different emission properties as the size is changed.

(a)

(b)
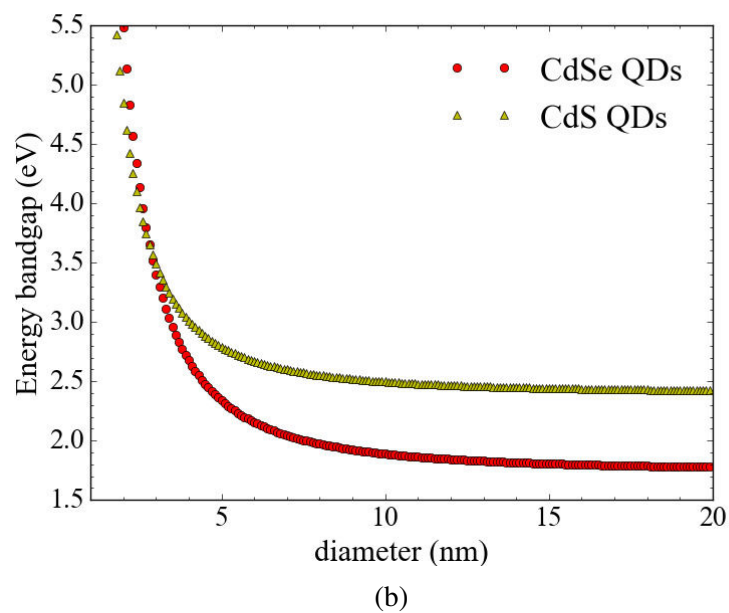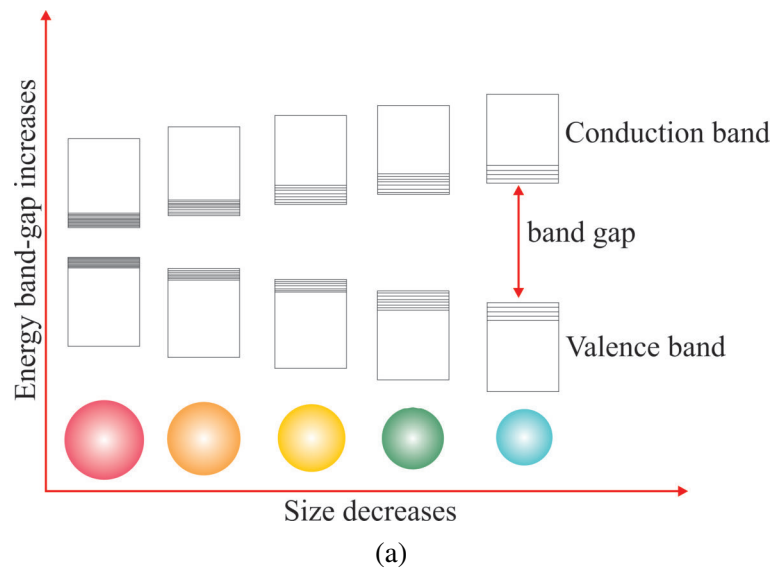
Fig. 2.12 (a) Schematic diagram of dependence of energy band gap with respect to the size of the NPs [86]. As the size of the NPs decreases, the bandgap increases. This results in requiring high excitation energy for emission. The requirement of higher excitation energy observes different emission properties that is applicable for different functions. (b) Size dependent energy bandgap of spherical CdSe and CdS QDs.

2.2.2 Morphological effects
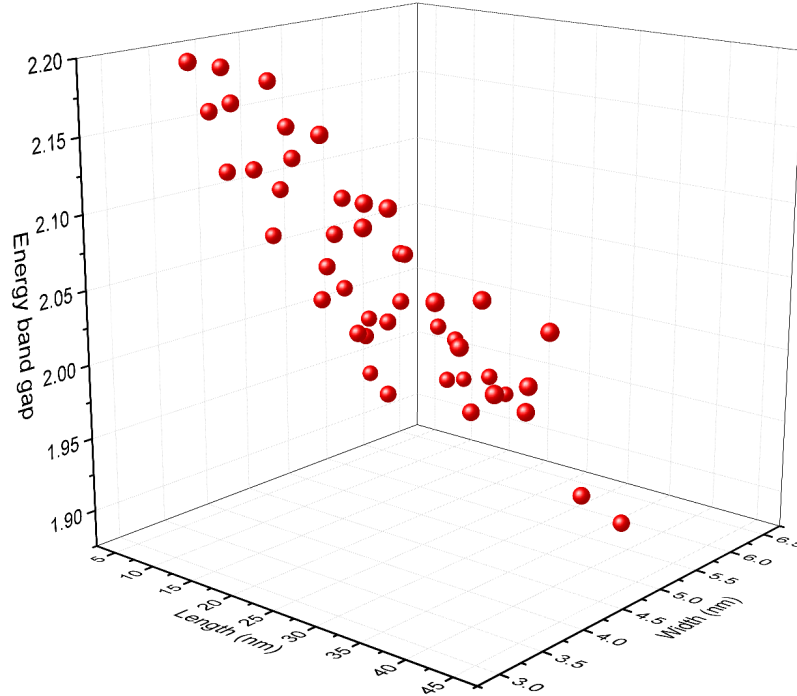
Fig. 2.13 Size dependent energy bandgap of CdSe QRs.

In addition to the size, shape of the NPs also gives an opportunity to manipulate their properties with respect to the required functions. In morphological characteristics, generally high and low aspect ratio of the particles are considered. High aspect ratio NPs include QRs and QWs with various shapes and the width that varies with the length. Fig. 2.13 represents the bandgap energy of CdSe based on different width and length, with the experimental values taken from [84].

The spherical QDs are an example of small aspect ratio. The electronic states of NPs strongly depends on their confinement. Increasing the aspect ratio reduces the confinement along the direction where the particle has degree of freedom. As shown in Table 2.3, QRs and QWs have 1-D and 2-D degree of freedom with respect to the traditional QDs. During the transition process from 0-D to 1-D and 2-D, the energy levels are extended into several levels towards the extended axis.

In QRs, the particle is elongated along the z-axis, which means the exciton can be mobile in z-axis although confined in the x and y directions. On the other hand, different system called QWs have confinement only along z axis and the particle is extended equally in x

and y for the exciton [3]. Previously, it is also investigated [87, 77, 88] that an increase in aspect ratio of the particles also provokes the confinement energy in the direction of long cross-section, such as in 1D QWs or 2D QRs, with a smaller electron-hole interaction energy.

The bandgap of the rods depends mainly on its width and only slightly on its length [84, 89]. According to [90], the bandgap of 5-monolayer CdSe/CdS core/crown QWs has a bandgap of 1.950 eV.

2.2.3   Stimulated emission

One of the many appealing properties of the semiconductor NPs is an ability to demonstrate amplified spontaneous emission (ASE); a topic which is thoroughly researched by many scientists [19, 91, 80, 92–95]. They demonstrate basic features of radiative and non-radiative recombination, which will be discussed below.
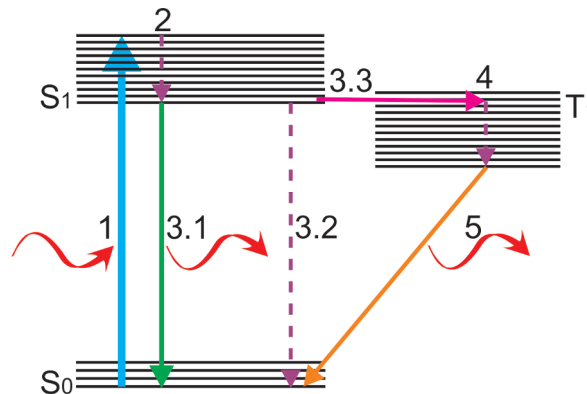
Fig. 2.14 The Jabłoński diagram describing the process of the radiative and non-radiative process. The incoming photon is described by process number 1, followed by the vibrational relaxation (number 2) within the excited state. The next stage has three possibilities: (3.1) Fluorescence, (3.2) Non-radiative recombination and (3.3) Intersystem crossing. Process 4 describes the vibrational relaxation within triplet state. Finally, number 5, called phosphorescence, which describes the relaxation of the electron from triplet state to ground state.

The NPs have strong absorption in the UV electromagnetic spectrum region. As represented by Jabłoński diagram in Fig. 2.14, when photons with the wavelength that matches the absorption spectrum of the materials is coupled in, the electron is excited from valence (S_0) to the conduction band (S_1), process number 1. During this process, the temperature of the carrier rises due to which molecules start to vibrate and give away some of its energy to its surrounding. This stage is followed by the vibrational relaxation (process number 2). This takes the electron from higher state of S_1 to the lower state of S_1. Once the electrons are relaxed in S_1, there are three possibilities that can occur, represented by 3.1, 3.2 and 3.3. The

process number 3.1 represents that the electron can relax back to the valence band by giving out photon. This is called fluorescence. The process number 3.2 represents that the electron can take similar path as 3.1 but this time they lose their energy as heat, not photon. This is the non-radiative recombination. The final possible process, represented by number 3.3 is the intersystem crossing. In this process, the electron change their electronic state and proceed to triplet state (T_1). The electron go through additional vibrational stage in T_1 and finally, relax back to S_1, represented by process number 5. This process is called phosphorescence. The vibrational relaxation stage loses some of the energy, resulting in lower energy of emitted light in comparison to absorbed light. Similarly, the phosphorescence has a lower energy and is slower than the fluorescence.

During the initial stage of the process when the energy is pumped into the system, the energy losses will be higher than the gain. Until the gain is equal to energy lost, this process of the exciton results in spontaneous emission, giving just radiative and non-radiative recombination as described above. However, the continuous pumping will lead to the threshold point when gain energy becomes equal to the loss. After this phase, upon continuous energy supply, the gain energy overrules and the stimulated emission takes place. During this process, the incoming photon of a specific frequency interacts with electron in S_1, dropping it to S_0, releasing energy as photons.

In QWs, due to their 2-D size [86], they have much higher absorption cross-section as compared with QRs and QDs, and this enables gain in lower threshold pump power. Furthermore, their strong 1-D confinement restricts carrier direction towards remaining two dimensions, enabling higher concentration of carriers to contribute to the excitons. This reduces an ASE threshold power [19]. The QDs on the other hand do not have this privilege due to their 3-D confinement effect. The QRs with their 2-D confinement however are more favourable than QDs but less than QWs.

In order to understand the properties of laser, it is crucial to comprehend how the light is generated [96]. The typical laser consists of a resonator and a gain medium. The resonator sends light backwards and forwards through the gain medium, the process by which it is amplified by stimulated emission. The condition for generating laser is when the amplification exceeds the losses of the resonator. The generated light through stimulated emission is the coherent light as the incident and emitted waves have same phase, direction and polarisation. Physically, a narrow output spectrum is observed in this case. Normally, at lower excitation power, there is no coherent output from the laser. The power is needed to increase to observe this property. The power at which change in this behaviour occurs is called threshold.

The ASE can be confirmed quantitatively although there is a debate on the criteria for lasing and its thresholds [97–99, 96, 100, 101]. Researchers are considering change in the

emission spectrum as the first hint of ASE. It normally appears as a sharp peak on top of the broad fluorescence spectrum, decreasing the full width half drastically [102, 82]. Previously, it has been observed a reduction in linewidth from 1.2 nm below the threshold to 0.02 nm above the threshold [103]. In another microcavity study, the spectrum narrowed from 20 nm below the threshold to less than 2 nm above the threshold [104].

A group [82] investigated the gain of colloidal QDs, using distributed-feedback lasers operating in the nanosecond regime. The lasers were designed based on second order grating structure covered by a thin-film QDs/PMMA. The threshold fluence of the laser was calculated to be 0.5 mJcm^{-2} for a 610 nm emission. More recently, an investigation [105] on the ASE on different monolayers (ML) of QWs, emitting at different wavelength reported blue-emitting 3ML CdSe to have a lowest ASE threshold to date of their publication. The results are shown in Fig. 2.15. The threshold values and the emission peaks are listed in Table 2.4.
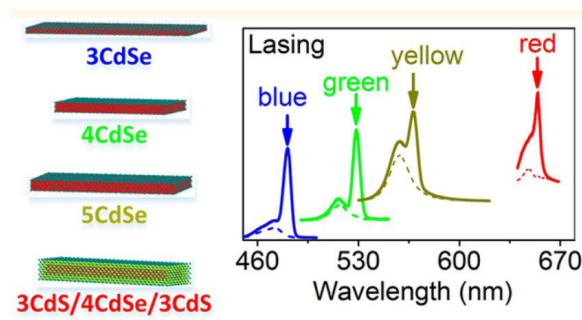
Fig. 2.15 ASE threshold of QWs that consist of different monolayers; 3CdSe, 4CdSe, 5CdSe and 3CdSe/4CdSe/3CdS, each emitting blue, green, yellow and red, respectively.

Table 2.4 QWs threshold values dependent on monolayers

Quantum wells		
Materials	Emission peak	Threshold
3ML CdSe	462 nm	50 μJcm^{-2}
4ML CdSe	512 nm	17 μJcm^{-2}
5ML CdSe	550 nm	28 μJcm^{-2}
3ML CdS/4CdSe/3CdS	630 nm	6 μJcm^{-2}

2.2.4   Auger recombination
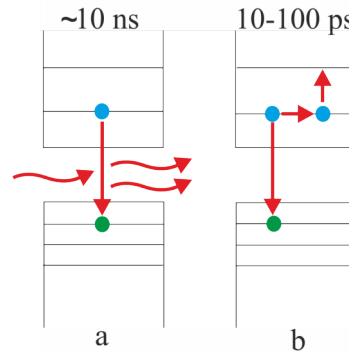
Fig. 2.16 The normal stimulated emission process (a) and the auger recombination (b) [106]. In stimulated emission process, when the photon comes in, the electron from the excited state is combined with the hole, releasing photon as an energy. In AR, when the photon comes in, energy from the electron is transfered to another electron in the form of kinetic energy. This results in exciting that electron to the higher state, interrupting the normal relaxation process.

One of the drawbacks of using semiconductor NPs is, they are susceptible to AR. In normal radiative recombination process as shown in Fig. 2.16(a) the electron is combined with the hole and the photon is released. However, in AR, as shown in Fig. 2.16(b), the normal exciton process is interrupted by extra losses. Once the electron reaches to the excited state, its energy is transfered to another electron in the form of kinetic energy, which results in exciting that electron to the higher state, preventing the normal relaxation process.

As previously stated (*Chapter 1, Section 1.3*), due to the inverse relationship between the size of the NPs and the bandgap, the use of semiconductor NPs for optical amplification can have a drawback of needing high excitation power [81]. However, the requirement of high excitation power results in higher rate of vibrational relaxation process, which results in higher heat losses than in bulk semiconductor. Hence, decrease in size of the particles make them more susceptible to a strong size-dependent AR. Previously, it has been shown that the rate of AR in QDs occurs in the picosecond timescale, faster than the exciton vibration timescale [80]. Therefore, to achieve optical gain, the relaxation time has to be faster than the AR.

Theoretically, the Coulomb interaction between the electron and hole causes the energy relaxation process after a population inversion. Upon the condition when the AR is faster than the relaxation process, the AR process dominates the Coulomb interactions and limits the ASE [78, 79, 19]. One of the ways this effect can be compensated is by using shorter excitation pulse, such as femtosecond. Again, the rate of AR depends on the confinement

dimensionality of the quantized NPs [75–77] and is expected to be significantly lower in 1-D QRs and 2-D QWs compared to 0-D QDs [80].

The effect of the carrier confinement dimensionality on AR by tuning the confinement regime has been demonstrated in the CdSe material system considering 0-D QDs and 1-D QRs [77]. It has been found that QRs show lowest AR and thus higher amplification at the same emission wavelengths, which can be explained by a significant shortening of the exciton radiative lifetime [87] and a reduced Auger heating rate [88]. In addition to the reduced AR influence, the 1-D QRs and 2-D QWs show an enhanced absorption cross section compared to 0-D QDs, where the rod and shell structures are acting as broadband optical antenna [80] along with a higher carrier concentration which can contribute to the excitons and thus enable higher optical gain [19]. Small quantum wells (QWs), due to their 2-D spatial extension, have been demonstrated to exhibit an even larger absorption cross-section as compared to QRs and QDs [86]. This enables achieving higher gain and ASE without any resonator structure using lower pump power laser sources.

2.2.5   Temperature influence

When the electrons are excited by an optical emission that has an energy higher than the bandgap, the electrons leave their initial state and reach an excited state within a pulse duration of the pumping source [107]. During this process, the temperature of the electrons and holes rises up to thousands of Kelvin higher in comparison to that of the lattice [107]. In addition to this, when the sample is heated, the additional temperature results in lattice expansion. As a consequence, the amplitude of the atomic vibrations accelerates, increasing an interatomic spacing. The research done by [108] shows that at high temperatures, the thermal expansion coefficient shows linear behaviour but at low temperature, nonlinear effect is observed. The expansion causes electron lattice interaction, which also results in the shift in the relative position of the conduction and valence bands [108, 109]. The temperature dependent energy bandgap can been explained by the following expression [108]:

$$E_g(\mathrm{T}) = E_g(0) - \alpha \frac{T^2}{T+\beta}$$

where, $E_g(\mathrm{T})$ is the energy bandgap of the compound at certain temperature, $E_g(0)$ is the bandgap at ambient temperature, α and β are the material's constants. The equation suggests that the rise in temperature encourages shrinkage of the bandgap. Taking the bulk bandgap values of CdSe and CdS as 1.74 eV and 2.42 eV, respectively at ambient temperature, the equation can be plotted to get the graph as shown in Fig. 2.17. For this calculation, α and β values of 0.65 meVK^{-1} and 400 K, respectively for CdSe are considered [110]. For CdS, the

values of 0.33 meVK^{-1} and 420 K are considered, after multiple iteration based on the band gap value of 2.42 eV.
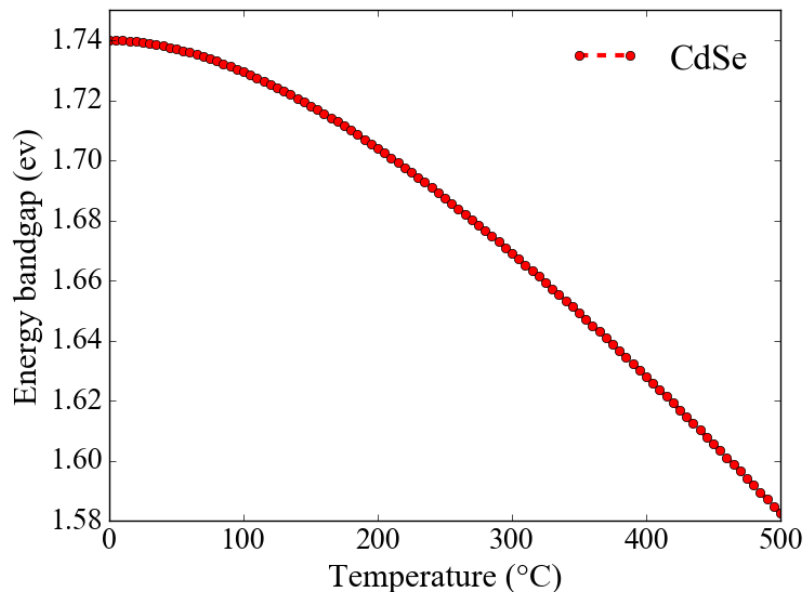
(a) CdSe
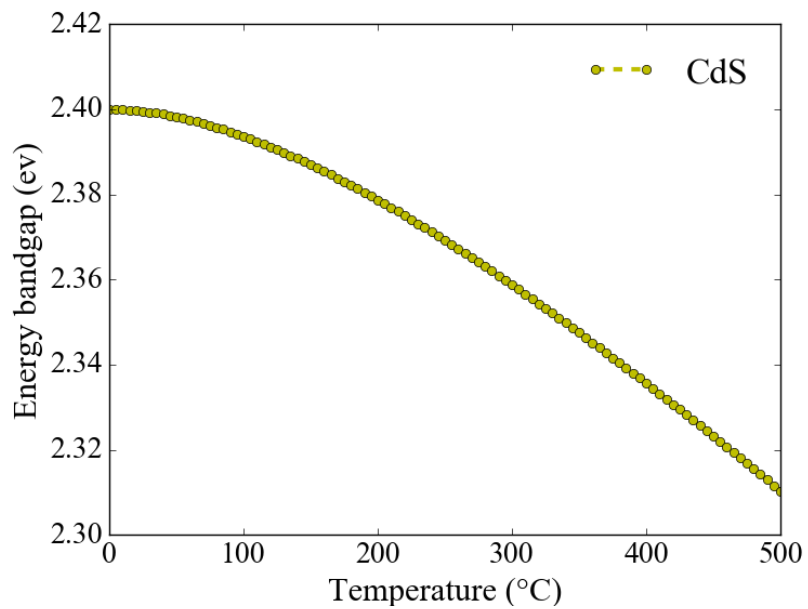
(b) CdS

Fig. 2.17 Theoretical bandgap of bulk CdSe and CdS, dependent on temperature (°C). The calculation suggests that as the temperature increases, the energy bandgap decreases.
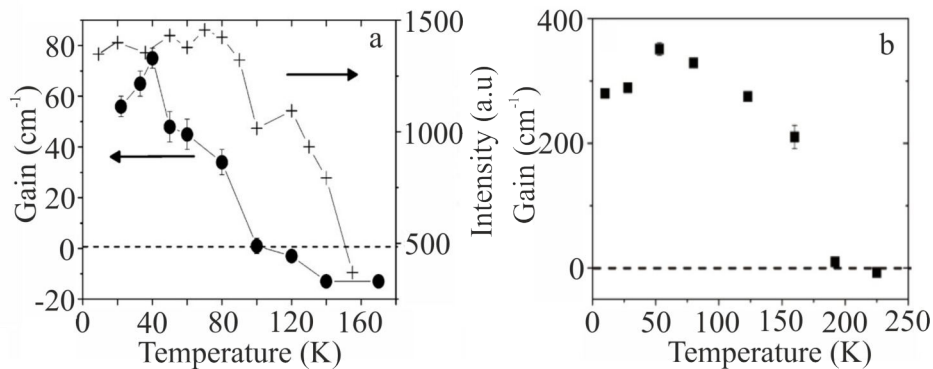
Fig. 2.18 The experimental investigation on the optical gain of CdSe/ZnS QDs (a) and QRs(b) dependence on temperature by [80].

The experiment, carried out by [80] on investigating optical gain of CdSe/ZnS QDs and QRs with respect to the temperature is shown in Fig. 2.18(a-b). The QDs and QRs consisted of volume ratio of ≈6% and 3%, respectively. The study was carried out by focusing nanosecond optical pumping (532 nm, 5 ns) into a stripe of 100 μm width by a cylindrical lens into a close-packed films of QDs and QRs. The gain measurement was accomplished using the variable stripe length method.

The QDs produced relatively small gain factor of ≈80 cm^{-1}. The strong decrease on the gain after 40 K shows that its dependence on the temperature is higher in comparison to QRs in Fig. 2.18(b). A gain factor of ≈350 cm^{-1} for QRs was achieved up to 120 K. After that, there was a drastic decrease in the gain. Another noticeable factor is that the QRs can endured up to higher temperature in comparison to QDs.

2.2.6 Multi-photon excitation
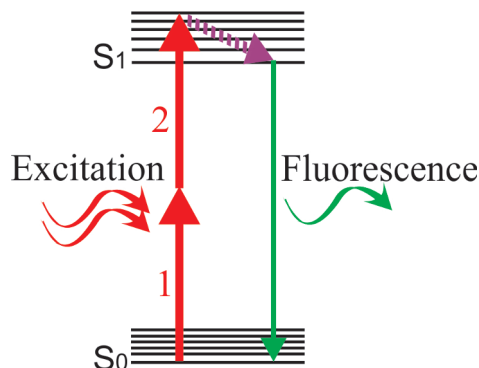
Fig. 2.19 The two photon absorption process requires excitation of two photons (1 and 2 in the figure) of equal energies. The emitted photons provide fluorescence while relaxing back to the valence band.

The discrete band structures of the NPs depend on their size. The increase in the bandgap due to decrease in size results in more discrete levels energy bands. This decreases the chances of the excited electrons reaching the energy levels in the conduction band as the energy of the incoming photon has to match with the bandgap of the energy levels for the emission to take place. Typically, once the NPs are prepared, their absorption spectra is measured to understand their absorption properties. Additionally, PL spectra can be measured to analyse which wavelength gives the maximum emission intensity. This measurement can be carried out with one-photon (standard procedure) or two-photon absorption.

Due to the fact that two-photon microscopy offers the advantages of less phototoxicity, deeper penetration depth and lower self-absorption, it is normally very beneficial in biological applications. The recent research demonstrated its use in detecting lysosomal thiols in live cells and tissues [111].

The phenomena of two-photon absorption was theoretically first introduced by Maria Goeppert-Mayer [112]. Later on in 1961, this effect was experimentally confirmed by Kaiser and Garret [113]. As shown in Fig. 2.19, in this process, two photons (1 and 2) are simultaneously absorbed to excite the electron from valence to conduction band. The difference in an energy of valence and conduction band is the sum of energies of two photon involved.

Normally, the photons in the ultraviolet spectra range are required to initiate this mechanism [114, 115]. However, in alternative case, similar process can be achieved by the absorption of two less energetic photons simultaneously under high intensity laser illumination.

The clear observation of the two-photon absorption can be achieved by the non-linear process, which normally occurs when the sum of energies of the two photons are equal or greater than the energy bandgap of the molecule. Due to the fact that this process requires two photons for the excitation to occur, the absorption molecule has a quadratic function of the excitation radiance, whereas one-photon process has a linear process.

According to [114], in comparison to one-photon absorption at UV, two-photon process reduces the photobleaching and photodamange process. This is crucial when examining biological specimens as it helps increasing the viability, making this process very advantageous in imaging highly dispersed tissues.

The two-photon absorption coefficients of CdSe/CdS core/shell QDs were calculated using a Z-scan technique, using a femtosecond Titanium:Sapphire (Ti:Sa) laser system [116]. The mean diameter of CdSe core was 3.6 nm whereas for CdS shell, it ranged from 4.2 nm to 7.2 nm. The NPs samples with different ML with a density of $1.8x10^{-4}$ moll^{-1}, were dispersed in toluene in a 1mm quartz cuvette. To compare the values, the same literature considered the nonlinear transmission measurement of the QDs, with density of $2.2x10^{-3}$ moll^{-1} in 1 cm path length quartz cuvette. The values from the two methods are listed in Table 2.5.

Table 2.5 Multiphoton absorption cross-section of CdSe/CdS.

monolayer	GM values using z-scan	GM values by nonlinear transmission
1	79500	72000
2	81000	74000
3	98000	89000
4	84800	79000
5	80500	73000

2.2.7 NPs-polymer waveguide

Besides the emission ability of semiconductor NPs, this thesis concerns their competence once they are embedded into the polymers. Since the introduction of first dye laser in 1966 [117, 118], many different possible dyes and fluorescent materials have been investigated with respect to their tendency to fluoresce and stability. An experimental comparison of the emission spectra between organic dye rhodamine 6G and semiconductor QDs [15] suggested better stability of the QDs whereas clear photobleaching was observed in Rhodamine 6G. This presents QDs as an attractive alternative to dyes and organic semiconductors as a gain medium. With their better photostability, these NPs can be utilised to develop more reliable

high power lasers, the great advantage over organic lasers. The improvement of performance of these QDs-based devices depends not only on quantum yields of the particles but also on the better structures of NPs [119]. Therefore, using suitable photosensitive polymer is very significant. The stability can be further increased by capping of the NPs. The particles, such as CdSe are commonly capped by the crown/shell that have higher bandgap. Although growing shell/crown enhances the photostability, it is possible to form defects at the interface between core and shell/crown due to large lattice mismatch and interfacial strain [119].

The previous researchers have demonstrated colloidal CdSe/Zns QDs [82], CdS/SiO_2 cores [120] and CDSe and CdTe QDs [121] into PMMA powder. However, producing hybrid polymer-NPs materials that is photocurable, without losing their distinctive properties is a challenge. The process of embedding NPs into the polymer can alter the chemical environment of the NPs, hence affecting their properties. To use the adopted materials as a waveguide, their refractive index has to be higher than the substrate and surrounding. Once the NPs are embedded into the polymer, the change in the refractive index of the solution occurs, which is one of the challenges for NPs/polymer nanocomposites. The change in refractive index can be evaluated with respect to the following equation [6];

$$n_{composite} = n_{NPs} * C_{NPs} + n_{polymer} * C_{polymer}$$

where, n_{NPs} is the refractive index of NPs, $n_{polymer}$ is the refractive index of polymer. C_{NPs} and $C_{polymer}$ are the concentration of NPs and polymer in wt% respectively. The change in the refractive index will also adjust the absorption and emission peak. It is expected the NPs will tend to aggregate once they are embedded into the polymer. In this case, the emission wavelength is expected to increase, presenting the property of red-shifting, as achieved with ZnO/polybutanediolmonoacrylate [122] and ZnO/PMMA [123] respectively.

2.2.8   Application

Semiconductor NPs have become a topic of huge interest in recent years due to their quantum confinement properties [15, 6]. As the size of the NPs decreases, discrete energy levels in the electronic system appear, which provide possibilities for fluorescent emission and light amplification in the visible spectral regime [19, 91, 80, 92–95]. The influence of emission wavelength by the degree of confinement, makes them promising for the development of novel light sources. This property endorses huge advantage in photonics, telecommunication and medical applications [19].
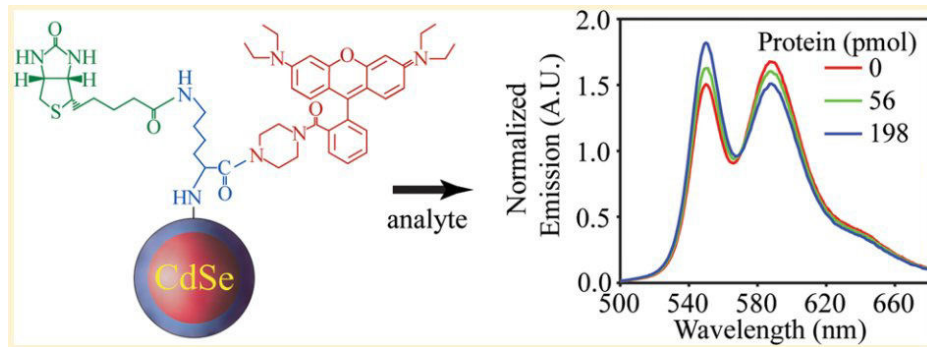
Fig. 2.20 The change in the emission spectra with respect to concentration of protein when it comes in contact with QDs-bound Rhodamine B Piperazine-Biotin dyes.

Recently, a biological sensor consisting of CdSe/ZnS QDs that can sense protein has been addressed [124]. The emission from the NPs is confined in a way that the fluorescence resonance energy transfer (FRET) occurs from donor to the dye acceptor. When these NPs are exposed to the target proteins, the analytes bind to the surfaces of the QDs, altering the microenvironments of the QDs-bound Rhodamine B Piperazine-Biotin dyes, which results in changing in emission properties as shown in Fig. 2.20.

Alternatively, these NPs can also be advantageous in the form of temperature sensor. Recently, CdSe/ZnS has also been investigated for this purpose [125]. A CdSe/ZnS NPs was embedded into Silicon dioxide (SiO_2) dielectric matrix and the temperature-dependent spectral and intensity modes were investigated from 295–525 K. The result demonstrated variation in peak wavelength of $\approx$0.11 nm per Degree Kelvin.
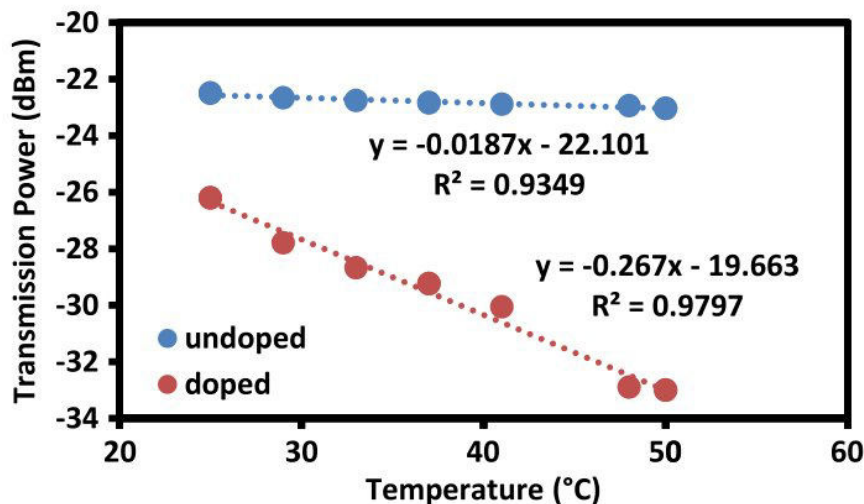
Fig. 2.21 The temperature dependence on output power observation from the CdSe QDs doped PMMA (red line) and undoped PMMA (blue).

Another group has investigated [126] a behaviour of transmitted power from the sample as a hint of possible temperature sensor by embedding CdSe QDs into PMMA. The comparison was done on the output signal from the QDs doped and undoped PMMA over the temperature range of 25°C-48°C. The result is shown in Fig. 2.21. It can be observed that an output signal of the doped material is influenced greatly as the temperature is changed. However, the increase in temperature for undoped material did not have significant differences.

Furthermore, the biological aspects of the quantum NPs have been enhanced with the study of natural biomaterials membranes as resonance cavities [127]. This was demonstrated by embedding ZnO NPs into the Pieris canidia butterfly wing at room temperature. The morphologies of sample was characterised by SEM as shown in Fig. 2.22 (b) at low magnification and (c) at high magnification. The reflectance spectrum was detected by a spectrophotometer and shown in Fig. 2.22 (d). The figure shows that after 350 nm, the reflectance is quite high, in between 40-50 %. This proves that the excitation laser wavelength needs to be lower than that. The lasing spectra, shown in Fig 2.22 (e) were achieved by exciting the sample optically with a Q-switched 4ω Nd: YAG laser (266 nm, 3–5 ns pulse,10 Hz), and focusing to a diameter of about 500 mm. As observed in the figure, the lasing property is visualised already at the excitation energy of 70 μJ at the peak wavelength of 386 nm. This approach proves that biological materials and structures can be good candidate for low cost ecological friendly optoelectronic devices.
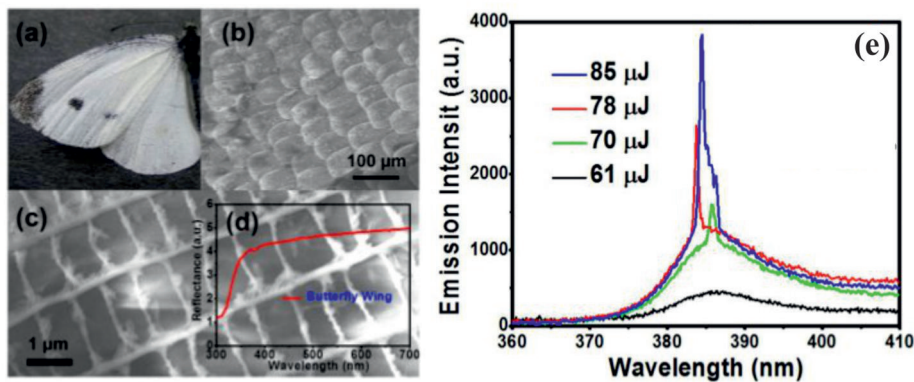
Fig. 2.22 (a) Pieris canidia butterfly, (b) SEM picture of wing scale at low magnification, (c) high magnification SEM image of the wing scale, (d) reflectance spectrum of butterfly wing, (e) lasing spectra of ZnO/butterfly wing composite with increasing excitation energy.

Chapter 3

Objectives

The preceding chapters focused on the importance of miniaturisation of electric circuits and role of nanotechnology in this forming. Yet, the choice of surface plasmon polaritons (SPPs) and semiconductor nanoparticles (NPs) as the investigation topics as the possibility of large and small scale sensor as the applications were also asserted.

The **first key goal** of this thesis is to determine the propagation length (L_{SPP}) based on different metals (gold and silver), fabricated by different methods. Since L_{SPP} depend on the quality of metal surface and morphology [128, 67], the proper control of these losses is a huge challenge in plasmonic field. Once losses are controlled, the application of SPPs can extend their applications to the miniaturised high efficient photonic circuits. The effects of film qualities on SPPs L_{SPP} is analysed by changing the deposition methods, hence tuning dielectric constants. Additionally, the influence of the metal thicknesses on the L_{SPP} of SPPs is also investigated.

To address the above concerns, after demonstrating experimental methods and materials in *Chapter 4*, *Chapter 5* mainly concerns on SPPs investigation on gold and silver based on following points:

- Fabrication methods

- Measurement methods

- Thickness

- Crystallinity

For SPPs investigation, gold, silver, copper and aluminum are considered to be the suitable metals. However, gold is considered to be most stable element, making it noble for

applications where as silver, copper and aluminum suffer losses due to oxidation properties. In comparison to latter elements, silver exhibits lowest ohmic losses in both visible and near-infrared. Additionally, silver also has an advantage of being more affordable than gold. Considering these orientations, gold and silver are chosen for this investigation.

The **second key goal** of this thesis concerns the feasibility of semiconductor NPs on their ability to emit coherent light. Since semiconductor NPs are of great interest due to their quantum confinement properties, NPs of different confinement dimensionality are considered. This prioritises the intended comparison to the utmost as the overall ASE performance of a given nanoparticle film strongly depends on various often only poorly known parameters such as packing density, optical homogeneity and many more. This makes a comparison of a given particle geometry with data for a different particle geometry always misleading and incomparable. Therefore, an effort has been taken to compare all NPs, produced by identical procedures and measured under identical conditions, giving rise to a robust analysis of the influence of the particle geometry on the ASE performance.

To address the above concerns, semiconductor NPs in *Chapter 6* are divided into different chapters, focusing on their sub-goals:

- An optical amplification properties of the home-made quantum NPs of cadmium selenide/cadmium sulfide (CdSe/CdS) material system with different dimensionality of spatial confinement is addressed. CdSe/CdS core/shell QDs, QRs and 5 monolayer thick core/crown QWs at ambient temperature are considered, exhibiting 0D, 1D and 2D spatial confinement dimensionality of the electronic system, respectively. The comparison is done based on ASE threshold values achieved by different NPs, while excited by different laser system under same condition. The outcome features a scope of developing novel types of tunable lasers that are functional at room temperature.

- In addition to the size and morphology of NPs, an impact of surrounding environment on ASE is also regarded as a fascinating investigative specification. The perception on how the ASE on NPs is influenced with regards to change in temperature is the focus of next section in *Chapter 6*. The influence of temperature on ASE of NPs have been investigated by many scientists [80, 119, 129] but this section focuses on investigating the temperature influence on self-made NPs that outwits other NPs in preceding investigation. Emphasis is placed on understanding the emission peak of the NPs as the temperature is changed. Upon the observation of significant temperature influence on these NPs, an approach can be adopted in real-life application as a temperature sensor.

- The NPs adopted in this thesis are specifically prepared for the observation of amplified spontaneous emission (ASE). This creates the importance of investigating optical

properties of these NPs more in detail. The exciton emission of NPs is observed with respect to one-photon and two-photon absorption to obtain better understanding of size dependent energy levels of the NPs. Next, in this chapter, a procedure to embed inorganic NPs into a photocurable polymer is accomplished. An adaptable polymer is investigated based on their foreseen applications.

Chapter 4

Experimental methods and materials

4.1 Methods

4.1.1 Photolithography

The subwavelength lines, required for the excitation of the SPPs can be synthesised by different lithography process. It is a sophisticated method to transfer a desired pattern from a donor into the substrate, creating a huge advantage in manufacturing complex circuits. Many techniques of lithography, such as photolithography [130], e-beam lithography [131], x-ray lithography [132], scanning probe lithography [133], magnetolithography [134], extreme ultraviolet lithography [135], nanoimprint lithography [136] and interference lithography [137] are already available, each possessing benefits according to the desired applications. Assessing the photonic structures, required to synthesis in this thesis, photolithography and e-beam lithography seem to be applicable. However, although the resolution limit of e-beam lithography goes down to up to 2 nm [138], its high cost factor and lengthy process [139] makes this method less preferable. The photolithography technique, developed at Laser Zentrum Hannover e.V., based on existing projection photolithography, gives benefit of low-cost and high enough resolution ($\approx$150 nm) needed for this thesis. Previously, the resolution limit of this techniques has been reported up to 200 nm [140, 141].

In the case of photolithography, a light sensitive polymer, called a photoresist is exposed and developed to form two-or-three-dimensional patterns on the substrate. The schematic diagram of this technique is shown in Fig. 4.1. The general process consists of two-step process that requires creating desired structures on a computer. The technique was developed by giving full attention to the cost, making the microscope objectives only the expensive part throughout the process. The procedure is illustrated further below.
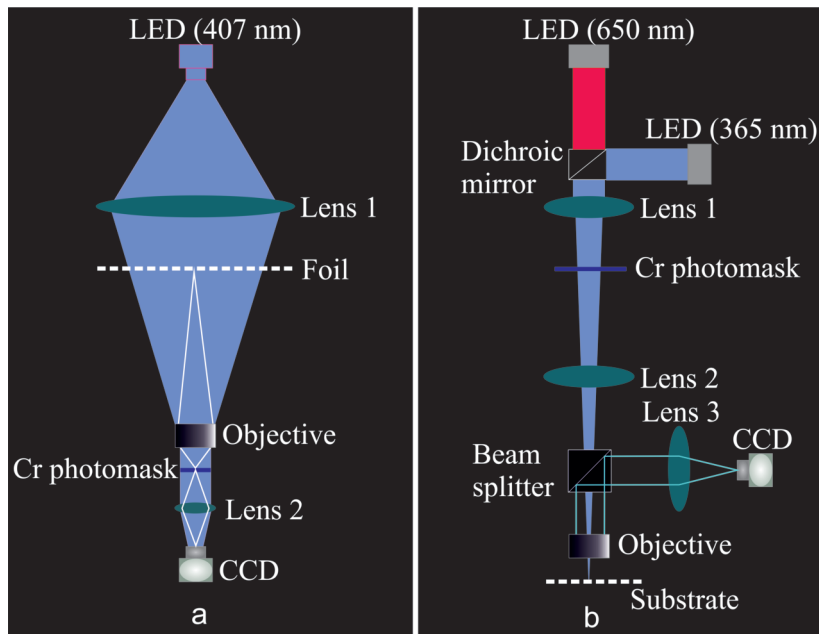
Fig. 4.1 The photolithography consists of two-step process; (a) demagnification procedure; a high power LED (407 nm) is used for demagnifying printed mask by 10x onto Cr photomask (25 mm diameter and 1 mm thick), coated with positive photoresist (see materials section for details). After development, the Cr photomask is taken to the next demagnification step. (b) Microscope Projection Photolithography; the demagnified image on Cr mask is projected with a 365 nm high-power UV LED onto a substrate that consists of photosensitive resist layer. Both setups consist of sophisticated CCD-cameras to maneuver focusing.

Demagnification Procedure

Initially, the desired structures of required sizes were designed in CorelDraw and printed onto an A4 size transparent foil with a laser plotter (Bungard FilmstarPLUS with B&W printing resolution of 16,256 dpi = 1.56 μm). Once the foil was ready, first demagnification process (10 times demagnification) was implemented. As illustrated in Fig. 4.1(a), a setup consists of a high power 407 nm LED source (ENFIS). The Fresnel lens (Lens 1) focuses the LED through transparent grids from the foil through a 10x Tessar objective. This home-assembled objective by [11, 142] has a key advantage of being able to assemble with standard spherical lenses while still presenting excellent imaging properties. A chromium (Cr) of 200 nm thickness, coated on BK7 glass substrate (ø=25mm, t=1mm), was further coated with positive photoresist (more information in materials) and placed at the image plane, which was focused into the CCD camera. The optical imagining path is shown by solid white lines. After the illumination, the Cr layer was etched, producing the intermediate mask required for the next demagnification process.

Microscope Projection Photolithography

The final step of the photolithography process is to demagnify structures from the Cr mask into the final substrate. This process is achieved in the Microscope Projection Photolithography (MPP) [11, 142], another home-assembled setup by [143–145]. As illustrated in Fig. 4.1(b), the Cr mask prepared with 10 times demagnification was placed in the image plane of a first tube lens (Lens 1). A high power 365 nm UV LED (Roithner) was used for focusing the structures from Cr mask with Lens 2 onto a standard 18x18x0.15 mm^3 microscopic cover glass, coated with a desired photoresist. Depending upon the size of final structures, 10x or 100x microscope objectives can be considered. Additionally, a 650 nm red high-power LED was mounted to observe and focus the projection of the Cr mask. The choice of this wavelength is solely based on it having a longest wavelength in visible range and lowest energy, creating less effects in sample. A beam splitter projects reflected light from the sample onto the camera. The tube lens (Lens 3) is adopted for visualisation.

The schematic diagram of both process is shown in Fig. 4.2. The demagnification uses waveguides as an example, which is 300 µm at the start and is demagnified by 100x to 3 µm in final substrate.
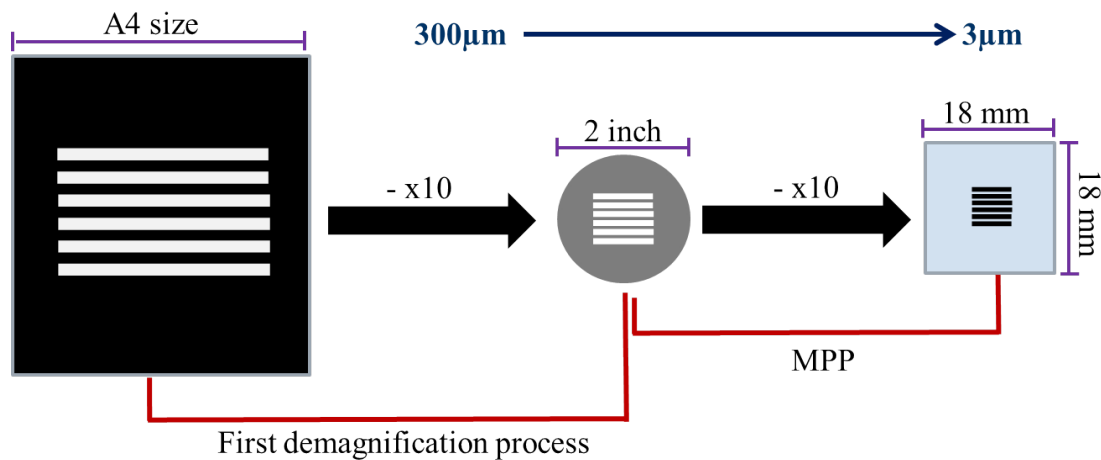
Fig. 4.2 The schematic diagram shows the process of photolithography process from the beginning. The diagram uses 10x objectives for both process.

4.1.2 Grating-coupling method
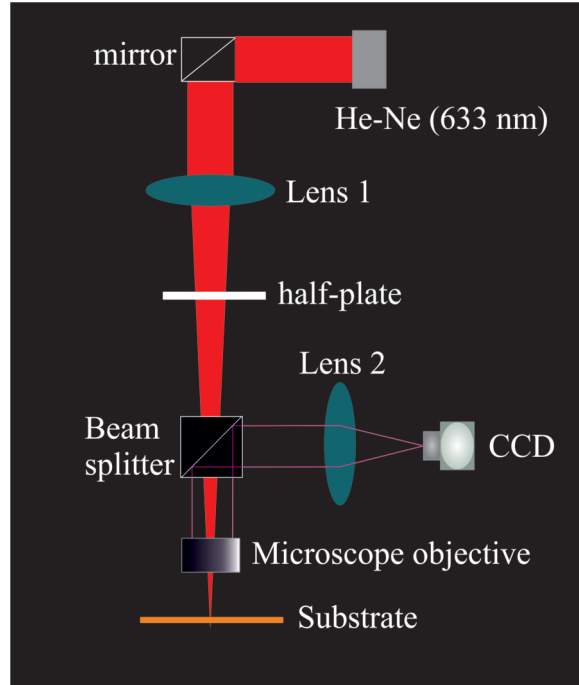
Fig. 4.3 Schematic diagram of the Grating-coupling method consists of He-Ne laser focused by Lens 1 and microscope objective (100x) into the sample, that consists of gratings with metal deposited on the top. The reflected light from the substrate is guided into the CCD camera by Lens 2.

The grating-coupling, regarded as one of the popular methods to investigate properties of SPPs is based on using grating as an approach to conserve momentum. The wave vector of the incident light is enhanced due to the normal diffraction modes of the gratings. This methods differs from Kretschmann configuration in a way that incident angle can be modified, not the effective refractive index that incident beam experiences. The main advantage of this technique is the diffraction angle and oscillating SPPs at a metallic surface can be effectively regulated by the dimensions of dielectric gratings.

The method is normally advantageous while investigating SPPs on thick metals since thin metals suffer from uncontrollable radiation losses. The incident light that hits the grating at θ with respect to the plane of incidence has a certain wave vector, which is altered once they are scattered. The wave vector, k_g of scattered light depends on the characteristics of the gratings period, a_g, by the equation [146]:

$$k_g = \frac{2\pi}{a_g} \tag{4.1}$$

The efficiency of these gratings determines the nature of diffracted orders, whose wave vector implies the behaviour of SPPs. The grating-coupling method, chosen for investigating properties of SPPs is shown in Fig. 4.3. The set-up was based on microscope projection, that focuses He-Ne (Roithner, 1mW) with Lens 1 through to the substrate. The (45:55) beam splitter was mounted in between the 100x microscope dry objective (Zeiss, NA =0.75) and the Lens 2 that collected the scattered laser from the substrate, directing towards the CCD camera. The $\lambda/2$ plate (Thorlabs) was installed in between the Lens 1 and beam splitter in order to monitor polarisation. Unless otherwise noted, for all the SPPs experiment described in this thesis, He-Ne laser was applied. The laser system used for this particular experiment is shown in Table. 4.1.

Table 4.1 Operating system of He-Ne Laser

Laser	He-Ne
Manufacturer	Roithner
Wavelength	633 nm
Operating mode	Continuous

For the evaluation, once the grids were synthesised using photolithography process (*Section 4.1.1*), gold and silver were deposited by evaporation and sputtering process (*Section 4.2.3*) at different sets of thicknesses. The thickness ranges from $\approx$20 nm to $\approx$85 nm. Two sets of grids were used, one for excitation and another for the out-coupling plasmons. Due to ohmic and scattering losses, the intensity of the plasmons decreases exponentially along the distance. This process can be described by the equation 4.2:

$$I(x) = I_0 e^{-Ax} \tag{4.2}$$

$$L_{SPP} = -\frac{\delta x}{ln\frac{I_1}{I_0}}$$

I_0 represents an initial intensity, I_1 represents a final intensity, δx represents a difference in distance with respect to I_0 and I_1. The exponential decay graph was plotted for different intensities with respect to their distances, and from the curve, L_{SPP} was estimated. This method is referred to as Method 1.

4.1.3   Leakage radiation microscope
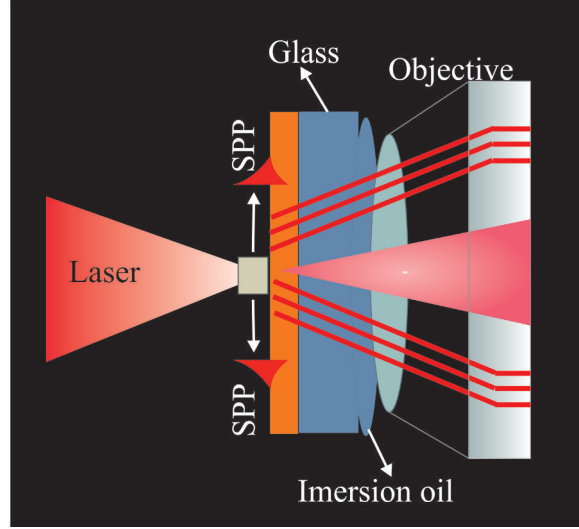
Fig. 4.4 The schematic diagram of the Leakage Radiation Microscopy Set-Up demonstrates the method to evaluate leaked radiation through the sample and the substrate. The refractive index of the glass is matched by using oil immersion that has similar refractive index to the glass.

For a flat metal surface, according to the dispersion curve in Fig. 2.1, SPPs excited within the light cone (light line of air and substrate) suffers from radiation loss into a high refractive index. The SPPs propagating in this region is defined by β, which is called propagation constant. The condition to achieve this losses is described by:

$$k_0 < \beta < k_0 n_s \tag{4.3}$$

where n_s is the refractive index of the substrate.

This losses can be measured to understand the properties of SPPs, by the LRM. The concept of this method has been widely studied by many scientists [147, 39, 40, 62] and is schematically shown in Fig. 4.4. In the set-up used, a laser is focused into the grating, using an aspheric lens with 4mm focal length and numerical aperture (NA) of 0.55. This initiates the propagating SPPs in both directions. The leaked radiations are captured by using a high NA oil immersion 100x objective. The NA of the objective, that detects the leaked waves is dependent on the complex effective index (n_{eff}) of the SPPs and the condition is met when:

$$K_{SPPs} = K_0 n_d Sin\theta_{SPPs} = K_0 n_{eff} \tag{4.4}$$

where, θ_{SPP_s} represents the incident angle. Additionally, the choice of high NA objective ensures a large angular spread of the focused excitation beam that includes and angle $\theta > \theta_c$, for total internal reflection.

This experiment is regarded as an additional method to understand the influence of the measurement methods in comparison with the grating-coupling method. Gold and silver with the thickness of $\approx$50 nm, fabricated by both evaporation and sputtering were evaluated with both grating-coupling and the LRM. This method is referred to as Method 2. Both laser systems demonstrated in Table. 4.1 and Table. 4.2 were used for this experiment.

Table 4.2 Operating system I of Femtosecond laser

Laser	Ti:Sa
Manufacturer	Kapteyn-Murnane
Model	MTS Mini Ti:Sa Laser Kit
Wavelength	800 nm
Operating mode	Continuous and Pulsed

4.1.4   Laser excitation of nanoparticles
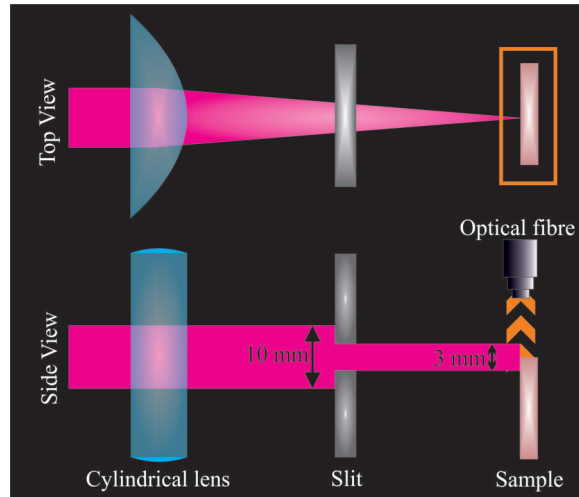
Fig. 4.5 A top view and a side view of the set represents a laser focused with a cylindrical lens (f=5cm) to the sample. A slit barrier is designated to control the laser focus length. The laser focus spot with length of 10 mm and a width of 45 μm, is focused at the edge of the film. An optical fibre, allocated perpendicularly close to the edge of the film measures the PL intensity of the illuminated area.

A gain measurement set-up, as shown in Fig. 4.5 consists of a laser beams with diameters of approximately 1 cm were focused onto the material layers by a cylindrical lens with a focal length of 5 cm. A micrometer-driven metal slit was introduced for manually controlling the slit width. The laser focus spot with a width of 45 μm, was focused at the edge of the film, so that the optically pumped line extends into the material layer when the slit was opened. By opening the slit only up to 3 mm the laser intensity remains constant, resulting in an interaction length on the sample of up to 1.5 mm. The laser power was varied by means of dielectric optical attenuators. The photoluminescence (PL) emission spectra of the NPs films were measured by positioning the fibre of a spectrometer (Ocean Optics) with a core diameter of 200 μm above the edge of the pumped zone of the sample. The cylindrical lens decreases the energy further by approximately 8 %. The investigated threshold energy were all measured after the slit barrier.

The advantage of cylindrical lens is, it focuses Gaussian beam into a line focus that consists of constant intensity throughout. This concept arranges the line to act as a waveguide, that guides the light in a certain direction. Without the line focus, the light does not have a definite direction, hence scatters in all directions. For this typical experiment, two sets of lasers were considered:

- Nanosecond pumping: The films were pumped by a neodymium-doped yttrium alu-minium garnet (Nd:YAG) laser, 3ω, at a wavelength of 355 nm, and a repetition rate of 14 Hz. The properties of two different nanosecond laser systems are listed in Table 4.3 and Table 4.4.

Table 4.3 Operating system I of nanosecond laser adopted for *Chapter 6, Section 6.1*.

Laser	Nd:YAG
Manufacturer	InnoLas Laser GmbH
Model	SpitLight DPSS
Wavelength	355 nm (3 ω)
Operating mode	pulsed @ 100Hz
Pulse duration	6 ns (FWHM)

Table 4.4 Operating system II of nanosecond laser adopted for *Chapter 6, Section 6.2*.

Laser	Nd:YAG
Manufacturer	Quantel
Model	BrilliantB
Wavelength	355 nm (3 ω)
Operating mode	pulsed @ 10Hz
Pulse energy @355 nm	165 mJ

- Femtosecond pumping: The Ti:Sa laser with a pulse duration of 50 fs was operated in two different system modes: (i) Fundamental (800 nm) at repetition rate of 50 Hz, (ii) 2ω (400 nm) at repetition rate of 20 Hz. The properties of the laser system is listed in Table 4.5.

Table 4.5 Operating system II of femtosecond laser adopted for *Chapter 6, Section 6.1*.

Laser	Ti:Sa
Manufacturer	Spectra-Physics
Model	Spitfire
Wavelength	800 nm
Operating mode	pulsed @ 1KHz
Average power	3.5 W

The experiment was evaluated in the scheme of two different categories:

Power variation

The slit was kept completely open to let half of the laser beam to excite the sample. The ASE threshold energy and the fluorescence spectra were collected by changing the laser intensity to different levels.

Interaction length variation

Once ASE was achieved, the power was kept constant at one particular value and the slit was opened slowly until the emission was detected. The fluorescence spectra was measured at every 500 μm opening.

For the investigation of two-photon absorption in *Chapter 6, Section 6.3*, another set of tunable femtosecond laser was adopted, as listed in Table 4.6.

Table 4.6 Operating system III of femtosecond tunable laser adopted for *Chapter 6, Section 6.3*.

Laser	Ti:Sa
Manufacturer	Coherent
Model	Chameleon
Wavelength	Tunable (705-980) nm
Operating mode	pulsed @ 80 MHz
Average power	3 W
Pulse duration	<140 fs

4.2   Materials

4.2.1   Photocurable polymers

Ormocore

Organically modified ceramics (ORMOCERS) are the group of polymers, developed at the Fraunhofer institute for silicate research ISC. It has been regarded as an advanced materials for photonics applications due to minimal shrinkage during polymerisation. The advantage of this materials is, they have high thermal and mechanical stability due to the fact that they contain both organic and inorganic compounds. It is a negative photoresist and is synthesised in a sol-gel process. The material was used as it was bought without further modification. However, to create the cross linking, standard Irgacure (IR)-369 (Ciba Specialty Chemicals) was added. This photoresist was chosen over other IR, such as IR-184, IR-651, IR-500, IR-907, IR-290, IR-819, IR-2100 and IR-2959 for its high absorption ability at 365 nm. The absorption spectrum for this particular photoresist is shown in Fig. 4.6. As demonstrated in the figure, the spectrum can be altered with the change in amount of acetonitrile in the solution. The change in the refractive index of the resist is also expected with polymerisation [148]. The choice of this material in this thesis is particularly due to its solubility in organic solvents; toluene, which is a common solvent to disperse semiconductor NPs. Among the different class of polymer categorised under ORMOCERS, ormocore is adopted as they are typically designed for waveguides synthesis.
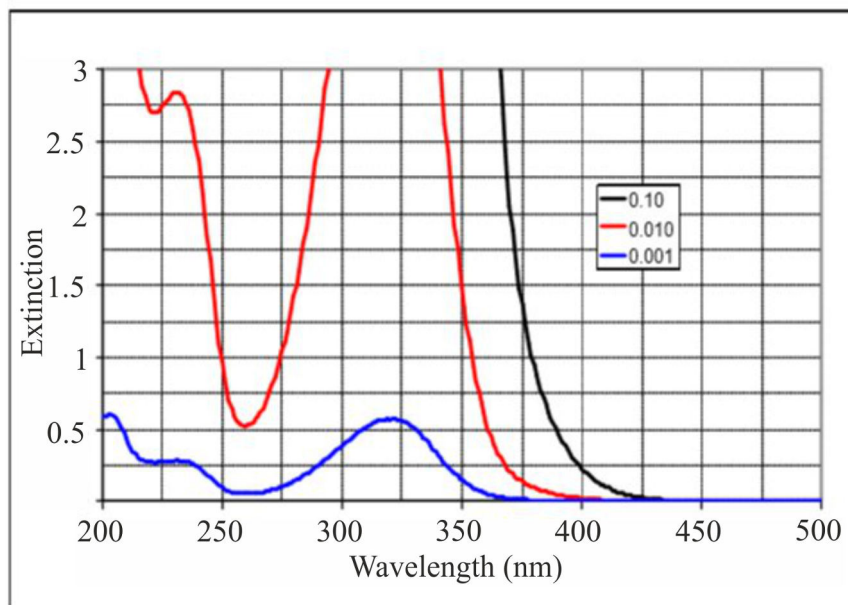
Fig. 4.6 The extinction of photoinitiator IR-369 with different % in acetonitrile.

Ormosil

In order to excite SPPs, one can fabricate grids as subwavelength scattering lines. Before the metal deposition process, the polymer grids were synthesised on the glass substrate in two-step photolithography process (*Section 4.1.1*). To synthesis these lines, the choice of materials is crucial. The choosing criteria are based on its solubility with the photoinitiator (PI) that absorbs the adopted wavelength for exposure in photolithography process. Additionally, the material should also be stable in the structural form once it is developed. Based on the available experimental set-ups and the structures required for different applications, a perfectly matched photoresist, known as Organically modified Silica (ORMOSIL) was synthesised.

Table 4.7 Chemicals required for the synthesis of Ormosil.

Chemicals	Specialty Companies
Methacryloxypropyltrimethoxysilane (MAPTMS), 99%	Sigma Aldrich
Zirconium n-proxide, (ZPO), 70% in propanol	Sigma Aldrich
Methyl Methacrylate (MMA)	Fluka
Hydrochloric acid solution (HCL), 0.1 M	Sigma-Aldrich
Deionised water (D-H_2O)	–
1-propanol	Sigma Aldrich

A sol-gel negative photoresist from a class of ORMOSIL were synthesised at the Laser Zentrum Hannover e.V. with the materials listed in Table 4.7 [149]. The alkoxysilane groups of MAPTMS with ZPO serve as an inorganic network. The molar ratio of MAPTMS to ZPO can be varied from 10:0 to 1:1 [148]. Due to difference in between the reactivity of alkoxysilane and zirconium precursor, synthesising procedure mainly requires three steps, consisting of hydrolysis process to form porous mutual cluster. The synthesis is carried out in following steps:

- (1) MAPTMS is hydrolised with HCL in ≈10:1 volume ratio and the solution is stirred for ≈40 minutes.

- (2) In a separate bottle, ZPO is chelated with MAA in ≈3:1 volume ratio and stirred for ≈40 mins.

- (3) Solution (1) and (2) are mixed together and stirred for ≈45 minutes.

- (4) ≈5% of water is mixed in solution (3) and stirred for ≈24 hours.

The choice of HCL as a hydrolysing agent was to compensate the immiscible nature of MAPTMS with water. After enough stirring, the production of methanol and the hydrolysis

of alkoxysilane groups allows the solution to generate miscible property in the solution. After the final procedure, a PI that has higher absorbance around the wavelength intended to use for photo-polymerisation, was added, followed by 2 hours stirring. In this thesis, most common PI, IR-369 that was sensitive to irradiation at wavelengths less than 390 nm was used at ≈4 wt%. The material was then filtered using 0.22 μm filters to avoid big lumps of agglomerated particles. As a result, a viscous and transparent solution was ready for the synthesis of nano-mm sized structures.

Optical and physical properties of Ormosil

To generate a required film thickness, sythesised ormosil can be diluted with 1-propanol. The measured thicknesses of ormosil/1-propanol in the ratio of 1:3 and 1:4 is shown in Fig. 4.7. The film was prepared by spin-coating on a standard 18x18x0.15 mm^3 microscopic cover glass.
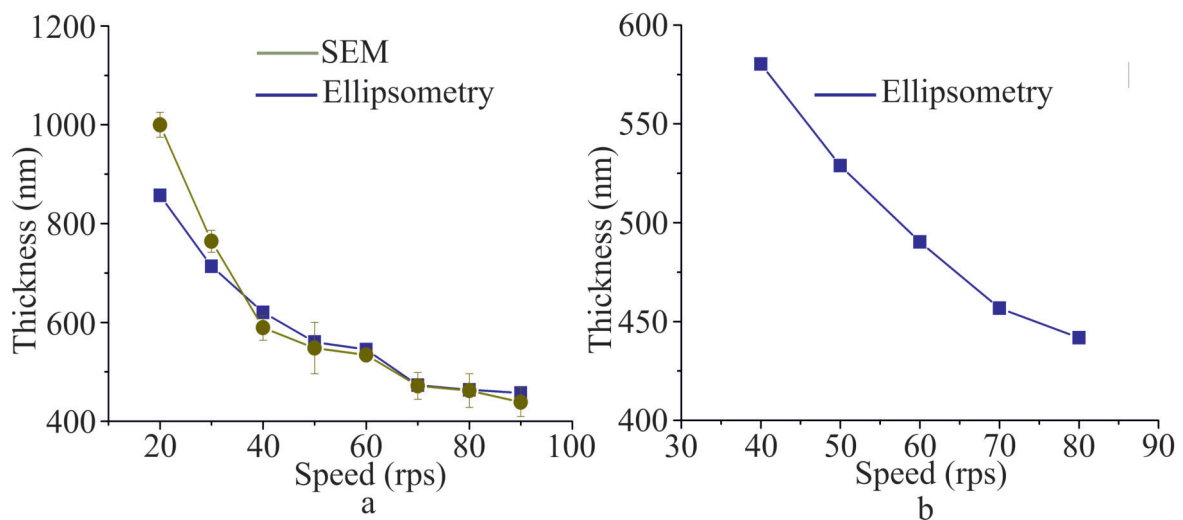
Fig. 4.7 Diluted ORMOSIL with 1-propanol in the ratio of (a) 1:3 and (b) 1:4 to achieve required thicknesses. The thickness is measured with ellipsometry. For the dilution 1:3, thickness measurement is compared with SEM.

The thickness measurement was carried out with ellipsometry [150] (SENTECH SE 800). The white light source with p and s polarisation, in the wavelength range of 400 nm–800 nm was inclined at Brewster angle (70°). The reflected light from the sample at similar angle was captured by a detector. The analysis was done based on an amplitude ratio, ϕ and the phase difference, δ in comparison to incoming light. The ratio of Fresnel reflection coefficients, R_p and R_s for p and s-polarised light are related to ϕ and δ by equation (4.5). This equation accounts for both incoming and reflected light.

$$\tan(\phi)e^{i\delta} = \frac{R_p}{R_s} \tag{4.5}$$

In order to estimate the standard deviation, the thicknesses were additionally measured with SEM for 1:3 dilution. As shown in Fig. 4.7(a), for the thicknesses lower than $\approx$700 nm (within the excitation wavelength range), trend lines for both ellipsometry and SEM are within error values of 2.5%. Since the dilution of 1:4 will be thinner in comparison to 1:3, less error was expected and the measurement was carried out with ellipsometry only, as shown in Fig. 4.7(b).

The investigation of absorption and transmittance of the material once the PI was added was carried out to understand its absorption properties. The characterisation was done in UV/Vis PL spectrometer (Perkin Elmer).
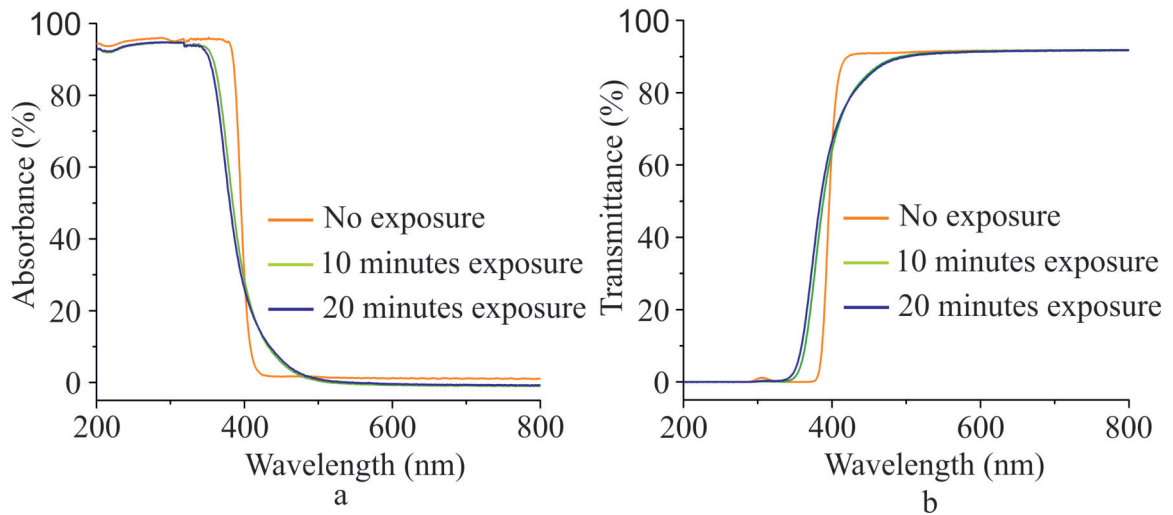
Fig. 4.8 The measurement of absorbance (a) and transmittance (b) of ormosil films with PI IR 369 shows almost 100% transmittance above 400 nm. Following exposure to UV LED (365 nm) for 10 minutes and 20 minutes, both absorbance and transmittance spectrum are shifted towards the lower wavelength.

The measurement of absorbance (Fig. 4.8(a)) and transmittance (Fig. 4.8(b)) of ormosil films with PI, IR-369 shows almost 100% transmittance above 400 nm, making it suitable for Vis-NIR optical applications. The absorbance graph supports the transmittance data by demonstrating the material can be polymersied by the wavelength up to 400 nm. For the UV lithography in this thesis, 365 nm LED was considered.

Next to that, the influence of an exposure time on optical properties was also analysed. As presented in the Fig 4.8, both transmittance and absorbance declared some changes of the spectrum to slightly curved, with the bands shifting towards lower wavelength. The curve

between 'No exposure' and '10 minutes' exposure has a huge difference in comparison to the curve between 10 minutes and 20 minutes exposure. This changes could have been raised from the Zr complex [151]. According to [151], when Zr content is increased in the solution, a bathochromic effect if observed. This content consists of strong polarisability and electropositivity that approaches to electrons donors groups such as amino and carboxyl groups in the PI [151]. The blue-shifting of the absorption and transmittance curve indicates the possibility of interaction between this material with light. Since the subwavelength scattering lines needed for this experiment required less than a minute as an exposure time, this shifting of the curve is not considered that detriment.
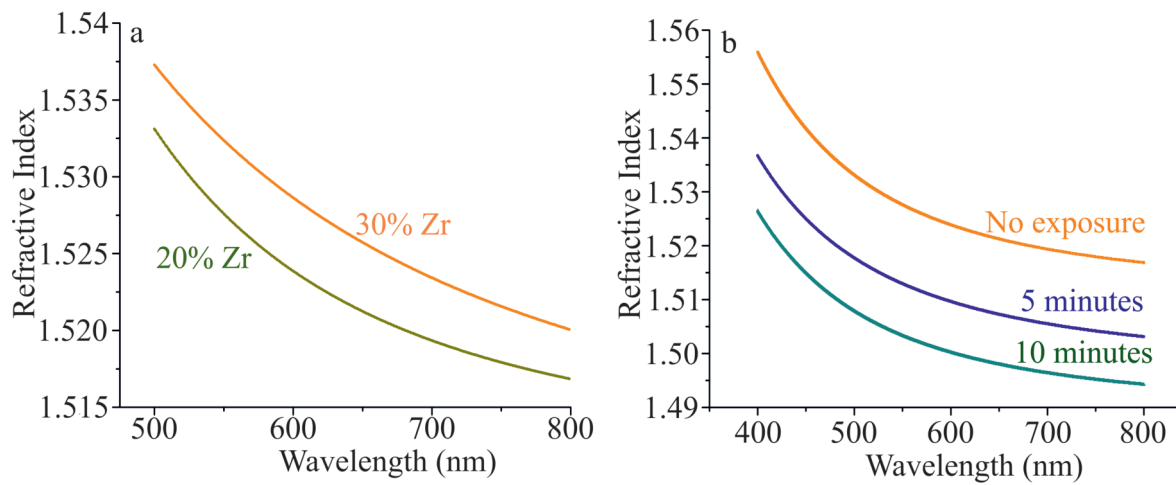
Fig. 4.9 The change in Zr precursor in the ormosil synthesis observed the change in the refractive index of the ORMOSIL.(a) represents the ZPO with 20% (green) Zr and 30% Zr (orange). Additionally, the influence of exposure time on the refractive index (b) demonstrates decrease in refractive index after 5 minutes and further decrease in 10 minutes exposure.

According to [148, 151], the refractive index of the material can be altered by controlling the amount of Zr precursor. This theory was experimented by changing the content of Zr precursor. Thin films of two solutions were prepared separately by spin-coating on a standard 18x18x0.15 mm^3 microscopic cover glass. The films were evaluated also in ellipsometry and the result was confirmed by Python programming calculation, using Cauchy equation, 4.6.

$$N(\lambda) = N_1 + \frac{N_2}{\lambda^2} \tag{4.6}$$

Fig. 4.9 shows the trend lines for 20% and 30%, as the content of Zr precursor was increased, the refractive index was increased. Additional investigation was carried out to understand the behaviour of refractive index with 30% Zr once it was exposed to UV light (365 nm). The data can be visualised in Fig. 4.9(b). Remarkably, when the materials was exposed for

5 minutes (blue line), the refractive index decreased. Afterwards, further exposure of same sample for 10 minutes decreased the refractive index further. This kind of behaviour can be the representation of interaction between the material and the PI. The fact that this degree of sensitivity on the refractive index with respect to the Zr content and the exposure time increases the prospect of manufacturing more desired structures for various applications.

4.2.2   Atomically flat crystalline gold flakes

The synthesis of atomically flat crystalline gold flakes (Au^F) was carried out by Dominik Hinrichs under the supervision of Dr. Dirk Dorfs from Institute of Physical Chemistry and Electrochemistry in the Leibniz University Hannover in co-operation with the Laser Zentrum Hannover e.V. The synthesis was adopted from the procedure developed by Hecht's group [152], using the materials listed in Table A.2. The synthesis was carried out directly on desired substrates in a gold precursor solution. In a Falcon tube, ethylene glycol (20 mL) was mixed with 180 µL of gold(III)chloride hydrate (39.4 mg) dissolved in water (1 mL). A silicon or glass substrate (18x18 mm^2) was placed into the solution and kept vertical by a plastic construction. The solution was slightly stirred and was pre-heated for 20 min in a water bath at 50°C. Afterwards, 180 µL of an aniline solution in ethylene glycol (0.1 M) was slowly injected into the reaction solution and stirred further for 5 minutes. The reaction vessel was placed in an oven at 50°C for 72 hours. The substrates were then cleaned by rinsing with water and acetone. As a result, triangular and hexagonal Au^F were achieved, as shown in Fig. 4.10.
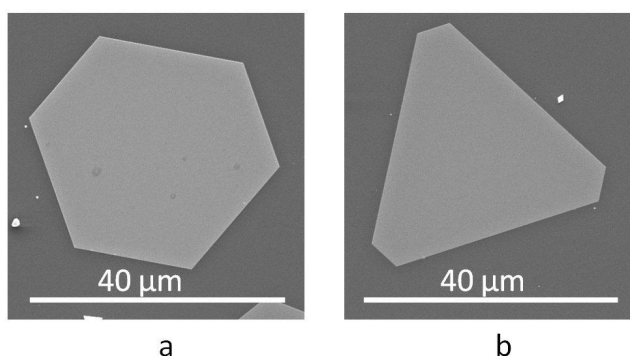
Fig. 4.10 The Au^F synthesised on silicon substrate, contain both (a) triangular and (b) hexagonal in shape. The thickness of the flakes varies in the range of 20-90 nm in different flakes but remains constant in one flake.

4.2.3 Polycrystalline gold and silver films

Subsequent to the synthesis of the grids, four sets of samples; evaporated gold (Au^E), sputtered gold (Au^S), evaporated silver (Ag^E) and sputtered silver (Ag^S), with different thicknesses were prepared with a thermal evaporation and an e-beam sputtering. The sputtering (EM ACE 600 Firma Leica) was carried out at the speed of 1.1-1.5 Å/s and the thermal evaporation (Edwards, Auto 306 Evaporation System) at 1-2 Å/s. Both gold and silver wires used for the evaporation were 99.99% pure with 1 mm diameter. The gold and silver used for sputtering were 99.95% and 99.97% pure respectively.

4.2.4 Polycrystalline gold flakes

The poly-crystalline gold flakes (PAu^F) were prepared by photolithography process (*Section 4.1.1*). The positive photoresist S1813 (Dow Chemical) was used for both demagnification processes. First, the resist was used for demagnifying structures from transparent foil into the Cr mask. The development process removed the exposed part. Next, the structures were demagnified further by 100 times using MPP *(section 4.1.1)*.
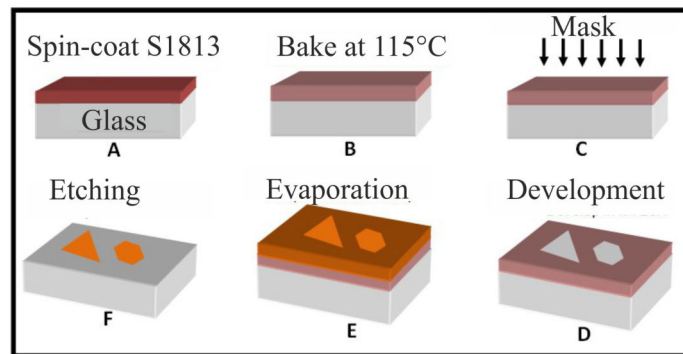
Fig. 4.11 The schematic diagram of preparation of PAu^F.

The procedure, shown in Fig. 4.11 consists of the positive photoresist, S1813 spin-coated on 18x18x0.15 mm^3 glass slide (A) followed by baking at 115°C for 1 minute (B). The film was exposed to 365 nm laser diode for 100 ms (C). Afterwards, the sample was developed in MF26A (D), standard developer for the resist S1813. After rinsing with water and blow dry process, gold evaporation (E) was carried out on the top, using similar process as described in *section 4.2.3*. The final stage consist of a lift-off process (F), that requires dissolving unexposed S1813 in acetone. As the result, ≈50 nm thick PAu^F with the size of ≈25 μm was achieved as shown in Fig. 4.12.
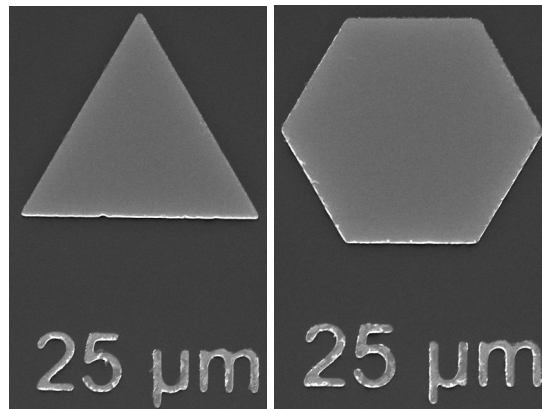
Fig. 4.12 The example of triangular and hexagonal PAu^F. These flakes are $\approx$50 nm thick. The size of the flakes from one end to another is $\approx$25 µm.

4.2.5   Semiconductor nanoparticles

The arrangement of core/shell NPs have previously demonstrated high PL quantum yields (QY), as high as 50-80% [153–156]. Additionally, core/shell NPs are also thermally and chemically more stable, making it suitable for sensing applications. Recent progress in the synthesis process has made a possibility to obtain highly luminescent plain core NPs. However, their instability makes them less preferable when it comes to applications [157, 158], such as biomedical [159, 160] and lasers [19]. Additionally, core/shell NPs typically are more stable against photooxidation [154]. The choice of CdS over ZnS (commonly used shell) as a shell is due to lower bandgap of CdS (2.4 eV) in comparison to ZnS (3.7 eV) [161]. Additionally, ZnS also suffers from disadvantageous spectral properties such as photon antibunching and dark state emission at low temperature [162]. The size of the core also play important role. Larger CdSe core dimensions results in fast radiative lifetimes and absence of photon antibunching [162].

The synthesis of NPs was carried out in co-operation with Dr. Suraj Naskar from Institute of Physical Chemistry and Electrochemistry in Leibniz Universität Hannover under the supervision of Dr. Nadja-Carola Bigall and Dr. Dirk Dorfs. Three types of NPs were chosen based on their size and morphology; CdSe/CdS core/shell QDs, CdSe/CdS core/shell QRs and 5 ML thick CdSe/CdS (core/crown) QWs. The materials are listed in Table B.1. Their synthesis processes are described more in detail below:

Synthesis 1: CdSe/CdS core/shell QDs
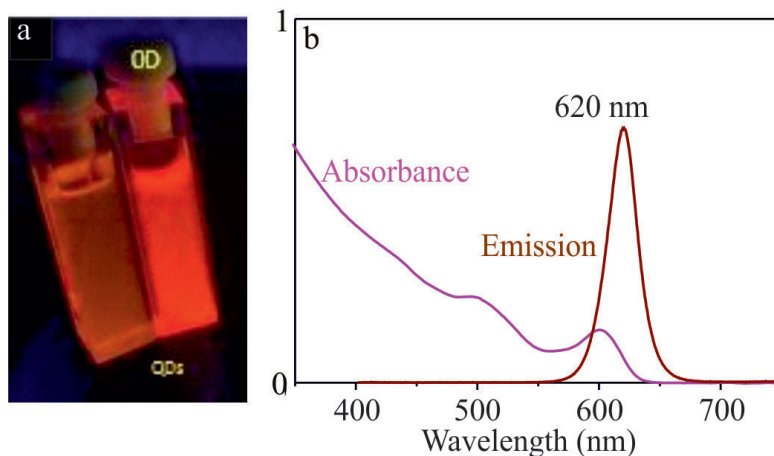
Fig. 4.13 (a) CdSe core (left), CdSe/CdS (right) core/shell QDs, illuminated under UV light with their (b) absorption and emission spectra.

For the synthesis of QDs, successive ionic layer adsorption reaction (SILAR) was chosen as it was proven to be a successful technique for these kind of synthesis. The synthesis procedure was adopted from [156]. The procedure consists of a two step synthesis with preparing CdSe seeds, followed by coating with one CdS layer via SILAR. After the synthesis and purifications the QDs were dispersed in 4 mL toluene. The particles have strong absorption around 355 nm, and emitting at 620 nm. The optical parameters and physical appearance are shown in Fig. 4.13.

Synthesis 2: CdSe/CdS core/shell QRs

The CdSe seeds were synthesised following the procedure of [163] with slight modification. A seeded-growth approach was based on the reaction procedure mentioned in the same literature. The mixture of 0.06 g of CdO (99.99%), 3.0 g of TOPO (99%), 0.28 g of ODPA (99%) and 0.08 g of HPA (99%) were placed in a three neck flask and degassed under vacuum for 1 h at 150°C. Afterwards, the reaction temperature was raised to 300°C under argon atmosphere. At the same temperature, 1.8 mL of TOP was injected and the solution was heated to 380°C under argon. Upon achieving this temperature, a sulfur precursor solution (0.130 g S dissolved in 1.8 mL TOP) consisting of CdSe seeds in toluene (concentration of CdSe was 400 µM) were dissolved was quickly injected. The temperature was decreased down to 270-300°C and the reaction was continued for 8 minutes before removing the heating mantle. The products were purified by centrifugation 3600 g (rcf) for 15 min and the

precipitate was dispersed in 4 mL toluene. The optical parameters and physical appearance as shown in Fig. 4.14 have strong absorption around 355 nm and emission at maximum wavelength of 621 nm.
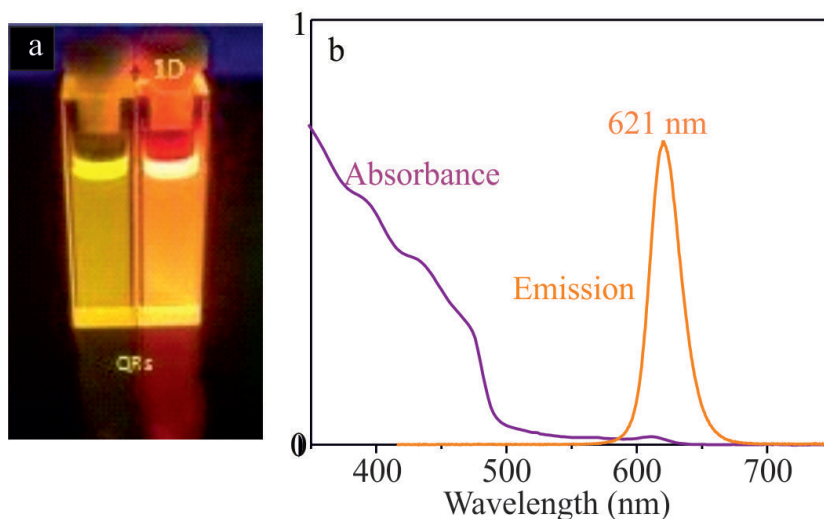
Fig. 4.14 (a) CdSe core (left), CdSe/CdS (right) core/shell QRs, illuminated under UV light with their (b) absorption and emission spectra.

Synthesis 3: 5 ML thick CdSe/CdS (core/crown) QWs

These particles were synthesized according to the procedure described by [162] with little modifications. A mixture of 170 mg cadmium myristate $Cd(myr)_2$ and 14 mL of ODE (90%) inside a 25 mL three neck flask was degassed under vacuum at 100°C for one hour with continuous stirring. Afterwards, the temperature of the reaction medium was increased up to 250°C under argon flow, followed by injecting 1 mL of selenium precursor (12 mg Se dispersed in 1 mL of ODE) into the mixture. Exactly one minute after Se injection, 120 mg of $Cd(OAc)_2.2H_2O$ was added to the mixture. After 10 min at 250°C, the reaction was stopped and 1 mL oleic acid was added. The CdSe QWs were separated by using 3:1 hexane:ethanol mixture.

In a mean time, an anisotropic CdS growth mixture was prepared by dissolving 480 mg of $Cd(OAc)_2$, 340 μL of oleic acid and 2 mL of ODE at 150°C for 15 min. Into the mixture, 3 mL of a 0.1 M sulfur (in ODE) precursor solution was added once the reaction temperature was lowered down to room temperature.

The precipitate of CdSe QWs was re-dispersed in 10 mL ODE and was placed inside a flask for the next step of lateral extension of CdS crown growth. After degassing CdSe core

at 100°C for an hour, the temperature was elevated to 240°C and an anisotropic CdS growth mixture was continuously injected (using a syringe pump) at a rate of 8 mL/h into the above solution for 10 min. Afterwards, the heating mantle was removed. The core/crown QWs were separated from the mixture by adding 15 mL of ethanol followed by centrifugation at 3600 g relative centrifugal force (rcf) for 15 min. The precipitate was dispersed in 4 mL hexane. The optical parameters and physical appearance are shown in Fig. 4.15. Similar to QDs and QRs, QWs has strong absorption around 355 nm, emitting at maximum wavelength of 554 nm.
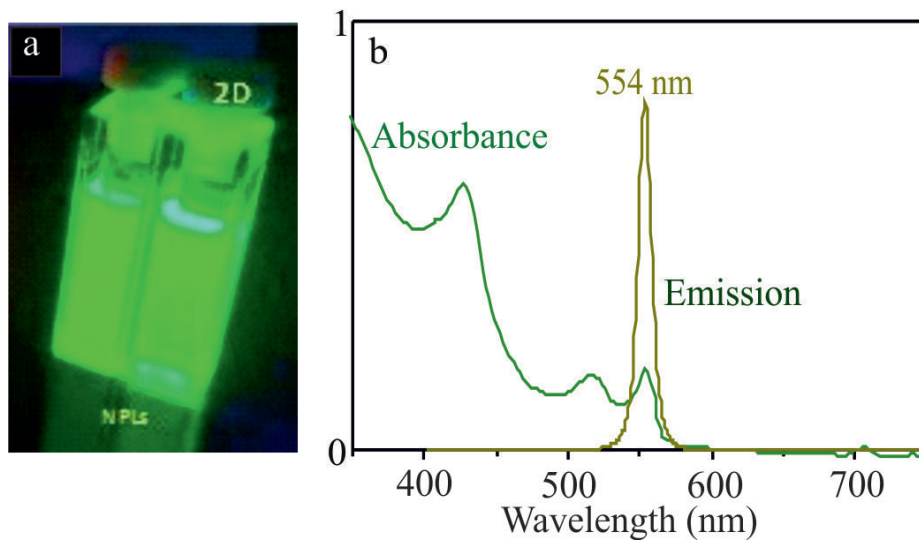
Fig. 4.15 (a) CdSe core (left), CdSe/CdS (right) core/crown QWs, illuminated under UV light with their (b) absorption and emission spectra. Note, in Fig. (a), NPLs is another term of quantum wells.

The concentration of the Cd ion is also investigated by the method explained in *Appendix B.1*. The measured concentration are listed in Table. 4.8.

Table 4.8 Concentration of NPs.

Samples	Cd ion Concentration (mMol)
QDs	36.40
QRs	71.92
QWs	29.67

The QY measurement is explained in detail in Appendix B.2 and the measured values are listed in Table. 4.9.

Table 4.9 Quantum yield of NPs.

Quantum Yield of Particles	
QDs	19.19 %
QRs	64.39 %
QWs	48.77 %

Transmission electron microscopy

A FEI Tecnai G2 F20 TMP (Cs = 2 mm, CC = 2 mm) equipped with a 200 kV field-emission gun was used for the transmission electron microscopy investigation. This analyses was used for determination of sizes as well as to confirm the appropriation of core/shell/crown. The samples were purified 3-4 times via precipitation with methanol/ethanol and re-dispersion in toluene/hexane prior to TEM grid preparation. Subsequently, one drop of the purified sample was placed on a carbon coated copper TEM grid and dried under ambient conditions. The TEM images of QDs, QRs and QWs are shown in Fig. 4.16(a-c), respectively.
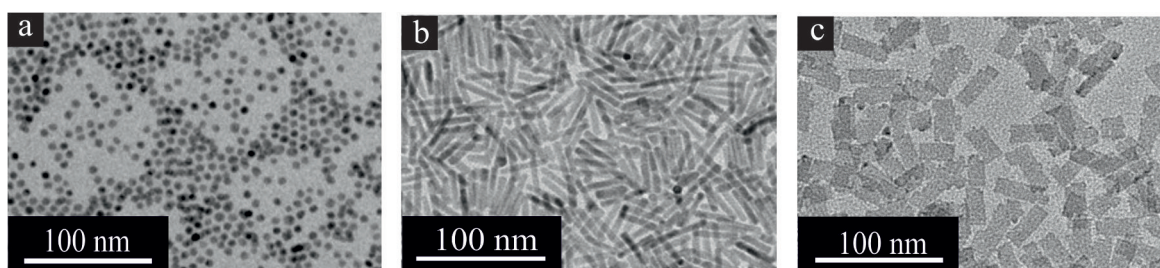
Fig. 4.16 TEM images of QDs (a), QRs (b) and QWs (c), showing size dimensions.

Chapter 5

Investigating surface plasmon polaritons propagation length on metallic films

The theoretical analysis approves the possibility of surface plasmon polaritons (SPPs) being influenced by the metal film quality. This can be realised by achieving the films with different fabrication processes. Additionally, it was also acknowledged that the thickness of the metal film influences the propagation of the SPPs. In this chapter, the investigation of how different metals, such as gold and silver of different thicknesses, prepared with different techniques and evaluated in different experimental techniques attribute to the SPPs losses is carried out. The poly-crystalline metals; evaporated gold (Au^E), sputtered gold (Au^S), evaporated silver (Ag^E) and sputtered silver (Ag^S) are the pre-eminent focus of the research. Two metals; gold and silver, which are commonly used in SPPs evaluation, are chosen. For each metal, two types of deposition approaches are considered, thermal evaporation and e-beam sputtering. For the excitation of SPPs, polymer grids on the sample surface are used. The SPPs are excited by a He-Ne (633 nm) and the propagation length (L_{SPP}) are measured by grating-coupling method and the leakage radiation microscopy (LRM). Dependence of L_{SPP} on the film thickness is also investigated. In the case of grating-coupling method, the L_{SPP} is estimated based on the out-coupled plasmons from grids (in poly-crystalline metals) and grooves (in mono-crystalline gold), and the comparison is done on each metal with respect to different deposition approaches and measurement methods. Additionally, for the comparison, atomically flat crystalline gold flakes (Au^F) and polycrystalline gold flakes (PAu^F), synthesised in *Section 4.2.2* and *Section 4.2.4*, respectively are also examined.

5.1 Synthesis of polymer grids for SPPs excitation
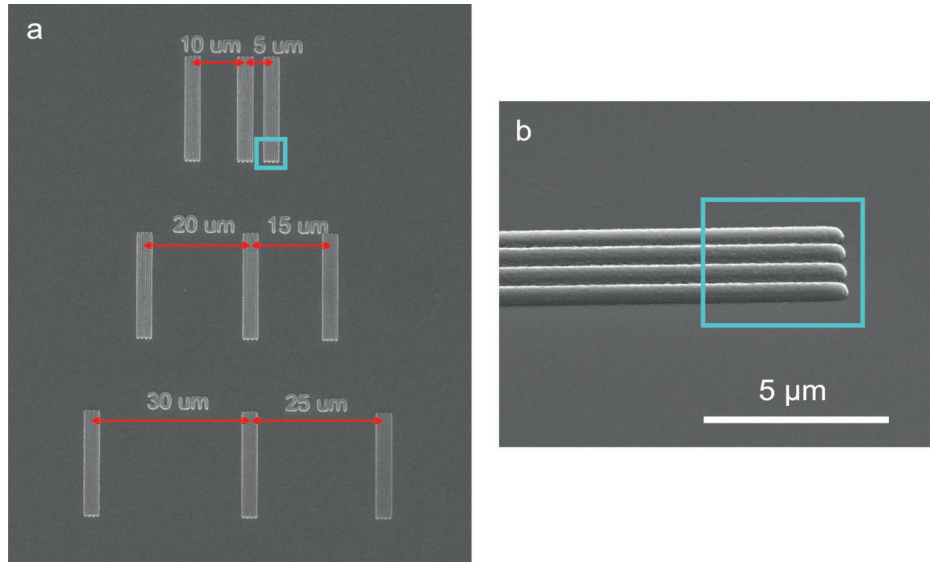
Fig. 5.1 A sample of SEM image of grids at different distances. Each grid is about 400 nm in width and 300 nm high. Similar samples were used for evaporation and sputtering gold and silver. The distances between different grids (centre to centre) are labelled with red arrows.

The subwavelength scattering lines as grids were synthesised with ormosil (*Section 4.2.1*), using photolithography method (*Section 4.1.1*). In the first stage, the grids of required size at six different distances, starting from 5 μm to 30 μm in an interval of every 5 μm were designed in CorelDraw and printed onto an A4 size transparent foil. These structures were then demagnified by 10x by illuminating a foil with a 410 nm high power LED source (ENFIS) on a chromium glass substrate (diameter=25 mm, thickness=1 mm), spin-coated with a positive photoresist, S1805 (Dow Chemical) at 50 revolution per second (rps) for 30 seconds. The resist was developed in MF26A (micro resist technology GmbH), and the chromium layer under the developed resist was etched with an aqueous basic solution with 10.9% ceric ammonium nitrate and 4.25% perchloric acid.

Next, the structure on chromium mask was demagnified by 100 times by using MPP. Ormosil was spin-coated on a standard 18x18x0.15 mm^3 microscopic cover glass, and baked at 115°C for 5 minutes. Afterwards, a 365 nm high power UV LED (Roithner) was used for focusing the structures from chromium mask with a 100x oil immersion microscope objective (Zeiss) onto a ORMOSIL coated glass. Subsequent to the exposure, the film was baked for another few minutes. During this baking, the irradiated part becomes strong, leading the non-irradiated polymers to be removed during development in isopropanol. The development process can be done in ethanol as well. Nevertheless, after development, the sample was

rinsed with ethanol and blow dried. As a result, the grids as subwavelength scattering lines as shown in Fig. 5.1 were synthesised in order to excite the plasmons. Each grid consist of period of 400 nm that includes four lines with ≈400 nm in width and ≈300 nm in height.

On top of synthesised grids, the metal was deposited, as described in *Section 4.2.3*. The thicknesses of the metal were measured using X-ray diffractometry with the help of Dr. Dominic Tetzlaff from Institute of Electronic Materials and Devices in Leibniz Universität Hannover. Afterwards, the thicknesses were compared with the calculation values based on light transmittance in our lab. The comparison gave the thickness values close to each other within th error range of 2%. The evaluation of the thickness based on transmittance was carried out by exciting the sample with halogen microscope light bulb and collecting the transmitted light by optical fibre. Based on the transmitted light, the thickness was calculated using Fresnel equations.
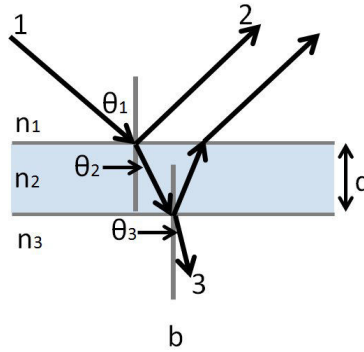
Fig. 5.2 The behaviour of light going from medium 1 to medium 2 and spontaneously to medium 3.

The Fresnel equations describes the behaviour of the light when it passes from one media to another with different refractive indices as shown in Fig. 5.2. The incoming light (1) hits the interface n_1 and n_2 at an angle of θ_1. Some of the light is reflected (2) at the border. The transmitted light goes out at an angle, θ_2. The reflectance and transmittance of p polarised light from medium 1 to 2 is explained by:

$$r_{12}^{P} = \frac{n_2 Cos\theta_1 - n_1 Cos\theta_2}{n_2 Cos\theta_1 + n_1 Cos\theta_2} \tag{5.1}$$

$$t_{12}^{p} = \frac{2n_1 Cos\theta_1}{n_1 Cos\theta_2 + n_2 Cos\theta_1} \tag{5.2}$$

where, r_{12}^{P} and t_{12}^{P} represent the reflectance and transmittance of p polarised lights from medium 1 to medium 2, n_1 and n_2 are refractive indices of medium 1 and 2, and θ_1 and θ_2

are the incoming and outgoing angles.

Similarly, the properties of p-polarised light traveling from medium 2 with refractive index n_2 and medium 3 with refractive index n_3 can be described by equation 5.3 and 5.4.

$$r^p_{23} = \frac{n_3 Cos\theta_2 - n_2 Cos\theta_3}{n_3 Cos\theta_2 + n_2 Cos\theta_3} \tag{5.3}$$

$$t^p_{23} = \frac{2n_2 Cos\theta_2}{(n_2 Cos\theta_3) + (n_3 Cos\theta_2)} \tag{5.4}$$

The phase difference of the light in the film thickness 'd' can be described by the equation 5.5.

$$\beta = 2\pi \frac{d}{\lambda} n_2 Cos\theta_2 \tag{5.5}$$

The transmittance coefficient is calculated as follows:

$$t = \frac{t^p_{12} t^p_{23} exp(\beta i)}{1 + (r^p_{12} r^p_{23} exp(\beta 2i))} \tag{5.6}$$

Hence, the thickness dependence transmittance is calculated by:

$$T = (\frac{abs(t)^2 n_3 * Cos\theta_3}{n_1 * Cos\theta_1}) * 100 \tag{5.7}$$

where, r^P_{23} and t^P_{23} represent the reflectance and transmittance of p polarised lights from medium 2 to medium 3, n_2 and n_3 are refractive indices of medium 2 and 3, and θ_2 and θ_3 are the incoming and outgoing angles.

Using the equations 5.1-5.7, and taking the dielectric constants of metal from [50], the thickness dependence transmittance was calculated using Python programming for a single wavelength of 600 nm. Note, similar calculation can be carried out for other wavelengths. The result is shown in Fig. 5.3, with the code for the calculation in Appendix (*Section A.3*).
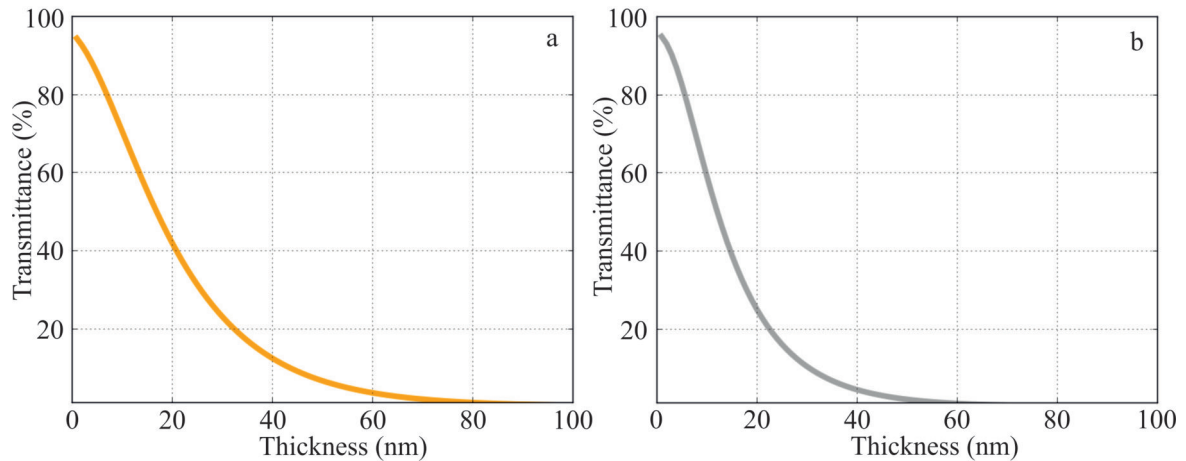
Fig. 5.3 Transmittance and thickness relationship of gold (a) and silver (b) at the wavelength of 600 nm.

From the calculation of transmittance (%) based on the thickness (nm), one can say that the transmittance on the silver is less than on gold in respective thickness. This indicates the silver to have less absorbance. This also demonstrates that silver has better propagating properties on the metal surface due to less absorption.

5.2   Excitation of surface plasmon polaritons

In both cases of deposition methods in poly-crystalline metal, same films of different thicknesses were considered in two different measurement methods; (i) Grating-coupling (Method 1 from *Section 4.1.2*), measuring the scattered plasmons from the grids/grooves and (ii) LRM (Method 2 from *Section 4.1.3*), measuring the leaked radiation along the metal surface.

Fig. 5.4(a) represents the Method 1. The plasmons were excited with He-Ne (JDSU Novette) at 633 nm on the right grids of each case and polarised horizontally, and were captured from the left grids. The laser beam was focused with a 100x long distance microscope objective. The out-coupled plasmons from the adjacent grids was captured by a CCD camera (The imaging source). In Method 2 as shown in Fig. 5.4(b), the same excitation wavelength was focused on the structure and the leaked radiation was collected by a 100x oil immersion microscope objective along the propagating line as shown in Fig. 5.4(d). Fig. 5.4(c,d) shows the example of excited grids with 633 nm on 60 nm Ag^S, using Method 1 and Method 2 respectively.
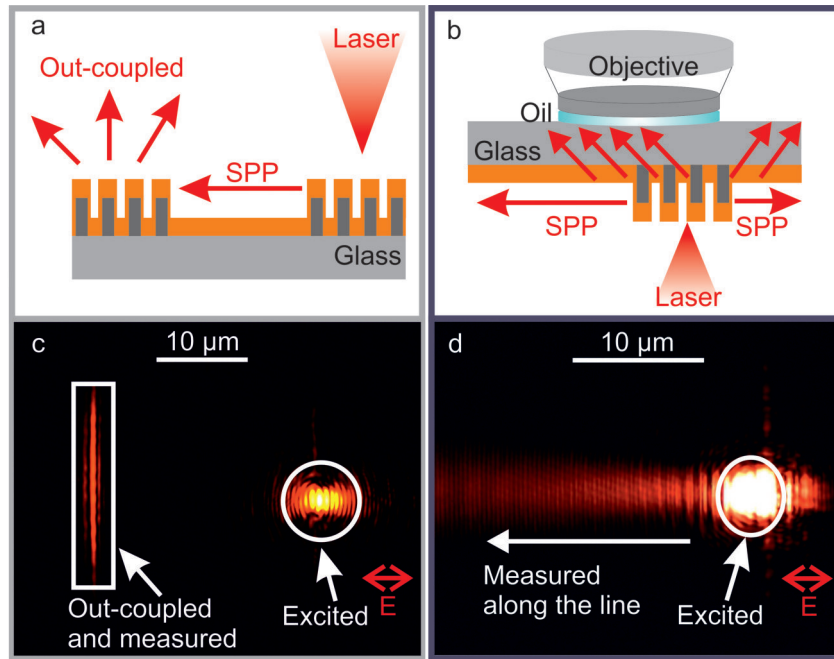
Fig. 5.4 Schematic illustration of Method 1 (a) and Method 2 (b) shows the comparison between two methods. The excited sample shown here in (c) with 633 nm using Method 1 and (d) with 800 nm using Method 2 is of 60 nm Ag^S. The plasmons are excited at 25 μm distance on the right grids and polarised horizontally towards left grids, from where they are captured. In Method 1, the out-coupled plasmons are captured by long distance 100X objective. In Method 2, 100X oil immersion objective is used. The excited and out-coupled points are indicated in (c) and (d) for both excitation sources.

The SPPs propagating on the metal surface and being out-coupled from the grids located at different distances are shown in Fig 5.5. As the distance increases, the out-coupled intensity seems to decrease. It is expected as SPPs are absorbed into the metal along the distance. Note that although the distance between exciting and out-coupled grids is 25 μm from centre to centre, the distance was measured in between the inner edges for the characterisation in Method 1.
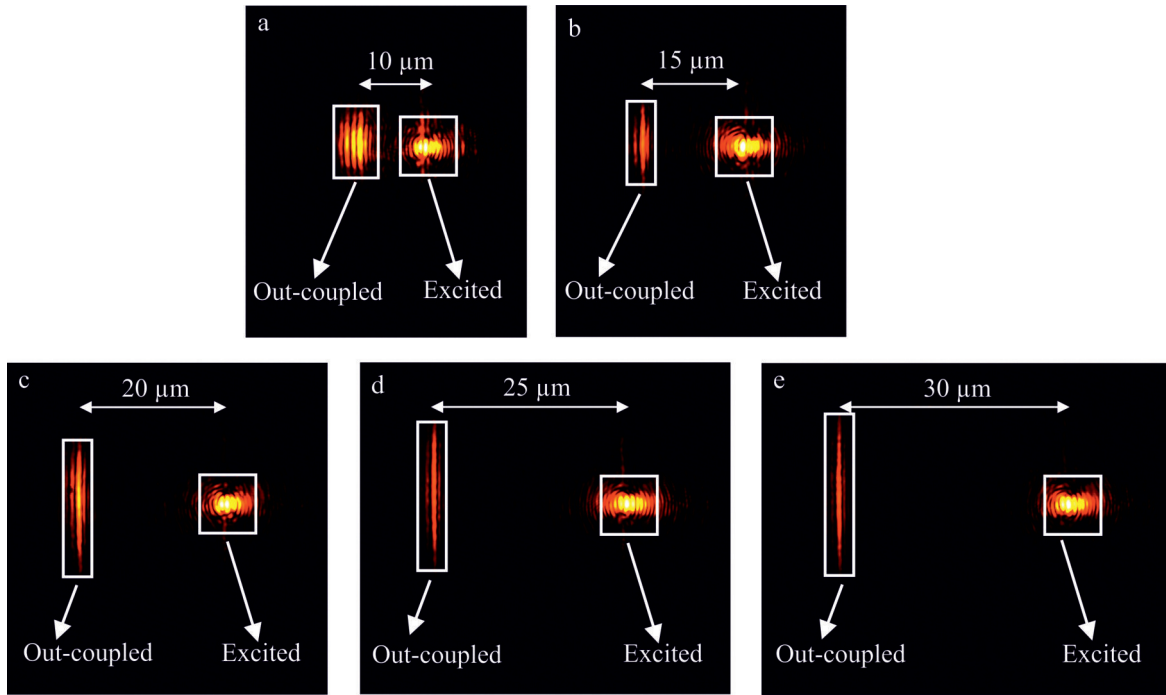
Fig. 5.5 Experimental images of the SPPs propagating along the distance and out-coupled from the grids located at different distances. The chosen sample is of 60 nm thick sputtered silver.

The intensities measured at each respective distances were plotted in the graph as shown in Fig. 5.6 (a) for Method 1 on 18 nm Ag^S and (b) for Method 2 on 50 nm Ag^E. As observed in Fig. 5.6 (a), Method 1 consists of plotted intensities with their corresponding distances. From a trendline, two points were chosen as initial intensity (I_0) and final intensity (I_1). Their specific distances were chosen as initial and final distances as x_0 and x_1. With these values, the L_{SPP} were calculated for each samples, using equation 4.2. For Method 2, least square method [164] was adopted to estimate L_{SPP} from decayed intensities along the distances. As shown in Fig. 5.6 (b), a trendline was plotted using least square method, and similar to Method 1, I_0, I_1, x_0 and x_1 were acquired to calculated L_{SPP}.
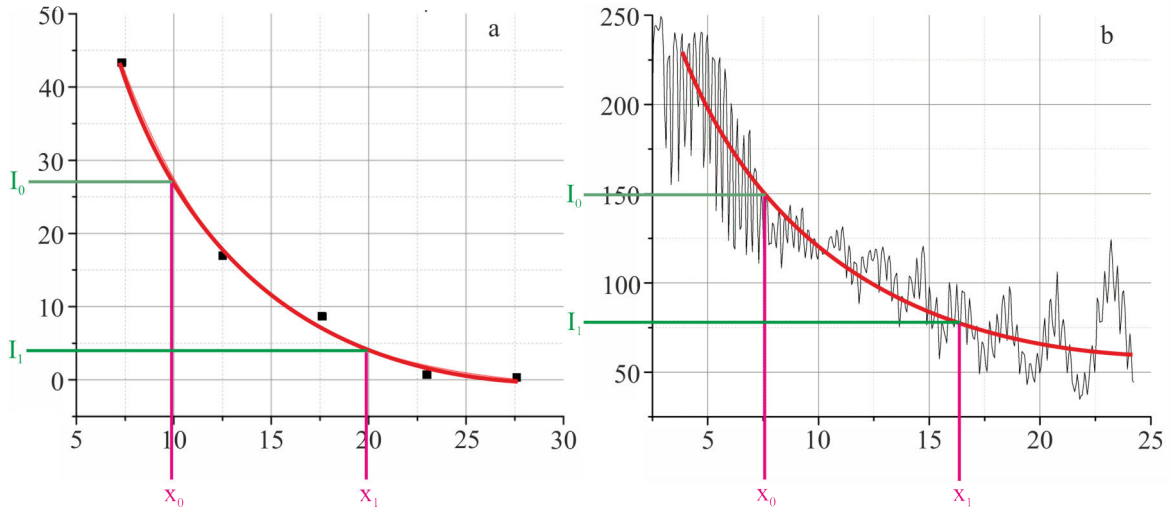
Fig. 5.6 The example calculation of L_{SPP} on 18 nm Ag^S, using Method 1 (a) and 50 nm Ag^E, using Method 2 (b).

5.3 Discussion

5.3.1 Influence of fabrication method

Gold

Table 5.1 The study of the influence of different measurement methods on gold, prepared by different deposition approaches; evaporation and sputtering.

Gold			
Deposition Method	Thickness	L_{SPP}- Method 1	L_{SPP}- Method 2
Evaporation	50 nm $\pm 1nm$	5.64 $\pm 1\mu m$	7.09 $\pm 1\mu m$
Sputtering	50 nm $\pm 1nm$	6.49$\pm 1\mu m$	6.94$\pm 1\mu m$

Results of the L_{SPP}, measured for evaporated and sputtered gold is shown in Table 5.1. In comparison, both deposition approaches provide similar L_{SPP} within an error range for both measurement methods. As mentioned in the paper [59], when the thickness of the gold is more than 10 nm, the sputtered gold produces pointed clusters, whereas the evaporated gold produces round cluster. The pointed cluster can have higher influences on scattering plasmons in comparison to the round cluster. This could be a well-founded explanation to why Au^S showed slightly higher L_{SPP} with Method 1 but Au^E indicated slightly better with Method 2. The LRM (Method 2) is more susceptible to morphology of the metals due to two interface (air/metal and metal/glass). This is expected to be better with evaporation process.

Silver

Table 5.2 The study of the influence of different measurement methods on silver, prepared by different deposition approaches; evaporation and sputtering.

Silver			
Deposition Method	Thickness	L_{SPP}- Method 1	L_{SPP}- Method 2
Evaporation	50 nm $\pm 1nm$	$12.66 \pm 1\mu m$	$13.33 \pm 1\mu m$
Sputtering	50 nm $\pm 1nm$	$13.81 \pm 1\mu m$	$11.90 \pm 1\mu m$

The silver films, shown in Table 5.2 behaved similar to the gold films. Due to the fact that silver films are sensitive to oxidation [165–167], their crystal size and the morphology has higher influence on L_{SPP} in comparison to the gold. In the case of sputtering, since it is possible to have the combination of both polycrystalline and amorphous crystals [168], the scattering losses could be higher than the evaporation that contains only polycrystalline crystals. Nevertheless, both Table 5.1 and Table 5.2 suggest that the influence of deposition methods on L_{SPP} is modest for $\approx$50 nm thick metals.

5.3.2   Influence of film thickness

In the case of a thick metal film on dielectric substrate, two independent SPPs modes exist related to different dielectric constants of the media adjacent to metal interfaces. If the metal is thin enough so that the electromagnetic interaction between the interfaces cannot be neglected, SPPs dispersion is significantly modified and coupling between SPPs modes on different interfaces of the film must be considered [9].

For the reason the LRM works best at an optimum thickness of $\approx$50 nm[169], further experiments were continued with Method 1 only. Different thicknesses of the metals were prepared and the influence of the deposition methods in variable thicknesses was investigated. Again, He-Ne (633 nm) was opted for the SPPs excitation. As shown in Fig. 5.7(a,b), L_{SPP} of thin metals coincide with both fabrication methods though some irregularities were seen below the thickness of 30 nm due to metal impurity. Silver is however expected to have longer L_{SPP} than gold due to its lower absorption impact. As the thickness of the metal increases, Au^S (brown) is observed superior in comparison to Au^E in gold films but reversed is noticed in silver films.

The experimental values achieved here closely agrees with the theoretical calculations based on bulk metals, estimated using dielectric constants from [51] and [52] on gold films, and from [51] only on silver films. The calculations as shown by dotted lines in each graph in Fig. 5.7 suggests the L_{SPP} of bulk gold to be $\approx$7 µm and $\approx$11 µm with regards to [51] and [52]

respectively. The L_{SPP} of silver is calculated to be ≈ 22 µm. The corresponding graph from sputtered gold suggested the L_{SPP} of ≈ 7 µm and ≈ 11 µm, representing the bulk property is achieved after 40 nm ± 1 nm and 75 nm ± 1 nm of film thickness, whereas evaporated silver endured up to thicker value of 60 nm ± 1 nm. Increasing the metal thickness results in large-grained films, bridging the gap between the properties of thin and thick films [51]. The deviation on trend-line suggests the possible impurity of metal during deposition process. Also, since the evaluation was done on different grids for different thickness, coupling efficiencies of the grids also creates influence on SPPs measurement.
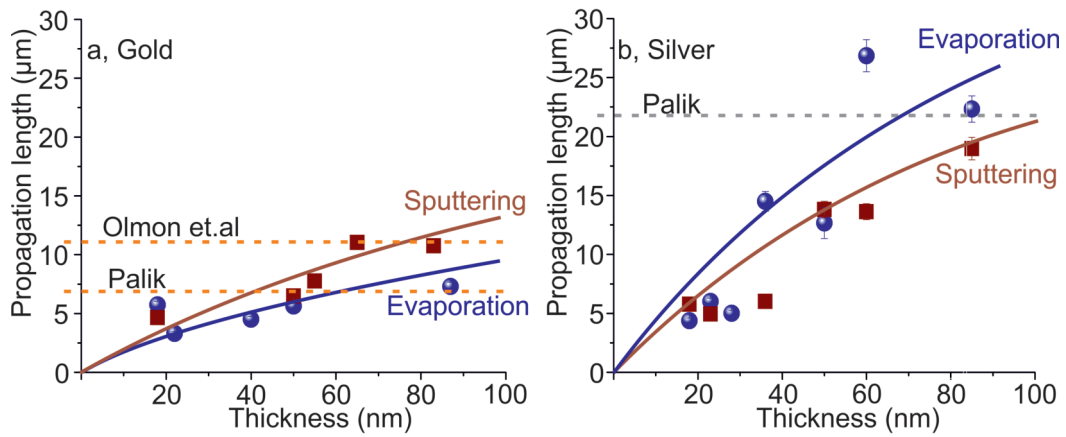
Fig. 5.7 The L_{SPP} length of (a)Au^E(blue dots), Au^S(brown square) and (b) Ag^E(blue dots), Ag^S(brown square). These experiments are based on grating-coupling (Method 1), excited by 633 nm. The comparison between gold and silver shows higher L_{SPP} for silver. In comparison between different deposition methods on gold, the Ag^S film shows longer L_{SPP} along the trendline. On silver, the inverse result is noticed. The evaporation method demonstrates longer L_{SPP} in comparison to sputtering. The dotted lines in each graph represents the theoretical L_{SPP} based on bulk metals. Using the dielectric constants from [51], the experimental value suggests that after 40 nm ± 1 nm of thickness, the sputtered gold show bulk properties but the evaporated silver remained up to 60 nm ± 1 nm. Based on another dielectric constants taken from [52], the bulk thickness is slightly higher, ≈ 75 nm. The L_{SPP} calculated with respect to the data from [51] and [52] on bulk gold are ≈ 7 µm and ≈ 11 µm respectively. On silver, only data from [51] is used and it is approximated to be around ≈ 22 µm.

Next, the resistivity calculated based on the formula given in [170], described by equation 5.8:

$$\rho_0' = \frac{c\rho_0}{k^1[1 - lnk^1]^1} \tag{5.8}$$

where, $k^1 = (d-r)/2d_{bulk}$. Here, r is the reducing factor (5.50 for gold) due to metal impurity and fabrication technique, d is the thickness of the metal, and d_{bulk} is the bulk thickness, c is constant, which is 3.07 for gold. In the equation, ρ_0 is the resistivity of the metal and ρ'_0 is the resistivity considering film impurity and inhomogeneity [170]. From Fig. 5.7, it was observed that bulk gold is achieved at the thickness of $\approx$60 nm, using evaporation technique. Taking the above values, the resistivity was plotted as shown in Fig. 5.8. It shows that the resistivity has an enormous impact for this thickness lower than 20 nm. Afterwards, it remains constants. These values overlaps well with the theoretical and experimental values given in the literature [170]. For the silver, no resistivity values were observed below 100 nm from [170]. This indeed proves that resistivity does not contribute significantly in SPPs L_{SPP}.
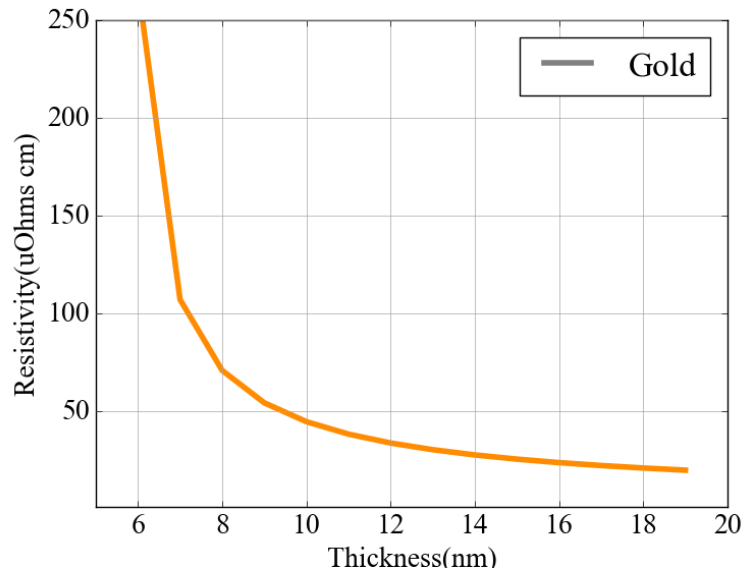
Fig. 5.8 Resistivity as a function of gold thickness

5.3.3   Study of surface plasmon polaritons on gold flakes

The preparation of the Au^F is explained in Fig. 4.2.2. The chemical reaction of this process is given by equation 5.9:

$$HAuCl_4 + OH(CH_2)_2OH \xrightarrow{\text{Heat}} AuCl_4^- \qquad (5.9)$$
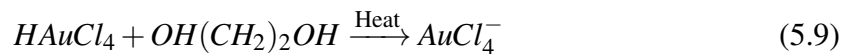
A possible mechanism for the formation of triangular and hexagonal shaped Au^F, as adopted from [171] is shown in Fig. 5.9. Once the chloroauric acid ($HAuCl_4$)is mixed with ethylene glycol (EG, $OH(CH_2)_2OH$) and heated at high temperature, gold atoms were produced. EG acts as a reducing agent and at high temperature, its reducing power increases more. At

this point, some Au atoms are formed with some unreacted $AuCl_4^-$. Next, an aniline was added as a catalyst to influence further reduction of unreacted $AuCl_4^-$. While the reduction of $AuCl_4^-$ to Au atoms occurs, the oxidation of aniline takes place. The Au atoms are favourably attached to the nucleus to form larger particles. The amount of triangular and hexagonal flakes cannot be determined. However, it is expected that the triangular flakes are formed by adding more Au atoms to the hexagonal flakes, as shown in Fig. 5.9(a). Alternatively, large triangular flakes are thought to be the result of accumulation of many small ones as shown in Fig. 5.9(b). Aniline is expected to play significant role as larger amount of it will end up in accumulation of oxidised aniline on the surfaces of the particles [152], resulting in spherical shape. The stirring speed controls the size of the flakes. Stirring the solution in mild speed will increase the size of the flakes [152]. The thickness of the Au^F varies from flake to flake but remains constant within one flake. These Au^F have variable thicknesses (20-90 nm).
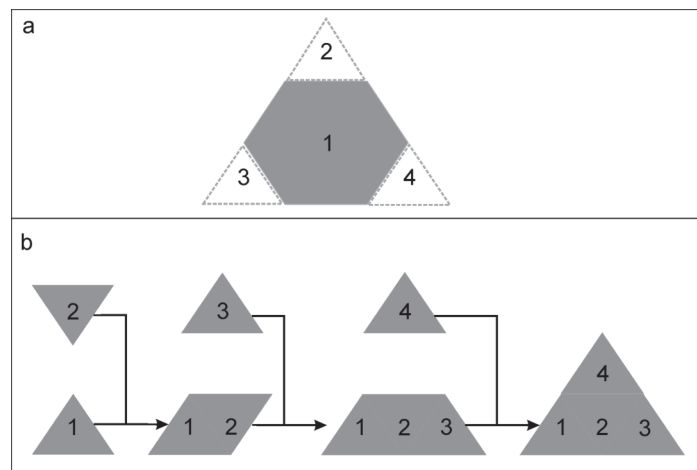
Fig. 5.9 The possible mechanism of the formation of Au^F

Initially, an attempt was made to transfer synthesised Au^F from the tube into the glass substrate. The clear observation with this method was, the flakes were not big enough. As demonstrated in Fig. 5.10, the flakes prepared with this methods were ≈5-10 μm big. An inadequacy in bigger size flakes creates the disadvantage in continuing intended experiment on these flakes. Since the plan was to measure the intensity of SPPs at different distances, these flakes were not big enough to authorise all the grids.
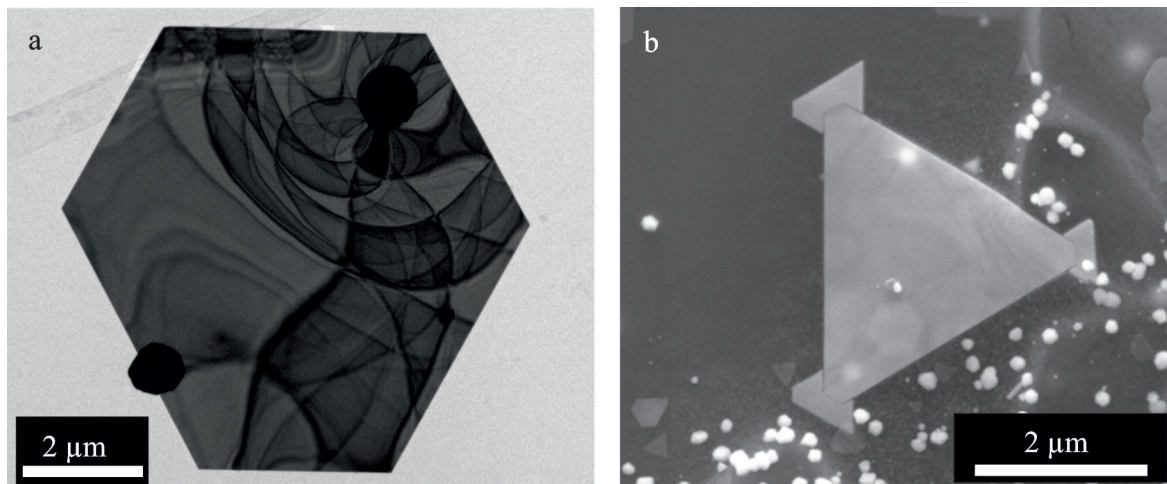
Fig. 5.10 (a) TEM image and (b) SEM image of small flakes in hexagonal and triangular shapes.
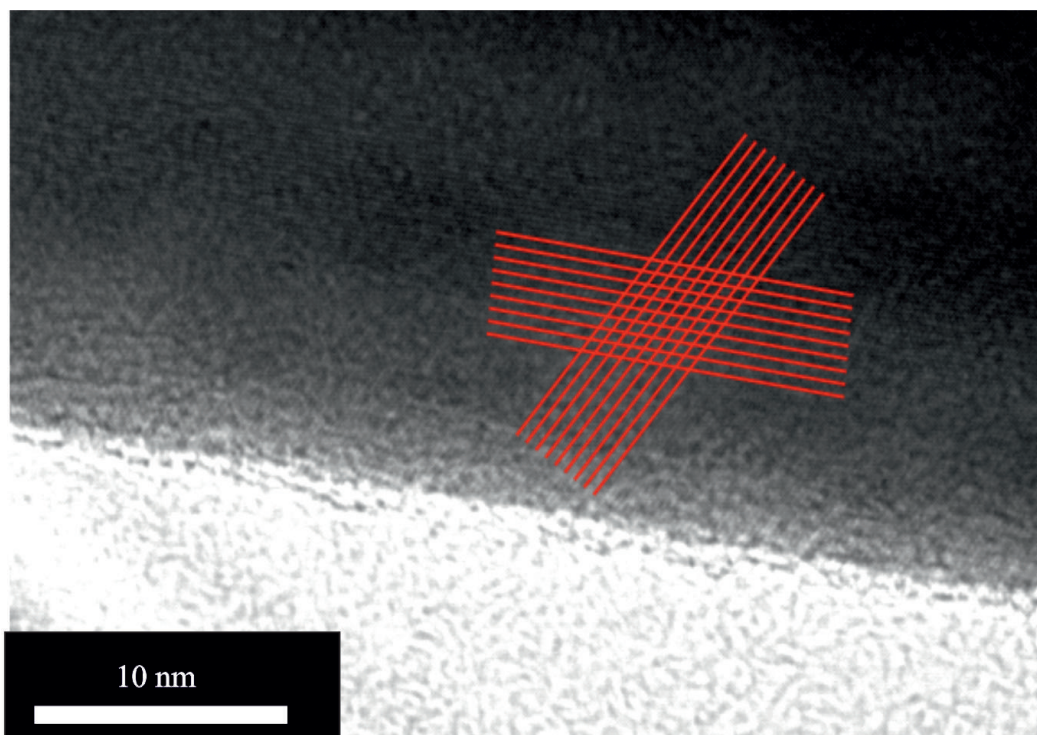
Fig. 5.11 The TEM investigation of Au^F suggests the arrangement of the atoms (highlighted by red lines), showing the property of single-crystallinity.

Another method, to synthesis Au^F on the substrate itself (*Section 4.2.2*), created larger flakes as shown in Fig. 4.10. These flakes were $\approx$ 40 μm large. Afterwards, TEM measurement was carried out to understand the atomic arrangement of the Au^F and confirm their

crystallinity. As shown in Fig. 5.11, the arrangement of the atoms were undistorted and symmetrically aligned, featuring the properties of single-crystallinity. For the better visibility, the atomic lines are highlighted by red lines.
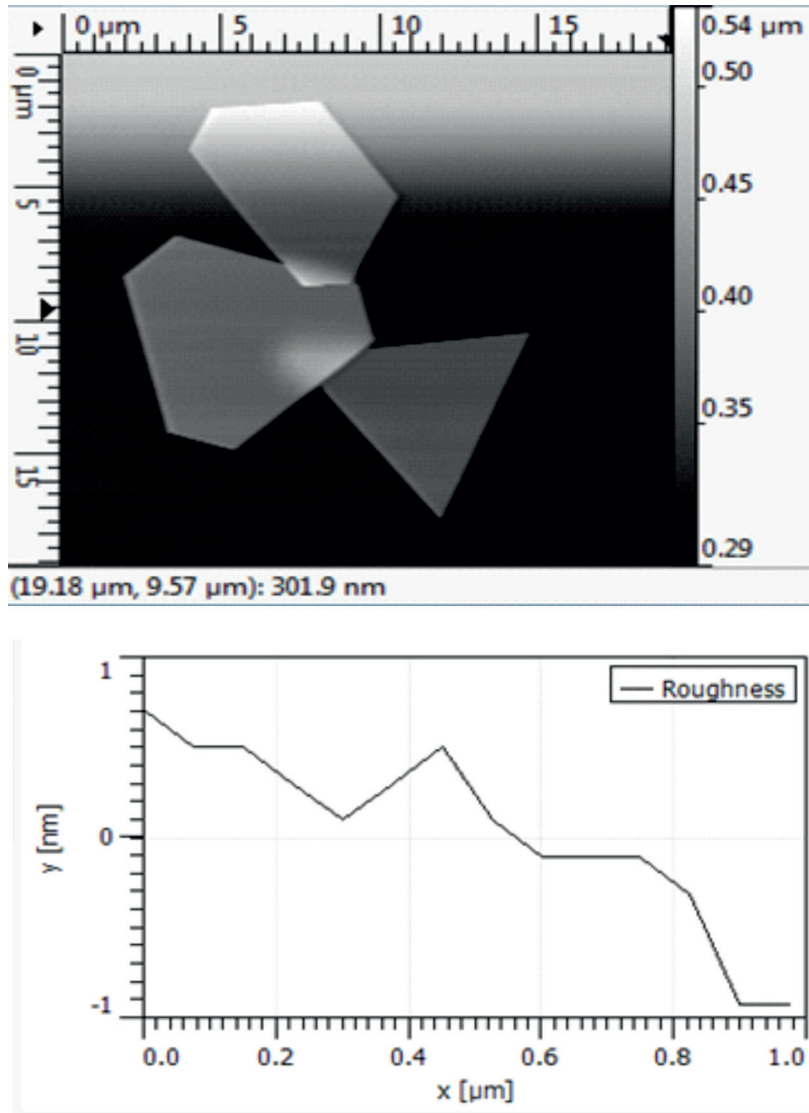
Fig. 5.12 AFM measurement of atomically flat gold flakes shows the surface roughness to be less than 1 nm.

For further confirmation, AFM measurement was carried out on Au^F. This measurement was carried out in tapping mode, and the data was analysed, using the software gwyddion. As shown in Fig. 5.12, the average roughness were measured to be less than 1 nm. According to [172], if the surface roughness is <1nm, it represents single- crystallinity. In Fig. 5.12, the top figure represents the chosen flakes and the average area for the measurement. The figure below represents the roughness as a result of measurement.

To pursuit similar roughness measurement on Au^E and Au^S, comparable experiment was carried out. However, due to large roughness, the tapping mode destroyed the tip of cantilever frequently. This barricaded the continuation of this measurement. For the reference, the measured roughness of four different samples (two for Au^E and two for Au^S) are listed in Table. 5.3. The result indicates that the roughness in quite high in reference to Au^F. In comparison between two different deposition methods, Au^E has higher roughness. This supports the L_{SPP} measurement in Fig. 5.7, which demonstrated that plasmons on Au^S propagated longer in comparison to Au^E.

Table 5.3 Roughness for polycrystalline gold.

Thickness	Roughness of Au^E	Thickness	Roughness of Au^S
40 nm	2.37 nm	50 nm	1.17 nm
85 nm	5.46 nm	65 nm	1.82 nm
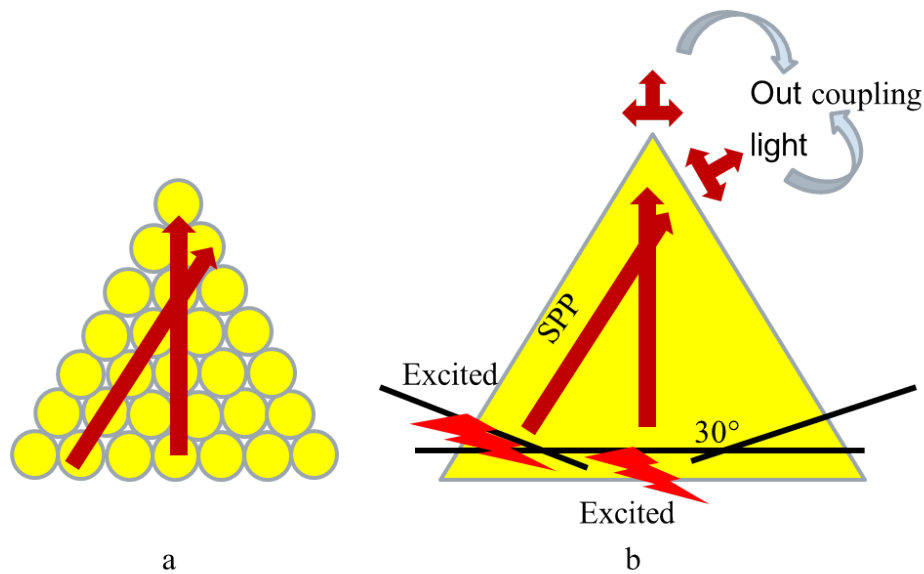
Fig. 5.13 The initial experimental plan showing investigation on out-coupled intensity based on the orientation. (a) Schematic diagram of the continuously aligned atoms, (b) Synthesised line at 30°and 180°for SPPs excitation.

The initial experimental plan for Au^F was to investigate whether the out-coupling light from the edge depends on the excitation direction on the flakes as shown in Fig. 5.13. To observe this hypothesis, single lines were synthesised on the flakes with photolithography (*Section 4.1.1*) at 180°and 30°. Considering the continuously aligned atoms on Au^F as shown in Fig. 5.11, the idea was to observe the effect of orientation on out-coupled intensity.

Despite, the impeccable grids were not achievable due to following reasons;

- The chosen photoresist for obtaining the grids were not strongly adhesive to the gold surface.

- Since the photolithography technique needs lots of trial and errors to get proper exposure time, the thickness of Au^F needed to be consistent for both testing and actual synthesis. However, it was not possible in this case due to the fact that their thickness was not controllable.

- Different Au^F consisted of different thickness and since these flakes are quite small, they were difficult to position and maneuver under the exact position of exposure.

- The developer of the photoresist, iso-propanol affected Au^F because after development, big flakes were disappeared.

- The trial and error option was limited since the preparation of the Au^F was time consuming process and every synthesis only produced few usable Au^F.

- To address the above problem, oil immersion objective was tested, which created additional problem of gold transparency. Since gold absorbs most of the light most of the light, only small amount of light was pass through to photoresist.

- Since refractive index of gold is lower than glass at the wavelength of 365 nm, most of the light were reflected from the glass/gold interface, limiting the amount of light reaching the resist.

Fig. 5.14 shows an attempt to synthesis grids on Au^F. Here, one can clearly observe that grids were not efficiently synthesised.
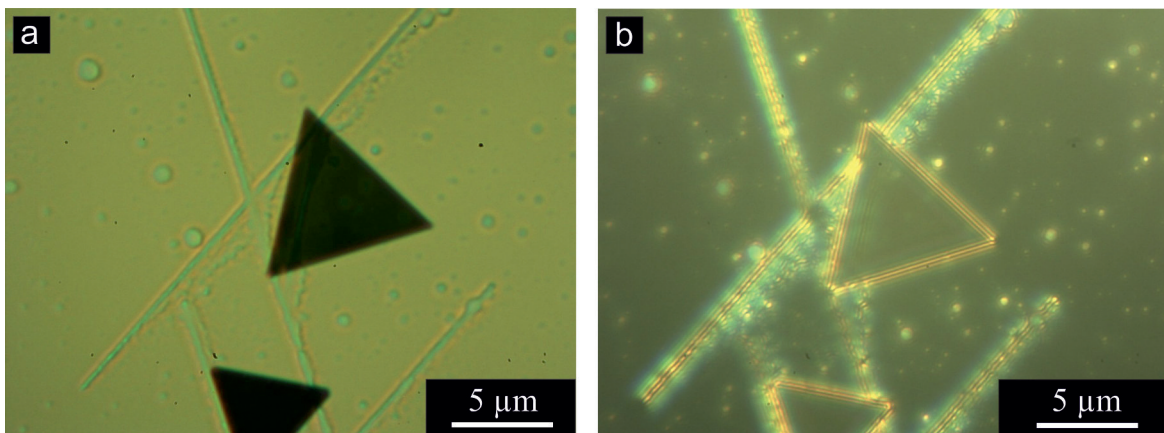
Fig. 5.14 The brightfield (a) and darkfield (b) view of photolithography structure on Au^F.

Nevertheless, the measurement was carried out in one of the flakes as shown in Fig. 5.15. As demonstrated, SPPs excitation was continued at 180°and 30°using mode-locked Ti:Sa with laser system listed in Table. 4.2 in Method 2. The figure clearly illustrates brighter out-coupled intensity with 180°orientation, considering both lines are ideally efficient.
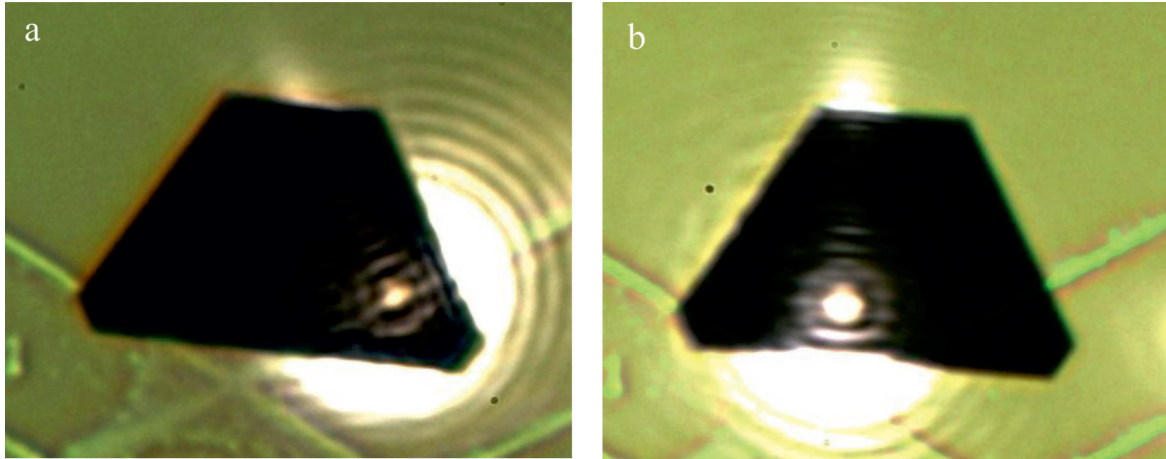
Fig. 5.15 SPPs excitation on the orientation of (a) 30°and (b) 180°.

However, due to the fact that the efficiency of SPPs depends on the grids, this experiment was continued further by replacing photolithography with focused ion beam method, and synthesising grooves instead of grids. On the synthesised Au^F (*Section 4.2.2*), the grooves,
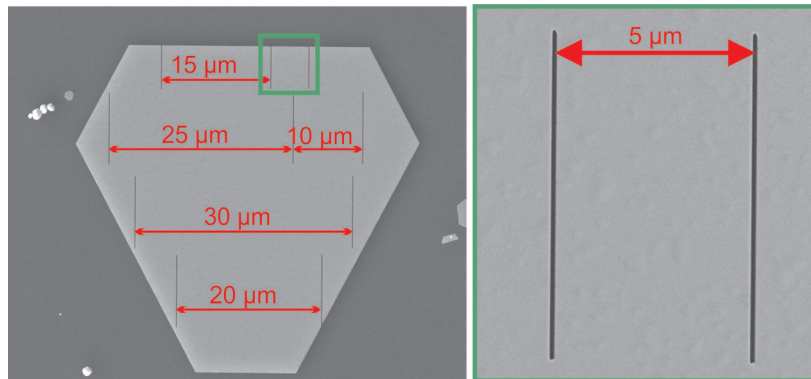
Fig. 5.16 FIB grooves on Au^F shown at different distances. The grooves are ≈130 nm wide and 1 μm deep.

as shown in Fig. 5.16 were milled onto the surfaces of the metal as subwavelength scattering grooves, at six different distances (labelled with red arrows) with a 30 kV focused ion beam from a liquid gallium source. Each groove has a width of about 130 nm and a depth of about 1 μm (milled into the Si-substrate).
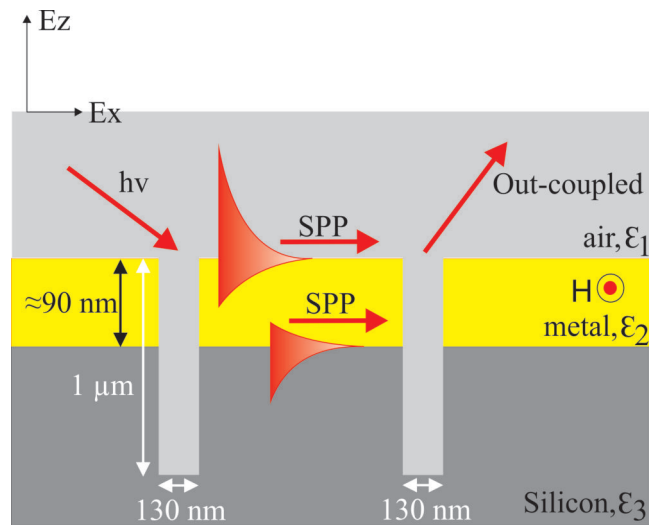
Fig. 5.17 Schematic diagram of three-level interface (air/metal/silicon) on AuF for SPPs study. The sample consists of two grooves prepared with FIB.
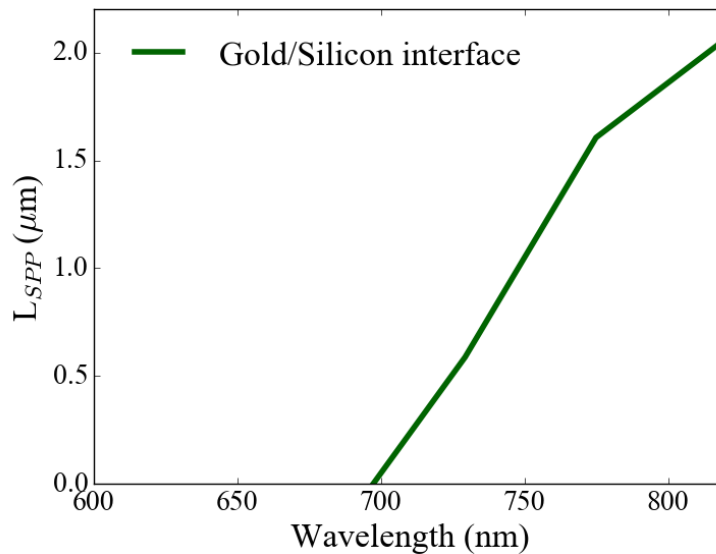
Fig. 5.18 Theoretical calculation of SPPs propagation length on the metal/silicon interface. The dielectric constants of gold and silicon (amorphous) are taken from [51].

When considering silicon as a substrate with flakes, synthesised on them, the grooves that were milled through to the silicon creates two interfaces for the SPPs propagation as shown in Fig. 5.17. The theoretical calculation of L_{SPP} on metal/silicon interface is shown in Fig. 5.18, which matches with the calculation from [173]. The dielectric constants of gold and silicon (amorphous) are taken from [51]. According to [173], the SPPs propagation on a

Si/metal interface exists only at higher wavelength but still is much shorter than on air/metal interface for the respective frequency. This is due to the fact that the high refractive index of silicon results in pushing field into the metal, enhancing the Ohmic losses. Looking at the chosen excitation wavelength (633 nm), there exists no propagation of the SPPs at all.

The grooved Au^F were evaluated with Method 1 only. Since Au^F were grown on Si-substrate, the excited plasmons cannot be captured from the back as it should be in Method 2. The grooved flakes, investigated with Method 1 at 633 nm is shown in Fig. 5.19(a). The L_{SPP} is estimated to be ≈ 7 μm. The number of grooves/grids and their depth and width plays significant role in assisting excitation of the SPPs [174, 175]. Since the grooves are quite narrow, it is possible that stronger confinement of the energy is located at the bottom of the groove, instead of propagating towards preferred direction [176, 177]. As a result, less energy is transferred to SPPs contribution.

Afterwards, thin flakes, synthesised on glass were investigated using mode-locked Ti:Sa with laser system listed in Table (4.2) in Method 2. The flake was excited at the edge as shown in Fig. 5.19(b) and the L_{SPP} was calculated from exponential decay curve, measuring the intensities at different points as labelled with red arrows (1-5) in Fig. 5.19(b). This method estimated the L_{SPP} to be about 21 μm. The higher estimation of L_{SPP} with this method in comparison to 633 nm is achieved due to lower absorption in longer wavelength.
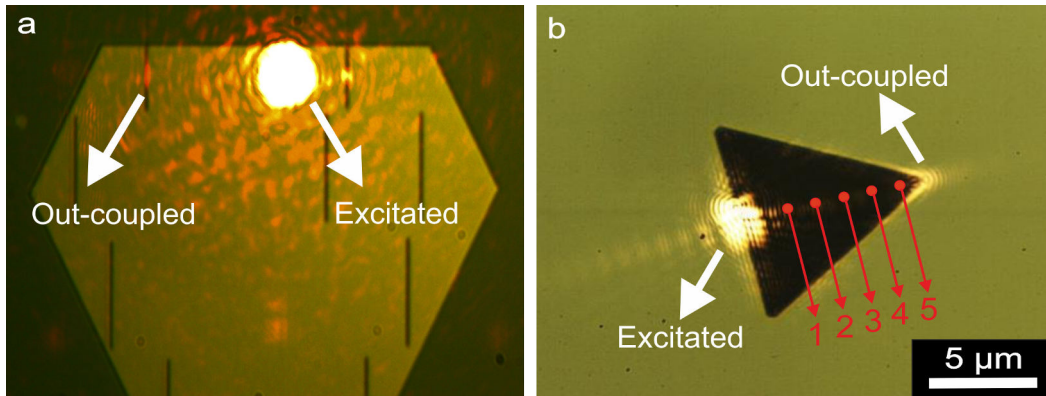
Fig. 5.19 An experimental pictures of Au^F excited by 633 nm (a) and 800 nm (b).

In Fig. 5.19, one can clearly observe the out-coupled light from edge of Au^F is brighter with 800 nm, approving longer L_{SPP}. It is due to the fact that at near-infrared, gold and silver have lower losses in comparison to lower wavelengths. The theoretical L_{SPP} with respect to [52] on single-crystalline gold is ≈ 9 μm at 633 nm and ≈ 55 μm at 800 nm. Note should be taken that these calculation are done on bulk gold. The Au^F, considered for 800 nm excitation was estimated to have a thickness of ≈ 20 nm ± 1 nm whereas ≈ 90 nm ± 1 nm thick Au^F was examined at 633 nm.

The experimental value of L_{SPP} at 633 nm closely matches with the theoretical value. However, there is a huge deviation between the experimental and theoretical values at the wavelength of 800 nm. This concludes that thickness influence is not that significant for shorter wavelengths in comparison to longer wavelengths. However, in the case of FIB milled Au^F, the efficiency of the excited plasmons are more attributed to the efficiency of the grooves.
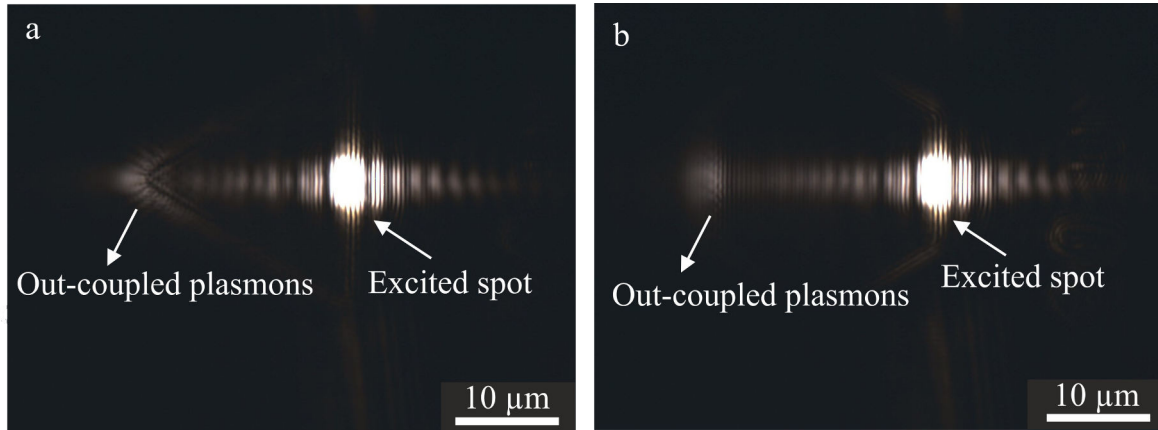
Fig. 5.20 SPPs excitation on (a) triangular and (b) hexagonal PAu^F using Method 2.

Additionally, Method 2, Ti:Sa 800 nm wavelength was chosen to evaluate PAu^F. Fig. 5.20 demonstrates the SPPs propagation on triangular (a) and hexagonal (b) flakes. The excited and out-coupled plasmons are labelled in the figure. These flakes are ≈20 nm thick. The triangular PAu^F is ≈20 μm large and hexagonal PAu^F is ≈25 μm large in size. The naked eye visualisation on Fig. 5.20 demonstrates triangular flake to have brighter out-coupled light in comparison to hexagonal flake. The could be due to the fact that hexagonal flake is slightly larger than triangular. The characterisation on these flakes were done similar to Au^F as shown in Fig. 5.19(b). The results were compared and listed in Table 5.4. From the table, one can visualise that Au^F acquire longer L_{SPP} in comparison to PAu^F despite possessing lower thickness. Both shapes of PAu^F demonstrated similar L_{SPP}; 12.62± 1 μm for triangular and 13.02± 1 μm for hexagonal, proving insignificant influence of shape on L_{SPP}.

Table 5.4 Propagation length on atomically flat crystalline gold and polycrystalline gold.

Orientation	Thickness	L_{SPP}- Method 2
Au^F	20 nm $\pm 1nm$	21 $\pm 1\mu m$
PAu^F triangular	50 nm $\pm 1nm$	12.62$\pm 1\mu m$
PAu^F hexagonal	50 nm $\pm 1nm$	13.02$\pm 1\mu m$

In summary, the comparison of L_{SPP} based on different fabrication approaches and metal thicknesses, measured by different experimental techniques were addressed. It has been shown that the dependence of L_{SPP} on different deposition methods is minimal. The thickness variation of the metals also showed similar L_{SPP} for thin metals films. However, thick gold films produced longer L_{SPP} with sputtering method whereas evaporation method was observed prominent for thick silver films. In comparison between both metals, silver films showed better propagation properties though their performance was limited by their sensitive surfaces. Additionally, grooves (130 nm x 1 μm) were milled into Au^F. The L_{SPP} on the flakes were evaluated with the incident light of 633 nm and 800 nm. The acquired values were compared with the experimental values of PAu^F, as well as the theoretical data, achieving good agreements. The section concludes that grating-coupling method is suitable for investigating thicker metals whereas LRM is more applicable for investigating thin metal films based on the leaked radiation. From this investigation, one can designate a proper condition and material, that provide longer L_{SPP}, which indeed is applicable as a strengthened sensor in optoelectronic techniques.

The acquired L_{SPP} in this thesis is still considered to be insufficient in large scale industrial applications. To compensate this, one can consider nanoparticles as a capacitor to assist energy to propagating electrons and enhance L_{SPP}. The propagation of SPPs can also influence the optical emission of semiconductor nanoparticles. Previously, it has been shown that the QDs coated on a silver/SiO_2 substrate generates directional and highly polarised fluorescence emission [178]. Therefore, the next chapter in this thesis discusses the properties of semiconductor nanoparticles as a prospective sensor materials.

Chapter 6

Optical properties of semiconductor nanoparticles

6.1 Room temperature amplified spontaneous emission in quantum confined systems

The optical properties of the semiconductor nanoparticles (NPs) depend on their size and morphology. To this regard, in this chapter, the optical amplification properties of quantum NPs of the cadmium selenide/cadmium sulphide (CdSe/CdS) material system with different dimensionality of spatial confinement are addressed. CdSe/CdS core/shell quantum dots (QDs), core/shell quantum rods (QRs) and 5 monolayer (ML) thick core/crown quantum wells (QWs) exhibiting 0-D, 1-D and 2-D spatial confinement dimensionality of the electronic system, respectively at room temperature are considered. Continuous films of all these NPs are synthesised and for optical pumping, the samples were illuminated by the second harmonic and the fundamental wave of a mode-locked amplified Ti:Sa laser in ω an 2ω systems, as well as the third harmonic of a nanosecond Nd:YAG laser with 14 Hz repetition rate. The specifications of both laser systems are shown in Table 4.5 and Table 4.3, respectively. The threshold values for each NPs with respect to each laser systems are compared. To emphasize this effect, ASE is demonstrated also in QRs and QWs at ambient temperature under nanosecond pumping (355 nm) in the same material films. These outcomes feature a scope of developing novel types of tunable lasers that are functional at room temperature.

A standard 18x18x0.15 mm^3 microscopic cover glasses were cleaned thoroughly by sonicating in acetone and then in deionised water for a minute. A total amount of 50 µL QDs, QRs and QWs, mixed in toluene were spin-coated on the glass slides separately at a speed of 10 rps for 10 seconds. The film quality of each NPs is shown in Fig. 6.1(a-c). The QRs and QWs show typical agglomeration behaviour in comparison to QDs. These films are about 150-195 nm thick as shown in Fig. 6.2(a-c). All NPs samples provide a high absorption cross section in the UV spectral range for efficient one-photon absorption pumping.
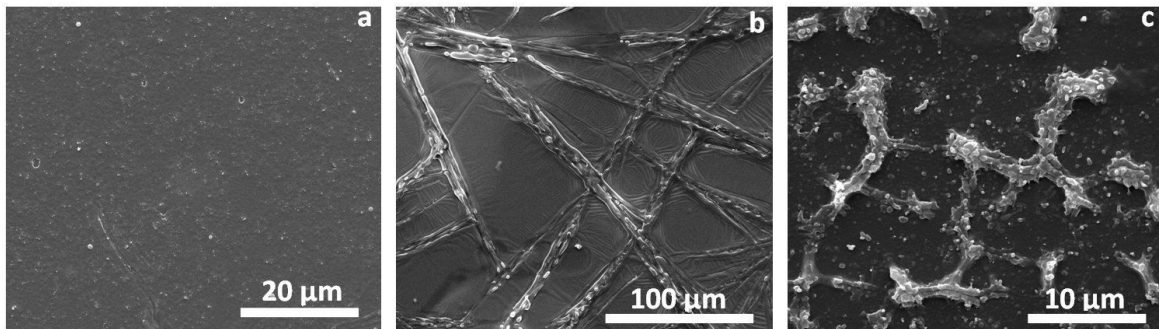
Fig. 6.1 SEM image of spin-coated film of core/shell QDs (a), core/shell QRs (b) and core/crown QWs (c).
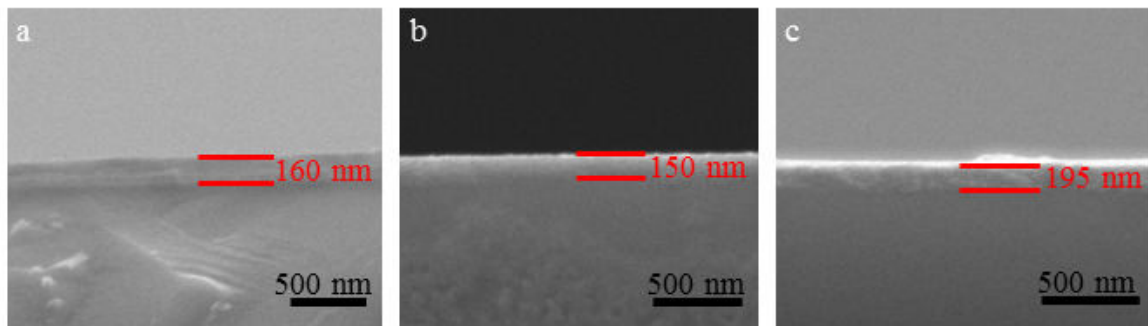
Fig. 6.2 SEM image of spin-coated film of core/shell QDs (a), core/shell QRs (b) and core/crown QWs (c) showing their film thickness. The films are about 150-195 nm thick.

The experimental method for this section was described in detail in *Section 4.1.4*. The laser was focused by the cylindrical lens (5 cm) and the middle of focal line was positioned onto an edge of the material samples, so that the optically pumped line extends into the material layer when the slit was opened. The emission is clearly visible with the naked eye, as shown in Fig. 6.3.
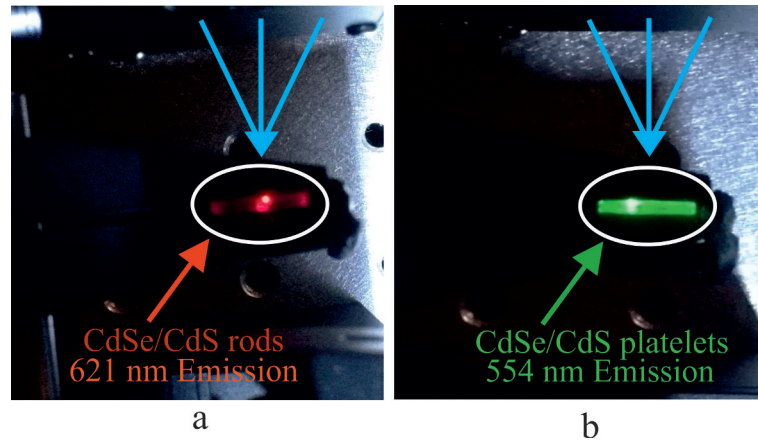
Fig. 6.3 Example of excitation of QRs (a) and QWs (b) shows the excited spots and emission at 621 nm and 554 nm, respectively.

Discussion

First experiments were performed using the second-harmonic output of the Ti:Sa laser at the wavelength of 400 nm, providing one-photon absorption pumping of the individual nanoparticle samples. Using the maximum interaction length of 1.5 mm, the pulse energy of the second-harmonic (2ω) output was increased until a definite evidence of a sharp and narrow peak was observed on top of the spectrally broad fluorescence emission. This spectral narrowing clearly indicates the onset of ASE [179].

Fig. 6.4 represents the ASE indication with 2ω pumping. The arrows in each graph, i.e. in Fig. 6.4(a) (QDs), Fig. 6.4(c) (QRs) and Fig. 6.4(e) (QWs) represent the energy range on the sample, considering the interaction length to be 1.5 mm. The NPs showed strong broadband fluorescence for low pump energy and clear evidence of ASE at higher pump energies at peak wavelengths of 632 nm (QDs), 623 nm (QRs) and 572 nm (QWs), respectively. ASE threshold energies and fluences were evaluated from Figs. 6.4(b,d,f). In this case, the threshold values for all three films QDs, QRs and QWs are as low as ≈ 0.285 μJ, ≈ 0.012 μJ and ≈ 0.009 μJ, respectively. Taking into account the length and the width of the illuminated area of the line focus on the sample this corresponds to pump fluences of ≈ 542 μJcm^{-2}, ≈ 25 μJcm^{-2} and ≈ 15.42 μJcm^{-2}, respectively. These values agree well with data given in previous literatures [180, 81]. However, the threshold value for QWs is lower than previously reported 5 monolayer thick CdSe, which is 28 μJcm^{-2} [105]. This suggests better material quality of the used QWs.
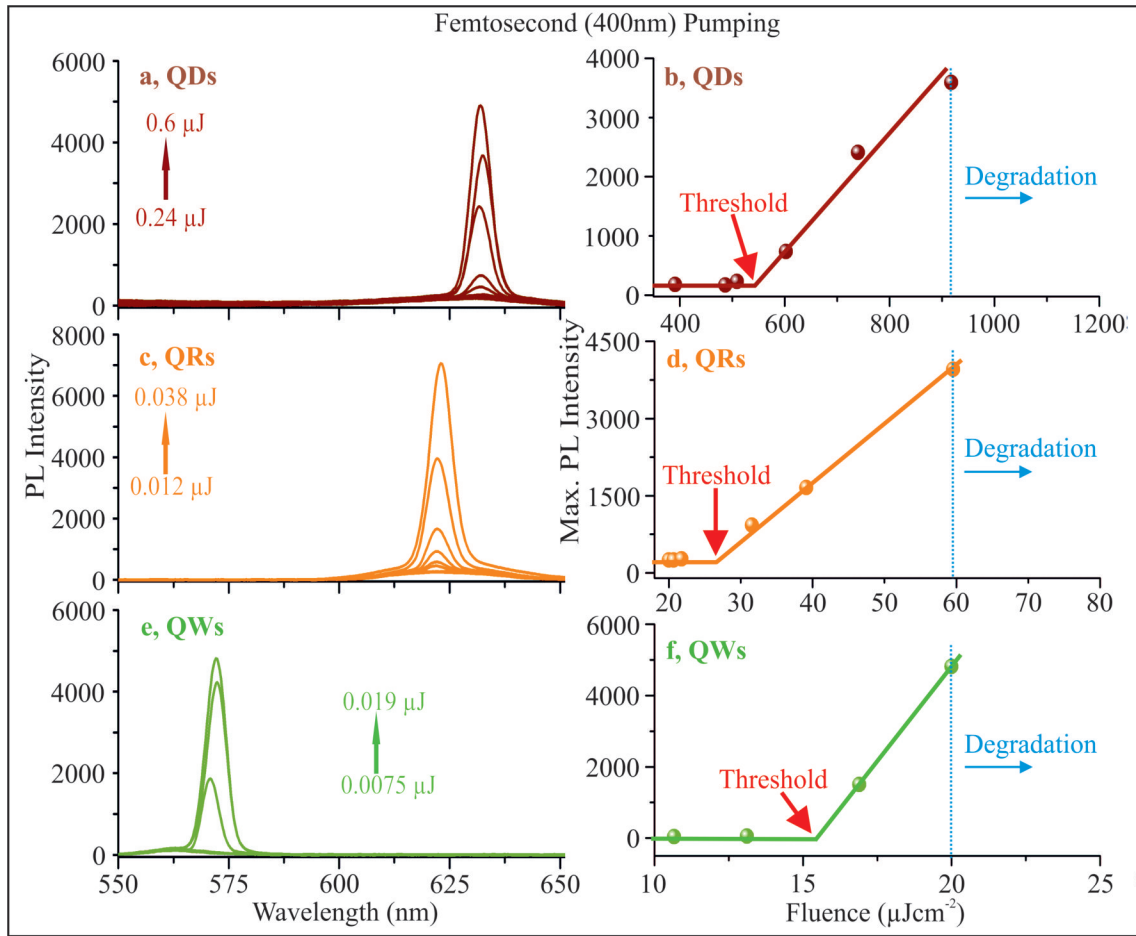
Fig. 6.4 The comparison between QDs (a,b), QRs (c,d) and QWs (e,f), measured with 2ω pumping. The arrows in graphs a,c and e (red for QDs, orange for QRs and green for QWs) represent the energy range used. All three NPs show clear indication of ASE at the peak wavelengths of 632 nm (QDs), 623 nm (QRs) and 572 nm (QWs). The corresponding ASE threshold values as shown in Fig. b(QDs), d(QRs) and f(QWs) are at the pump fluences of $\approx 542\ \mu Jcm^{-2}$, $\approx 25\ \mu Jcm^{-2}$ and $\approx 15.42\ \mu Jcm^{-2}$, respectively.

The particles of all dimensionality showed slight variation in the emission wavelength during pump power variation. However, this shift is within the resolution limit of the used spectrometer. Consequently, for the evaluation of the gain curves only the maximum emission peaks were taken. The results are given in Fig. 6.4(b,d,f). The QDs and the QWs show photo-degradation at higher pump fluences. For the QDs generally, the necessary pump fluence is one to two orders of magnitude higher than for QRs and QWs. In this case the photo-degradation can be attributed to the damage threshold of the material layer. For the QWs the absorbed energy is highest so that the damage threshold is drastically reduced.
Photo-degradation was observed for pump energies above $\approx 0.45\ \mu J$ (for QDs), $\approx 0.038\ \mu J$

(for QRs) and ≈ 0.0135 μJ (for QWs). These correspond to the fluences values of 918 μJcm^{-2}, 59 μJcm^{-2} and 20 μJcm^{-2}, respectively.
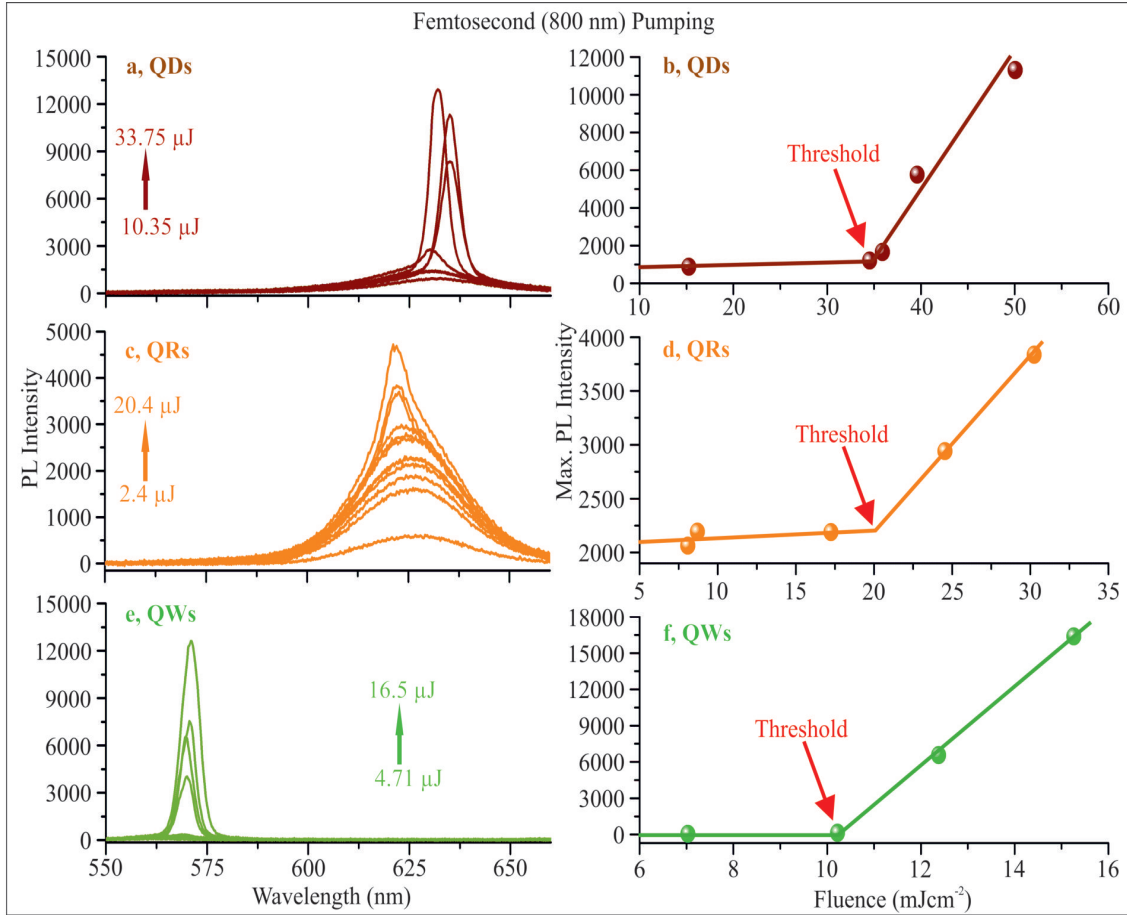
Fig. 6.5 Femtosecond fundamental (800 nm) pumping of different NPs. The energy variation with minimum and maximum in each NPs coated film is shown by arrow in each graph (a for QDs, c for QRs and e for QWs). The Fig. b, d and f represent the threshold values at the maximum peak intensity wavelength for each particle. The threshold values of QDs (b), QRs (d) and QWs (f) are at pump fluences of ≈ 35 mJcm^{-2}, ≈ 20 mJcm^{-2} and ≈ 10.5 mJcm^{-2}, respectively.

An additional study was carried out using femtosecond pumping at 800 nm. The result is shown in Fig. 6.5. Due to the two-photon absorption required for pumping, the threshold pump pulse energies are significantly higher than in the previous case. The energy range on the sample is again indicated by the arrows in each graph for the different NPs. The lowest pump energy represents the energy at which clearly fluorescence could be detected. The energies were then increased until the films were destroyed. The ASE threshold energy again was taken when clear onset of the narrow ASE peak occurred. Considering the interaction

length of 1.5 mm, the threshold values of QDs, QRs and QWs to be $\approx$22.5 µJ, $\approx$11.04 µJ and $\approx$6.75 µJ, respectively as shown in Figs. 6.5(b,d,f). This corresponds to threshold pump fluences of $\approx$35 mJcm^{-2}, $\approx$20 mJcm^{-2} and $\approx$10.5 mJcm^{-2}, respectively. These values are in line with data given in the literature [181].

The above experiments, using femtosecond one-photon pumping at the second harmonic (2ω) and two-photon pumping at fundamental (ω) wavelengths of the Ti:Sa laser, served for referencing the spectral measurements with common results from literature and to demonstrate that clear signals of ASE were obtained from all types of NPs under investigation. In case of femtosecond pumping only energy/fluence variation measurements were carried out at room temperature. The main goal of this section, however, was the demonstration of ASE signals from the different NPs, using nanosecond pumping at room temperature, and the demonstration of high intrinsic gain in QR and QWs material films due to their enhanced absorption properties as explained above.
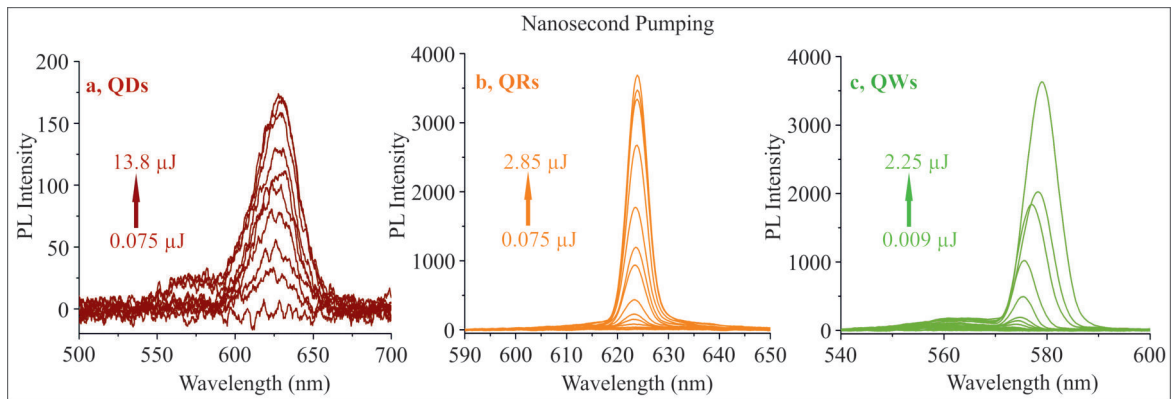
Fig. 6.6 The comparison between nanosecond pumping of (a)QDs, (b)QRs and (c)QWs. The arrows in each graph (red for QDs, orange for QRs and green for QWs) represents the energy range, adopted for each case. The QRs and QWs show clear indication of ASE at the peak wavelengths of 624 nm and 579 nm, respectively but only fluorescence is detected from QDs at the peak wavelength of 628 nm.

Under nanosecond pumping, all three spin-coated NPs films were illuminated up to the damage threshold of the samples, as shown in Figs. 6.6(a-c), but only the spectra of QRs and QWs exhibit clear indications of ASE. Note the different wavelength scales in Fig. 6.6. The QDs only show a sign of fluorescence. The ASE threshold value as shown in 6.7(a-b) are $\approx$1.3 mJcm^{-2} and $\approx$1.54 mJcm^{-2} for QRs and QWs respectively. Damage threshold of the sample was observed at the fluence value of $\approx$4 mJcm^{-2} for both QRs and QWs. Since, the spherical QDs with small diameter have a larger energy band gap in comparison to bigger ones, this requires higher excitation energy for the excitons, increasing the timescale for the normal emission process. During this process, AR process can occur, disturbing the

electron-hole relaxation mechanism. This effect is not observed in QRs and QWs due to the fact that their 1-D and 2-D degrees of freedom let the emission process occur faster than AR. In contrast to femtosecond pumping, the ASE thresholds here appear to be very similar, despite the difference in size of the extended shell structures. It is assumed that due to the larger size of the QWs, the pumping process is more efficient since the shell structure acts as an optical antennae for the pump radiation. This effect is corroborated by the experimental results of femtosecond pumping. However, for nanosecond pumping, the situation is different with respect to the pumping wavelength and of course the pulse duration. First, the absorption cross sections for QRs and QWs may differ slightly which may result in different pump efficiencies. Second, which is more decisive, the materials significantly accumulate heat during the nanosecond pulse duration of the pump pulses. The heat cannot be transferred within this time duration to the substrate. Due to their extended shell structure, the heating process is more pronounced for the QWs than for the QRs [182]. This effect is visible in the experimental results by an increase of the ASE threshold of the QWs. As a result, the ASE threshold of QRs and QWs appear to be in the same order of magnitude, in contrast to the results of femtosecond pumping.
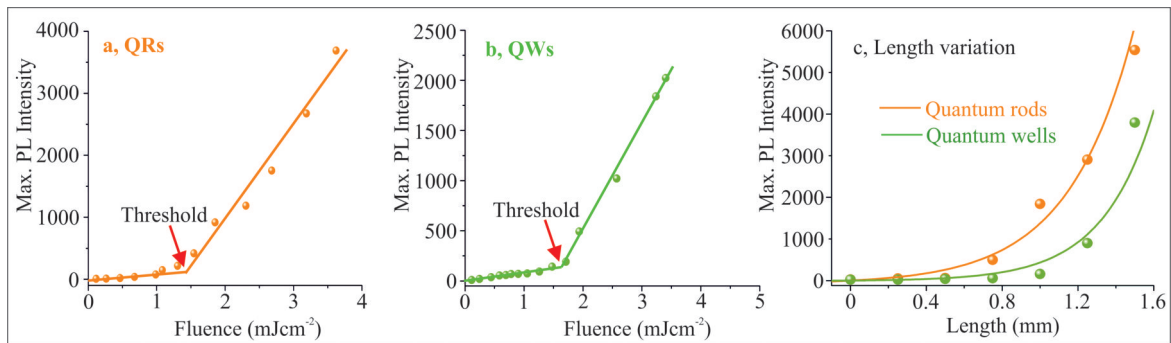
Fig. 6.7 The QRs and QWs show ASE thresholds at ≈ 1.3 mJcm^{-2} (a) and ≈ 1.54 mJcm^{-2} (b), respectively. Fig. (c) represents the slit variation performance of QRs and QWs corresponding to the pump pulse energy at the sample to be ≈ 2.25 μJ, with an interaction length of 1.5 mm. The QRs needs ≈ 0.5 mm opening of the slit for ASE confirmation whereas QWs needs ≈ 0.85 mm.

Due to the absence of ASE in QDs with nanosecond pumping, the variation of the interaction length, i.e. the length variation of the pumped zone, was carried out only for QRs and QWs. In this experiment the pump fluence was set to 3.3 mJcm^{-2} for both, QRs and QWs, in order to stay clearly below the damage thresholds of the samples. As demonstrated, both QRs (orange) and QWs (green) have no emission until 0.5 mm of slit opening. The gain

value was calculated by fitting the points in Fig. 6.7(c) and using the equation 6.1:

$$I = \frac{A}{g}(exp(gL) - 1) \tag{6.1}$$

where I is the intensity, g is the gain coefficient, L is the stripe length and A is the constant. The calculated gain values are 29 cm^{-1} and 37 cm^{-1} for QRs and QWs, respectively. These values are in the same order of magnitude of QD gain, measured under nanosecond pumping, but using a distributed Bragg reflector to benefit from enhanced modal gain [183].

In summary, light amplification properties of CdSe/CdS QDs (emission wavelength 620 nm), QRs (emission wavelength 621 nm) and QWs (emission wavelength 554 nm) at ambient temperature were investigated. The thin films (150 nm-190 nm) of all three NPs were spin-coated on glass substrates. Three pumping regimes were investigated: (i) femtosecond pumping using the second harmonic of a Ti:Si laser with 50 fs pulse duration at 400 nm, (ii) femtosecond pumping at the fundamental wavelength of the femtosecond laser at 800 nm, and (iii) nanosecond pumping by third harmonic of a q-switched Nd:YAG laser (355 nm) with 6 ns pulse duration. It was observed that ASE of all NPs can be achieved at room temperature for femtosecond one-photon and two-photon pumping. The emission threshold for each NPs sample was measured on the basis of pump fluence variations. In comparison, 2ω pumping produced the lowest threshold power for ASE in all three NPs, which agrees well with values given in the literature. For nanosecond pumping ASE at room temperature was observed from QRs and QWs due to their enhanced absorption properties. The length variation of the pumped zone on the sample in this case yielded gain coefficients of 29 cm^{-1} for QRs and 37 cm^{-1} for QWs. This investigation confirms that in comparison to three NPs (QDs, QRs and QWs), QWs has an ability to provide higher gain as well as lowest ASE threshold.

6.2   High temperature influence on amplified spontaneous emission of quantum wells

In addition to the size and morphology of NPs, an impact of surrounding environment on ASE is also regarded as a fascinating investigative specification. Considering the final stage of this thesis as to embed NPs into the polymer, and also considering the NPs as a possible high temperature sensor, the perception on how the ASE on NPs is influenced with regards to change in temperature needs to be evaluated. From our previous investigation, it was demonstrated that in comparison between three NPs (QDs, QRs and QWs), QWs have a lowest threshold energy for the ASE. Due to this reason, only QWs is carried on for the upcoming investigation. The influence of temperature on ASE of NPs have been investigated by many scientists [80, 119, 129] but a report on 5-monolayer QWs is not yet addressed. Similar to *Section 6.1*, the properties is evaluated on thin film, obtained by spin-coating QWs on the glass slide. The film is pumped under a nanosecond pumping, 3ω (355 nm) while being heated up to different temperatures. The fluorescence and ASE spectra were recorded at each respective temperature. The investigation also gives special consideration to the change in Full Width Half Maximum (FWHM) and red-shifted wavelengths with respect to altered temperature. Another significant evaluation in this section is an assessment of a stability of QWs while exciting at single spot. The change in peak intensity with respect to per degree Celsius is also evaluated. Upon the observation of significant temperature influence on these QWs, an approach can be adopted in real-life application as a temperature sensor.

The QWs particles with the Cd ion concentration of 35 mmol/L, dispersed in 3 mL toluene was ultasonicated for $\approx$5 minutes. Separately, a standard 18x18x0.15 mm^3 microscopic cover glass was cleaned thoroughly by sonicating in acetone for $\approx$5 minutes and then in deionised water for a minute. Afterwards, a total amount of 50 μL QWs solution was spin-coated at a speed of 10 rps for 10 seconds.

For an investigation purpose, an experimental technique, explained in *Section 4.1.4* with top-surface coupling was chosen. The experimental photo that demonstrates the excitation spot on the sample is shown in Fig. 6.8. A nanosecond (Table 4.4), 3ω (355 nm) with 4 ns pulse duration at a repetition rate of 14 Hz laser was pumped vertically from the top (shown by puple arrows) and was focused by the cylindrical lens (f=5cm) to the sample, placed on hot plate. The spot size was 10 mm long and 45 μm wide at the focus region. The emission wavelength is around 554 nm. The fibre, placed next to the sample horizontally, collected the emitted photons. Considering the damage threshold of the sample from previous section, the pump fluence was set to 3.3 mJcm^{-2}.
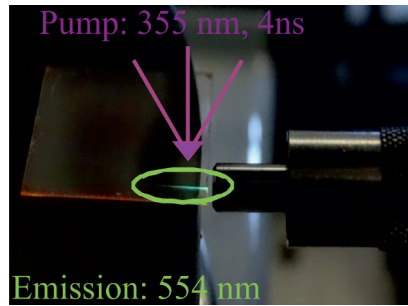
Fig. 6.8 Experimental photo demonstrating the excitation spot on sample. The sample is placed on the hot plate. The laser impacts through vertically (shown by purple arrows), hitting the horizontally arranged sample that emits around 554 nm. The fibre is placed next to the sample, collecting PL intensity.
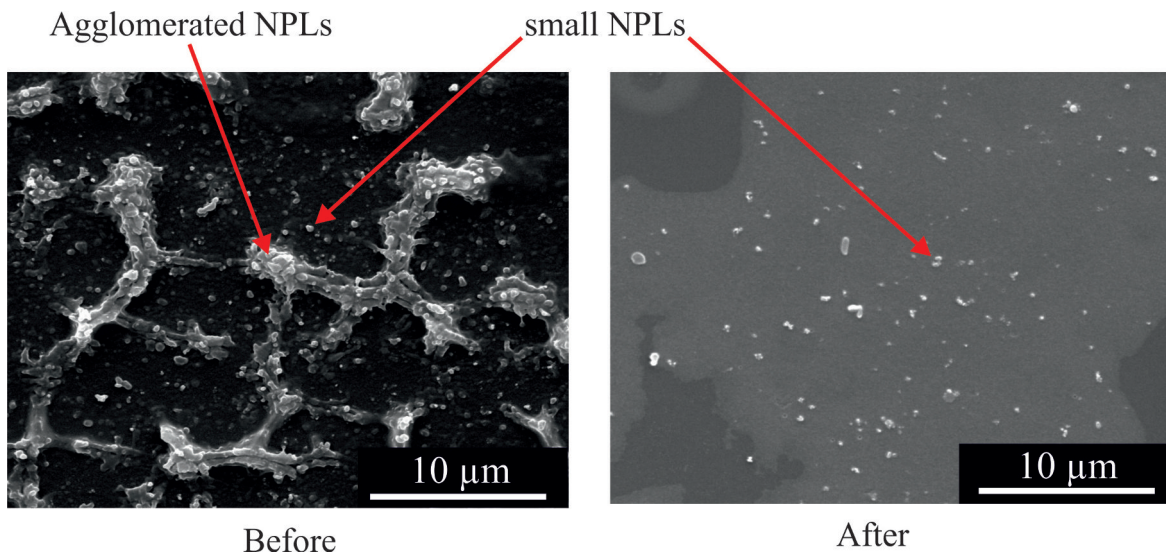
Fig. 6.9 The SEM picture of the QWs films before and after baked on a hot plate. The big agglomerated QWs are seen in normal room temperature with many small particles around. After the sample is baked up to 200°C, big agglomerated QWs have disappeared, leaving only small ones.

The first measurement of PL intensity was carried out at room temperature. Subsequently, measuring at 50°C, the temperature was increased up to 200°C while measuring at each 50°C. The film quality of QWs before and after they were baked is shown in Fig. 6.9. The investigated SEM picture showed big agglomerated QWs before they were baked and disappearance of those agglomerated QWs after baking at 200°C. The disappearance could be a sign of particles deterioration.

Normally, these QWs are synthesised at high temperature 240°C (see *Section 4.2.5*) under Ar atmosphere. When the temperature of the QWs is increased at normal atmosphere, it may

result in some interfacial strain [184] between core and crown. As a result, the concentration of the NPs seems to decrease. Since not many NPs can be excited at high temperatures, the rate of ASE is decreased as well.

Discussion

Influence of temperature increase on emission properties of NPs

In oder to investigate the influence of temperature on QWs, five different temperatures were chosen, starting at room temperature (25°C), followed by 50°C. Afterwards, the temperature was increased by 50°C until 200°C. The evaluation is listed in Fig. 6.10. The figure (a) demonstrates that as the temperature is increased, PL intensity that represents both ASE and fluorescence spectra decreased. This suggests that the ability of the sample film deteriorates at some degree once it is baked at higher temperatures. The fluorescence is observed until 200°C but the ASE only lasted until 150°C. Another observation is the red-shifting of the peak wavelengths. This observation with the FWHM of each temperature is shown in Fig.6.10(b). As expected, both peak wavelength and FWHM (blue square) increase with the temperature. The increase of the peak wavelength confirms the presence of red-shifting. This occurs due to the fact that the energy associated with radiative and non-radiative emission is less than that of absorption. At room temperature, the peak wavelength of $\approx$569.87 nm is observed. By the time the temperature is increased to 150°C, the peak wavelength was red-shifted by $\approx$19 nm (peak at 150°C $\approx$588.78 nm). The FWHM at 25°C is as low as $\approx$5.25 nm. The increase in temperature to 50°C, 100°C and 150°C also increases the FWHM to $\approx$6.12 nm, $\approx$6.8 nm and $\approx$9.2 nm respectively.

Theoretically, the bandgap of NPs should decrease as the temperature is increased [108] (*Section 2.2.5*). However, increase in temperature also accumulates additional heat waste in the system, which triggers AR process even faster than it would be at ambient temperature. Therefore, although decrease in bandgap is occurred, the faster AR process limits the exciton process.
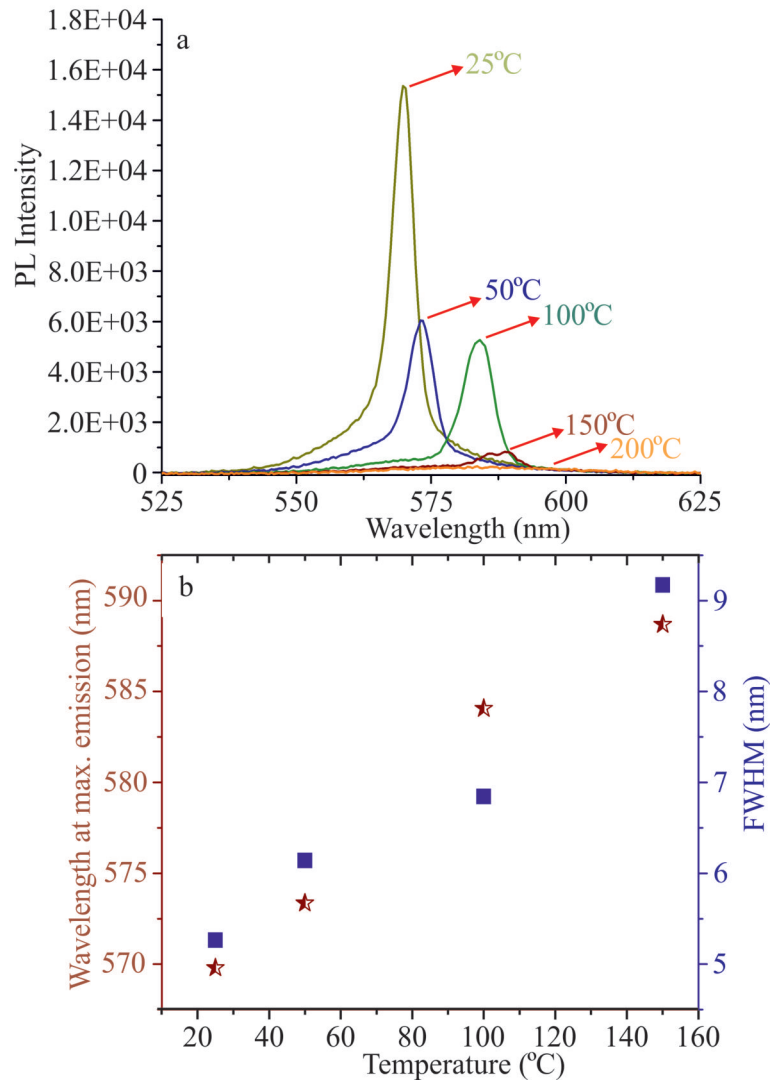
Fig. 6.10 (a) Influence of five different temperatures, 25°C, 50°C, 100°C, 150°C and 200°on the NPs. The PL intensity is decreased as the temperature is increased. (b) The FWHM (blue square) and the peak wavelength (red star) of each spectra is calculated only until 150°C since no ASE is detected at 200°C. As expected, both the peak wavelength and the FWHM increase with the temperature.

Fig. 6.11 corresponds to the behaviour of ASE on the sample as it is left cooling down after being heated for 200°C. The figure suggests that as the sample is cooled down, the abrogated ASE start to visualise. The normalised intensity, shown in Fig 6.11(a) demonstrates the recovering of the intensity with cooling down of sample. Fig 6.11(b) on the other hand represents the corresponding FWHM and peak wavelength at each hour. The FWHM is seen decreasing as the cooling of the sample takes place. Similarly, the peak wavelength is also seen blue-shifting with respect to each hour. Now, considering that the peak wavelength at

150°C is ≈588.78 nm, it is blue shifted by ≈14.23 nm (lower in comparison to red-shifted in Fig. 6.10(b)), with the peak wavelength of ≈574.5 nm at 4th hour. This suggests the possibility of restoring of QWs at some degree once they are baked at high temperatures.

The temperature was also recorded within first 30 minutes, 45 minutes, and then in each hour after the first hour. In first 30 minutes, the temperature was decreased to 45°C, and at 45 minutes, it was recorded to be 28°C. After the first full one hour, the sample was already at room temperature.
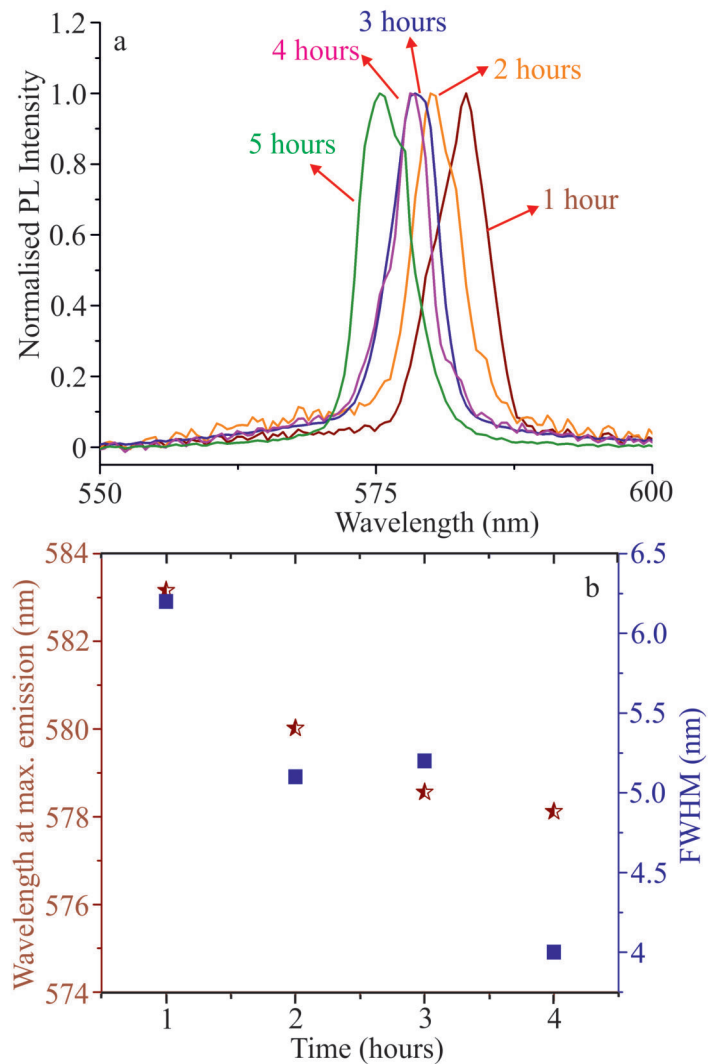
Fig. 6.11 The consequence of cooling down of the sample after it is heated for 200°C. The PL intensity is decreased as the temperature is increased. (a) The normalised intensity observed the regeneration of the ASE as the sample is left cooling. (b) The FWHM (blue square) and the peak wavelength (red star) with respect to each hour demonstrates a decrease in FWHM and blue-shifting of the peak intensity.

Re-generation of optical properties of NPs
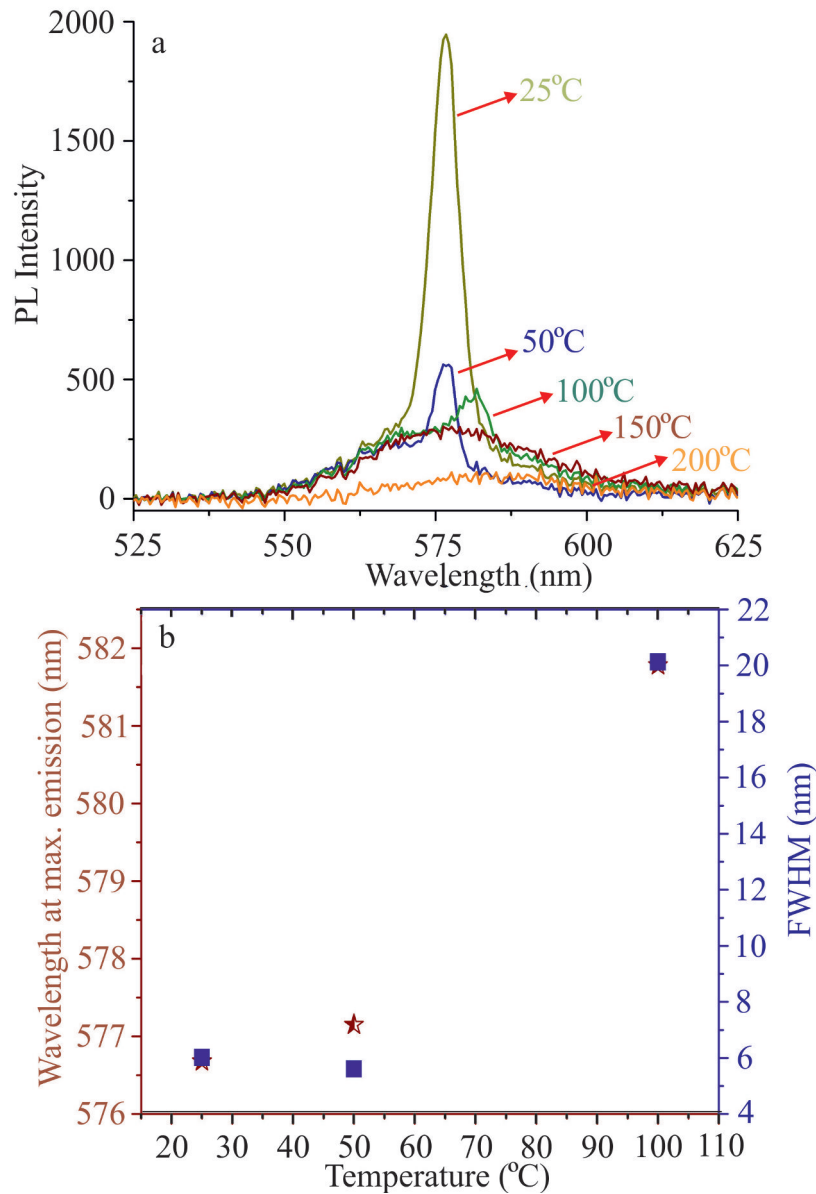
Fig. 6.12 (a) The re-treatment on previously baked sample demonstrated some ASE. The PL intensity is decreased as the temperature is increased. (b) The FWHM (blue square) and the peak wavelength (red star) of each spectra is calculated only until 100°C since no ASE is detected at 150°C and 200°C. As expected, both the peak wavelength and the FWHM increase with the temperature. Note the two red stars underneath blue squares at 25°C and 100°C.

The significant prospect of this analysis is to understand if QWs are sustainable. To study this property, the treatment on previously baked NPs film was carried out. Once the sample

is completely cooled down from the previous experiment (*Section 4.3.3*), the ASE was again measured at room temperature (25°C). The clear indication of the ASE was observed as shown in Fig. 6.12(a). However, the PL intensity decreased drastically in comparison to initial measurement, Fig. 6.10(a).
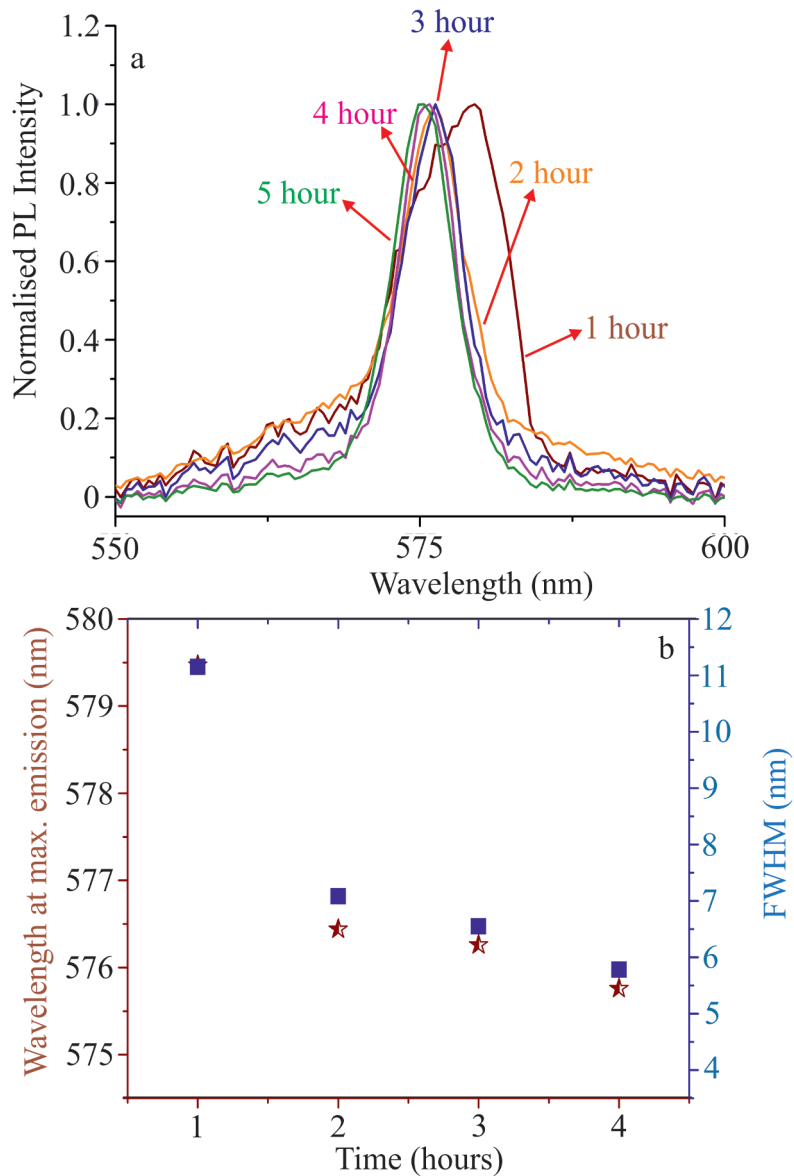
Fig. 6.13 The cooling down of the sample after it is heated until 200°C shows similar trend to 6.10. (a) The regeneration of ASE is observed with cooling down of the sample. (b) The FWHM (blue square) and the peak wavelength (red star) with respect to each hour demonstrates a decrease in FWHM and blue-shifting of the peak intensity. Note a red star underneath a blue square at 1 hour.

Similar to the previous investigation, five different temperatures, 25°C, 50°C, 100°C, 150°C and 200°were chosen. The result showed decrease in PL intensity as the temperature was increased. In comparison to the previous analysis, the ASE was not detected at 150°C. Only fluorescence were observed at the temperatures beyond it. For the FWHM and peak wavelength calculation as shown in Fig. 6.12(b), only 25°C, 50°C and 100°C were chosen since ASE could still be detected at these temperatures. The FWHM (blue square) was expected to increase, however, the value at 50°C showed some irregularities. The peak wavelength (red star) on the other hand showed exponential increase. At room temperature, the peak wavelength is ≈576.69 nm. By the time the temperature was increased to 100°C, peak wavelength was red-shifted by ≈5.2 nm (≈581.9 nm). Note the two red stars underneath blue squares at 25°C and 100°C. The FWHM at 25°C also seems slightly higher (≈6 nm) than the first experiment (*Section 4.3.3*). The increase in temperature to 50°C and 100°gives the FWHM values to be ≈5.5 nm and ≈20 nm respectively.

Again, the cooling down of the sample observed regeneration of ASE. The PL intensity is decreased as the temperature is increased as expected. The Fig. 6.13(a) still follows the trendline as seen in Fig. 6.11, however, the process seems slower this time. Similarly, as shown in Fig 6.13(b), the corresponding FWHM and peak wavelength at each hour shows blue-shifting with respect to the each hour. Now, taking the peak wavelength at 100°C to be ≈581.9 nm, it is blue shifted by about ≈5.9 nm, providing the peak wavelength of ≈576 nm at 4th hour. The change in peak wavelength is lower in comparison to Fig. 6.12(b).

In addition to the temperature influence, an ability of the material to cope laser excitation with respect to time was investigated at room temperature. As demonstrated in Fig. 6.14(a), the peak PL intensity (red triangle) was recorded in each minute. The figure suggests that as the time goes on, the peak PL intensity decreases. The trend line suggests that the material is effective until 5 minutes after which the sign of deterioration is observed. In addition to this, the red-shifting of peak wavelength (blue square) shows sharp variation until 4 minutes although a huge deviation of data is observed in between. After this, the PL intensity remains constant. In between 7 and 10 minutes, there are again some fluctuation, which may be due to surface and deep-level defects in NPs [185]. The maximum red-shifting of the peak wavelength is recored to be ≈0.92 nm (570.73 nm at 1 minute and 571.65 nm at 4 minutes).

Afterwards, an additional investigation was conducted to observe red-shifting of the peak wavelength with respect to temperature in each degree. The first measurement was carried out at 25°C, followed by 30°C. Afterwards, the intensity (red triangle) was measured at each degree. One can observe in Fig.6.14(b) that the intensity (red triangle) decreases exponentially. The corresponding peak intensities with respect to the wavelength plot (blue square) shows the red-shifting of the peak as the temperature increases. Another observation

is that there is a linear sharp jump from 25°C to 30°C. The peak wavelength remains constant afterwards until 35°C when again sharp jump is observed. After 40°C, the peak wavelength fluctuates. Although some irregularities are observed in between 40°C to 50°C, one can say that the red-shifting is not that significant here. This can be related with Fig. 6.14(a), which declares that a single spot of the sample is deteriorated after 4 minutes of excitation. It is possible that after 40°C, the sample was already deteriorated. However, considering in between 25°C and 30°C, and 35°C to 40°C, the red-shifting of ≈1.85 nm per 5°C is observed.
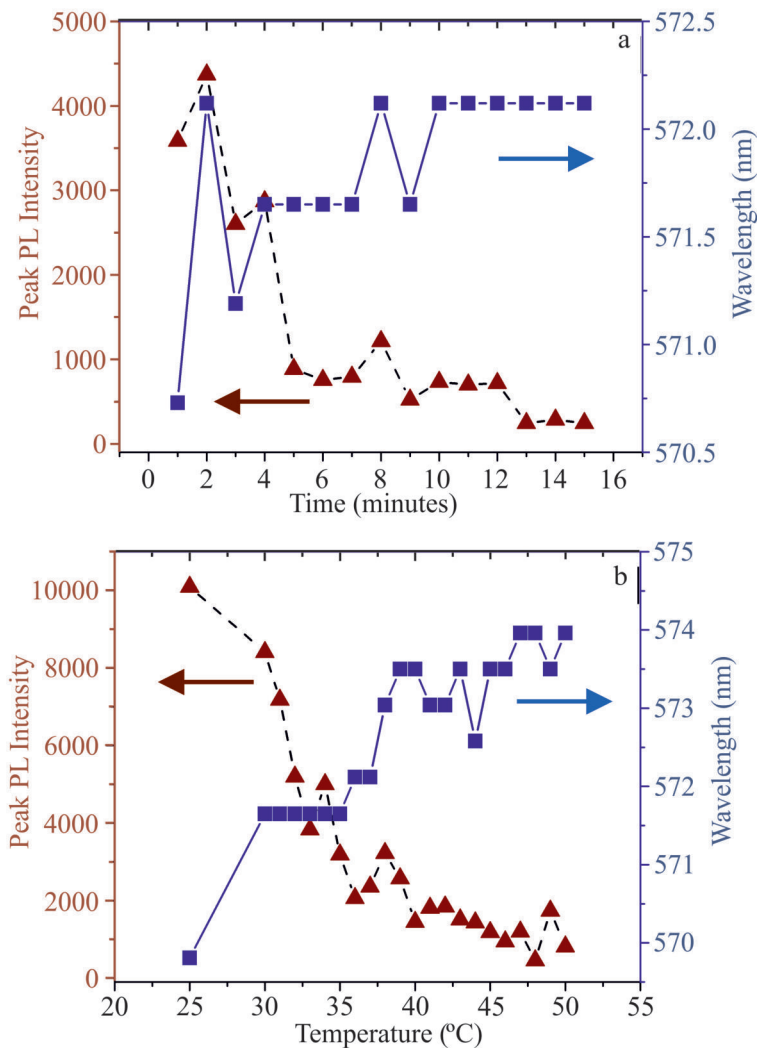
Fig. 6.14 (a) Investigation of the stability of the material at room temperature, (b) Change in the peak wavelength and the intensity with respect to the temperature in each degree.

Polymer substrate for the temperature influence investigation on nanoparticles

The temperature influence on ASE investigation is extended to the evaluation on alternative substrate. From the previous experiment, it is clear that ASE of QWs withstands as high as 150°C for the initial experiment, on glass substrate. However, considering the polymer substrate degrades faster, it is still considered a reasonable investigation to understand the limitation.
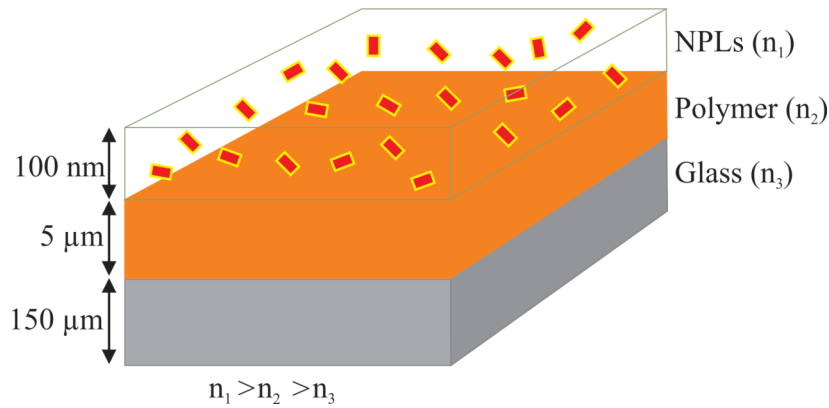
Fig. 6.15 The schematic diagram of three-level interface of QWs/polymer/glass for laser excited PL measurement.
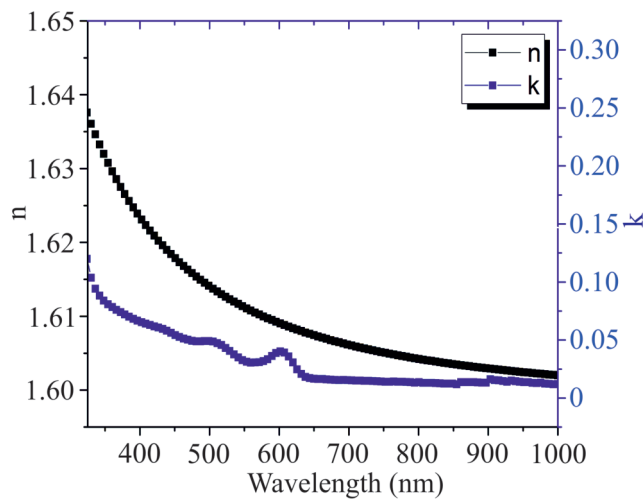
Fig. 6.16 Refractive index of Quantum NPs with respect to different wavelengths.

The high refractive index of CdSe/CdS NPs [51] makes this material more advantageous for waveguide applications. To understand the compatibility of QWs once coated on top of polymer with regards to ASE observation is the key matter of this investigation. As shown in Fig. 6.15. The QWs solution was spin-coated on the polymer film deposited on glass slide,

also by spin-coating. The polymer adopted in this particular investigation is Ormocore, with refractive index is ≈1.56. The refractive index of a glass is 1.52 and that of NPs is shown in Fig 6.16, calculated by measuring reflectance and transmittance, and using Fresnel equations. The figure indicates higher refractive index of NPs in comparison to polymer, which promotes the properties of waveguide once they are excited with line focus. The sample preparation and the experiment was carried out similar to the previous sections of this chapter. Unlike the investigation on glass substrate, the measurement was carried out in every 10°C interval since the decay time of the polymer substrate is expected to be faster than the glass. The result is shown in Fig. 6.17(a).
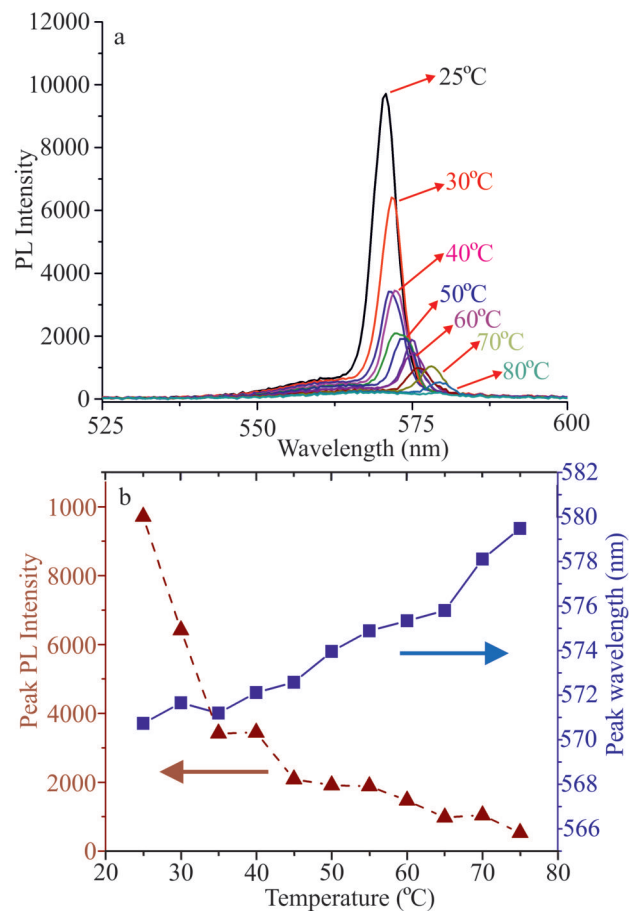
Fig. 6.17 The effect of increase in temperature of QWs deposited on the polymer substrate. The sample is heated until 80°C. (a) The decrease of ASE is observed with heating of the sample. (b) The FWHM (blue square) and the peak wavelength (red star) with respect to each temperature demonstrates a increase in FWHM and decrease blue-shifting of the peak intensity.

The intensity was measured at 25°C, followed by every 5°C interval. The investigation was carried out only up to 80°C since the ASE was disappeared at this temperature. The peak PL intensity and wavelength until 75°C at every 5°C is shown in Fig. 6.17 (b). The trendline of the peak intensity (red) closely matches with the Fig. 6.10 (a) since it is decreasing exponentially. The peak wavelength trendline (blue) also shows red-shifting as the temperature is increased. From 25°C to 75°C, it demonstrates total of ≈8.5 nm shift, making it ≈0.85 nm per 5°C. As the temperature increases, the rate of AR is increased as more energy is lost as heat. This results in an electron to acquire lower energy than it originally owned. Hence, the recombination of an electron-hole pair occurs in higher wavelength. This process is hugely influenced as the temperature increases to higher level.
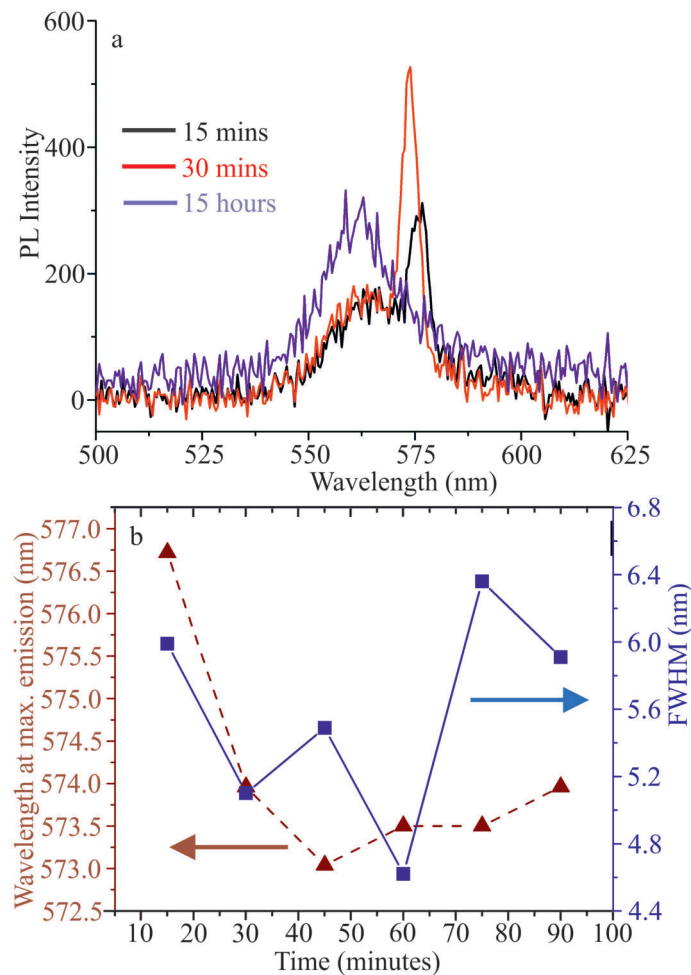
Fig. 6.18 (a) The cooling down of the sample after it is heated for 80°C, regenerated ASE. (b) The FWHM (blue square) and the peak wavelength (red star) with respect to each time labelled in Fig. a demonstrates a blue-shifting of the peak intensity. The scattered FWHM values show the overall values less than 6.4 nm.

Similar to the NPs/glass interface, an additional investigation was conducted to observe regeneration of the ASE peak when the sample was cooled. Fig. 6.18(a) confirms the regeneration of ASE as the temperature was decreased. The emission was measured at every 15 minutes until 90th minutes. At first 15th and 30th minutes, the temperature was decreased to 30°C and 45°C, respectively. Since the shifting of the peak was not so significantly visible and the peak intensities showed no definite trendlines, all the peaks were densely pack, making the lines indistinguishable. Therefore, only the data from 15 minutes, 30 minutes and 15 hours is shown. At the same spot, the measurement was carried out in 15th hour and it showed no signature of ASE as shown in figure. The result suggest that the polymer as a substrate deforms permanently. It is possible that when temperature increases, the polymer expands while depositing the NPs layered on the top. By the time the sample is extremely hot (eg. 80°C), most of the NPs would already have been absorbed into the polymer layer. Now, when this sample is cooled down, the sample becomes compact making NPs unaccessible to the exciting laser. The FWHM and peak wavelength during the cooling process is shown in Fig. 6.18(b). As observed, the peak wavelength (red triangle) with respect to each time as labelled in figure indicates a blue-shifting of the peak intensity until 45th minutes after which the peak is seen redirecting towards red-shifting. This states that the agglomeration of the NPs/polymer starts after 45 minutes of cooling down. Noting the peak fluctuation from first 15 mintues until 45 minutes, ≈3.75 nm of blue-shifting was observed. The FWHM values do not show definite trendline but all values are less than 6.4 nm.

In summary, the optical properties of thin film QWs (emission wavelength 554 nm) were investigated at high temperature (from room temperature up to 200°C) by pumping with nanosecond, third harmonic of a q-switched Nd:YAG laser (355 nm), 5 ns pulse duration laser. It was observed that ASE of QWs decreased as the temperature was increased, disappearing completely at 200°C. The cooling down of the sample demonstrated regeneration of the ASE, however not prominent as before. The peak fluctuation was also observed during heating and cooling process. These fluctuations, as investigated by previous research [127] has suggested quasi-periodic structure being one of the attributer. Since within particular NPs, each particle have tendency to behave differently due to consequence of agglomeration, and size deviation, this leads to formation of different cavity length. This indeed results in the occurrence of peak fluctuation in response to higher excitation energies. The photo-degradation investigation on QWs suggested that a single spot is functional for up to 4 minutes, after which is shows some degradation. The examination on red-shifting of the particle in every 5°C yielded the value of ≈1.85 nm per 5°C, undeniably showing a huge potential as a temperature sensor. The comparison between glass and polymer as a substrate, concluded glass as a better choice with polymer being deformed after 75°C.

6.3 Energy levels of the quantum nanoparticles using single and two-photon excitation

The discrete energy levels of the NPs depend on their size. This dependence leads onto the investigation of the emission spectra depending upon variable excitation energies. In this section, further evaluation on three NPs (QDs, QRs and QWs) are carried out to understand their optical properties and their adaptation into the polymer. The section is sub-divided into two parts; (i) two-photon absorption. The perception of two-photon absorption uses two photons with double the wavelength to excite the molecule [186]. For the recombination process, only one photon is released. The released photon consists of the wavelength equivalent to one-photon absorption. This technique estimates the energy band gap of the NPs, (ii) Afterwards, a procedure to embedded inorganic CdSe/Cds core/shell QDs, QRs and core/crown QWs NPs into a photocurable polymer, Ormocore is accomplished. The emphasis is given in generating the procedure to successfully embed the semiconductor NPs into the polymer that can be still functional afterwards. This opens an opportunity to investigate possible inorganic lasers using semiconductor NPs, which have great advantage over organic lasers due to their better photostability and an ability to achieve high output power. Additionally, the investigated optical properties, achieved by embedding NPs into high-refractive index photocurable polymer materials, such as in this research, can have huge advantage in photonic applications.

Since the NPs adopted in this thesis are self-made, the importance of investigating their optical properties more in detail carries a huge affirmation, and hence, can be acknowledged. Considering accurate spectra for both kind of absorption, the absorption efficiency with respect to different wavelength can be achieved. Additionally, the better understanding of the discrete energy levels of the NPs can be obtained.

Similar to previous sections in this chapter, a standard 18x18x0.15 mm^3 microscopic cover glasses were chosen as the substrates for the NPs. After the substrate was cleaned throughly with the same technique, a total amount of 20 µL solution of the QDs, QRs and QWs particles were spin-coated at a speed of 50 rps for 50 seconds. The film was pumped under a Ti:Sa tunable (705 nm-980 nm) femtosecond laser (80 MHz) (Table 4.6), measuring the fluorescence spectra at an interval of each 5 nm wavelength. The measurement technique, explained in *Section 4.1.4* was opted for the investigation. For two photon excitation, considering the interaction length of 1.5 mm, the pump pulse energy at the sample was set to 0.11 W.

Discussion

Energy Levels of Nanoparticles

The NPs investigating in this thesis are core/shell CdSe/CdS QDs, QRs and core/crown CdSe/CdS QWs. The concept of core/shell or core/crown initiates the arrangement of four-level systems, creating better efficiency of lasing system. Since the bandgap of CdS is higher than CdSe, FRET is expected from CdS to be transferred to CdSe, considering they are acting as donor and acceptor, respectively. For FRET to occur, the CdS and CdSe must be in close distance (normally 1 to 10 nm), requirement met by the arrangement of these NPs. Additionally, the emission spectrum of CdS must overlap the absorption spectrum of the CdSe [187].

For two-photon absorption to occur, two photons must hit the molecule within few femtoseconds of each other, requiring a focused laser that has high repetition rate and a huge intensity. On the other hand, one-photon absorption only requires low power UV/Vis excitation. The basic understanding of the energy bands of the NPs are investigated with the PL luminescence assessment. For the standard spherical bulk CdSe and CdS NPs, the bandgap of 1.74 eV and 2.48 eV, respectively are considered [188, 189]. Considering the potential well position of valence and conduction band of bulk CdSe at -6.5 eV and -4 eV, and of CdS at -6 eV and 4.3 eV, respectively [190, 191], the energy levels of each material can be estimated with regards to the behaviour of electrons in the conduction band.
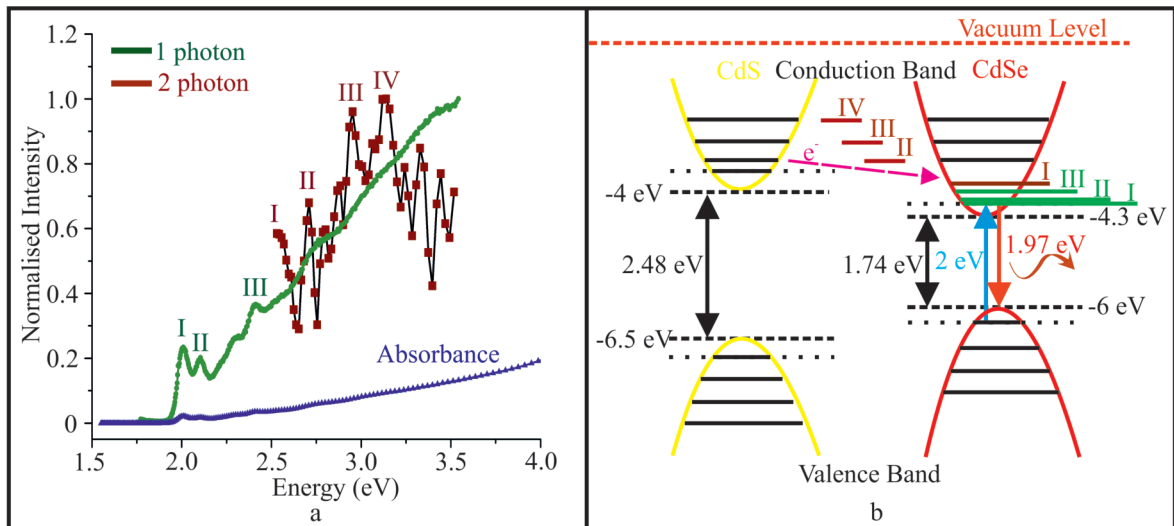
Fig. 6.19 (a) The investigation of PL emission by one-photon (green) and two-photon absorption (red) QDs, (b) The energy levels of the QDs, estimated by the PL spectra of both methods. Note, the energy of two-photon-absorption (red) is multiplied by two, to make them in similar range with one-photon absorption.

Table 6.1 Multiphoton excitation dependent excitonic emission of quantum dots. Note, the energy of two-photon-absorption (red) is multiplied by two, to make them in similar range with one-photon absorption.

Absorption	Peak I (eV)	Peak II (eV)	Peak III (eV)	Peak IV (eV)
one-photon	2	2.11	2.41	-
two-photon	2.53	2.71	2.95	3.14

Fig. 6.19 represents the diagrammatic illustration of the inspected absorption on QDs. The one-photon absorption showed discrete peaks at the 2 eV (green I), 2.11 eV (green II) and 2.41 eV (green III). These peaks perfectly overlap with the three noticeable humps from absorbance (blue line). It is assumed that this electronic transition is related to the exciton. It is expected that the bandgap of all the confined NPs have higher in comparison to bulk due to their different shape and sizes. However, since all these energies are lower than the bandgap of bulk CdS, these excitons are expected to occur in CdSe, whose bandgap after size confinement is $\approx$2 eV (size $\approx$6 nm, including the one monolayer CdS shell). The two-photon absorption (red line) shows two distinct highest peaks quite close to each other; 2.95 eV (III) and 3.14 eV (IV). Although there are other small peaks but they can be considered not so notable in comparison to peaks III and IV.

The energy band structure of the CdSe/CdS QDs is schematically shown in Fig. 6.19(b) with valence and conduction bands. The two valence and two conduction bands of CdSe and CdS, shown in the figure gives the characteristics of four levels laser system. The bulk bandgaps for both particles are shown by dashed lines whereas dotted lines shows their bandgaps after they are confined.

In terms of two-photon absorption, there are discrete peaks labelled by red I-IV in Fig. 6.19(a). Since the energies of these peaks are higher than the CdSe/CdS bandgaps, both of them share these bands, as labelled in Fig. 6.19(b). The one-photon absorption green I-III are expected to occur in CdSe only since the energies they represent is lower than the bandgap of CdS. The emission energy is $\approx$1.97 eV, corresponding to the wavelength of $\approx$629 nm. Note that this is lower than the absorption (2 eV). It is due to exciton binding energies of CdS and CdSe, which are 27 meV and 15 meV, respectively. The transfer of energy from CdS to CdSe is shown by pink arrow in the same figure. Table 6.1 represents the data peak energies for both one-photon and two-photon absorption displayed in Fig. 6.19(a). Note, the energy bands with respect to the PL emission was drawn only for QDs, as the focus was to understand the energy bandgaps with respect to the PL emission, excited by two-photon and one-photon. The peaks with respect to one-photon and two-photon absorption on QDs are listed in Table 6.1.
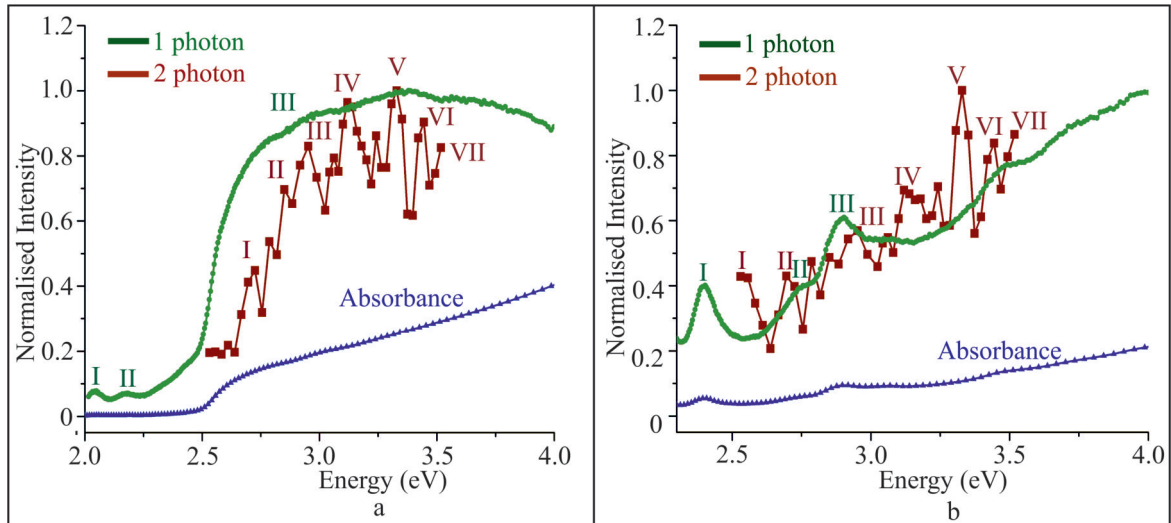
Fig. 6.20 The investigation of PL emission by one-photon and two-photon absorption on (a) QRs and (b) QWs.

Fig. 6.20(a,b) represents the PL emission of QRs and QWs, respectively. Similar to QDs, both QRs and QWs show clear and noticeable peaks with regards to two-photon excitation in comparison to one-photon. The absorption with QRs shows around 2.1 eV (green I), which is similar to QDs. After 2.5 eV, one can say the peak intensity is seen increasing quadratically until 2.73 eV (III) after which it posses bulk properties. The two-photon absorption (red line) favours slightly at the energy levels of 3.12 eV (IV) and 3.33 eV (V).

The QWs, as shown in Fig. 6.20(b) demonstrates the peak line (green I) around 2.40 eV. Since the bandgap of QWs is expected to be lower than QDs and QRs, it is possible that some peaks are present below 2.4 eV. However, it was not possible to detect due to the fact that this materials emits at around 2.2 eV. The investigation on QWs has proved that it has more distinct peaks in comparison to all three NPS. With one-photon absorption (green line), three distinct peaks at 2.40 eV (I), 2.73 (II) and 2.9 eV (III) are observed. After 3 eV, a curve increases linearly, representing the favourable emission energy for the particles. With the same particles, two-photon absorption (red line) gives slightly different observation. The highest peak intensity was observed at 3.3 eV (V). Nevertheless, the primitive peaks (I-IV) in QRs and QWs are listed in Table. 6.2 and Table. 6.3, respectively. The peaks energies (V-VII) of all both QRs and QWs at two-photon absorption have same energies; 3.12 eV, 3.33 eV and 3.52 eV.

Table 6.2 Multiphoton excitation dependent excitonic emission of quantum rods.

Absorption	Peak I (eV)	Peak II (eV)	Peak III (eV)	Peak IV (eV)
one-photon	2.1	-	2.73	-
two-photon	2.73	2.85	2.95	3.12

Table 6.3 Multiphoton excitation dependent excitonic emission of quantum wells.

Absorption	Peak I (eV)	Peak II (eV)	Peak III (eV)	Peak IV (eV)
one-photon	2.40	2.73	2.90	-
two-photon	2.53	2.7	2.95	3.12

Theoretically, the use of high repetition rate and high power results in peak intensities increasing quadratically with respect to pump power. This concept was also investigated experimentally for all three NPs and the result is shown in Fig. 6.21.
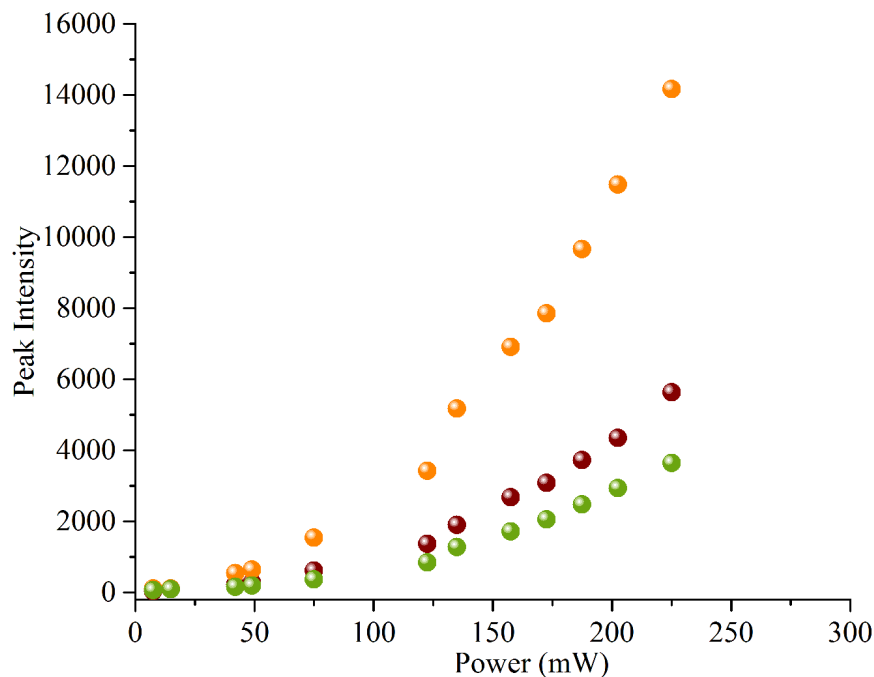
Fig. 6.21 The investigation of PL emission by two-photon absorption on QDs (red), QRs (orange)and QWs (green). The peak intensities increase quadratically with respect to power for all three NPs.

As shown in figure, the trendline of peak intensities have agreed with theoretical hypothesis. In comparison to three NPs, the QRs possessed highest intensity. This could have come from the fact that they have highest concentration.

Quantum nanoparticles embedded polymer for waveguide synthesis

Organic dye lasers have commonly been a topic of investigation[192–194]. However, they possess disadvantage of high bleaching rate, hence are only suitable for low power continuous wave laser system. In this thesis, a similar system was investigated by embedding Rhodamine 6G into Ormosil. Fig 6.22 shows the waveguide synthesised with hybrid rhodamine/ormosil, using photolithograhy process (*Section 4.1.1*). As observed in Fig. 6.22(a),the material was inadequate to withstand electrons from SEM. This makes the possibility of future application as a high power laser with this material intrusive. Nevertheless, the material demonstrated an ability to perfectly adapt under the laser diode illumination of 450 nm, reflecting perfectly green colour, as shown in Fig. 6.22(b).
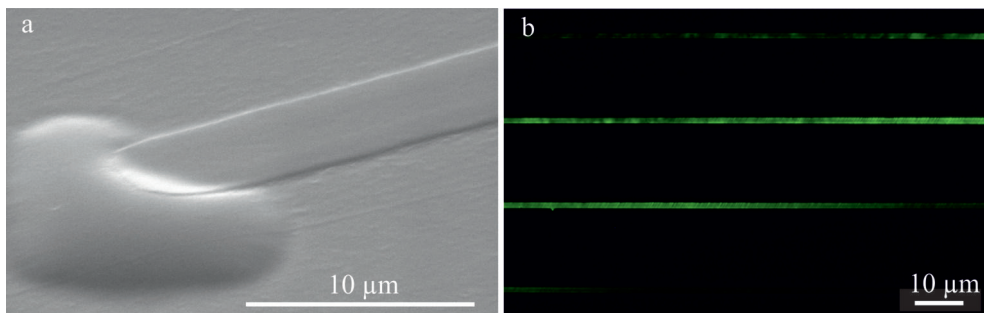
Fig. 6.22 (a) SEM image of the synthesised waveguide. (b) The similar waveguide under the light microscope. (c) The waveguide is illuminated by 450 nm laser diode. (d) The darkfield view image of the illuminated waveguide.

This complication opens the idea of investigating possible optical properties by embedding quantum NPs into Ormocore. The advantage of Ormocore is, it is soluble in Toluene, the storage solvent for NPs. The sample preparation was carried out by the following method:

- A tube consists of NPs in toluene was centrifuged at 6000 revolution per minute (RPM) for 10 minutes to separate.

- Similar amount of methanol was added to the solution in order to separate toluene from NPs.

- Toluene was removed from the tube.

- In remaining NPs, required amount of Ormocore was added and stirred for few hours.

- In order to synthesis waveguide using photolithography method, 4 wt% Ir 369 was added in the solution.

- Depending upon the required thickness, a thinner (microresist) was added.

With the solution prepared from above method, the transmission and absorption spectra were measured using UV/Vis spectrometer, as shown in Fig. 6.23. With the Cd concentration, listed in Table 4.8, QRs looks better in absorbing the wavelength of 365 nm out of three NPs. Hence, the waveguide was synthesised using Ormocore/QRs. The synthesising procedure is shown in Table 6.4.
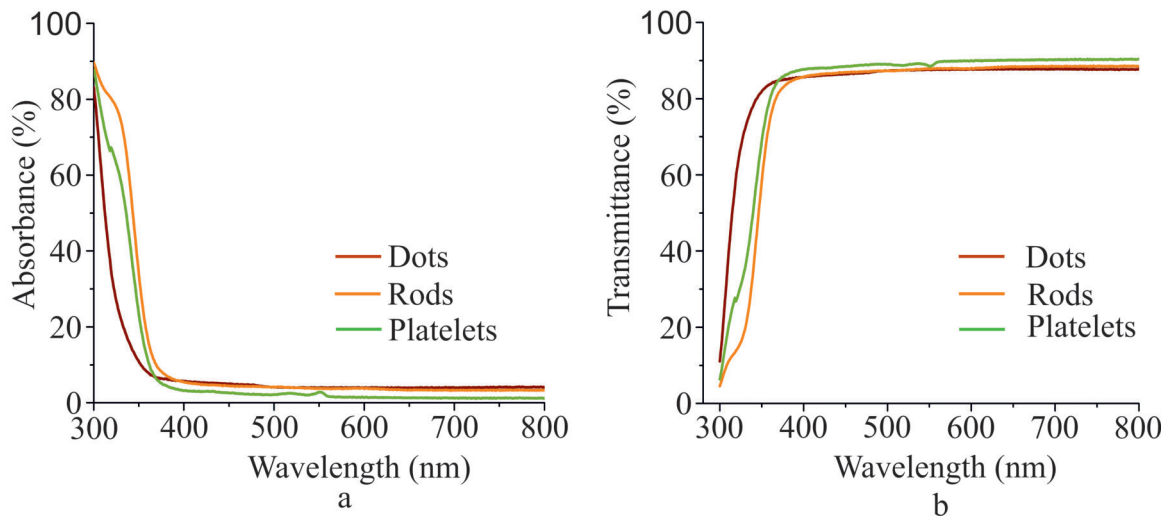
Fig. 6.23 The absorption and transmittance spectra of Ormocore/NPs, each with the Cd ion concentration listed in Table 4.8.

Table 6.4 Step needed for the fabrication of waveguide.

Procedure	
Softbake	No
Exposure	5-10 minutes in MPP
Postbake	150 degree in UV Oven for 2 hours
Develop	2 minutes in Ormodev
Rinse	Ormodev

The prepared solution was spin-coated at 50 rps for 50 seconds. Using the photolithography process, the required waveguide was synthesised and baked in oven for around 2 hours for better stability. The Ormodev (microresist) was used for the development, followed by rinsing with the same chemical. Fig. 6.24 shows the prepared waveguide illuminated by a

laser diode at 450 nm wavelength. The figure suggests that the possibility of embedding NPs into the polymer and synthesising of the structure is possible. However, the problem of the agglomeration arises. Due to high degree of agglomeration, scattering is quite high as shown in Fig. 6.24(c-d). For the waveguide, high scattering is the disturbance since most light will scatter rather than travelling through it. The scattering usually comes form big agglomerated lumps.
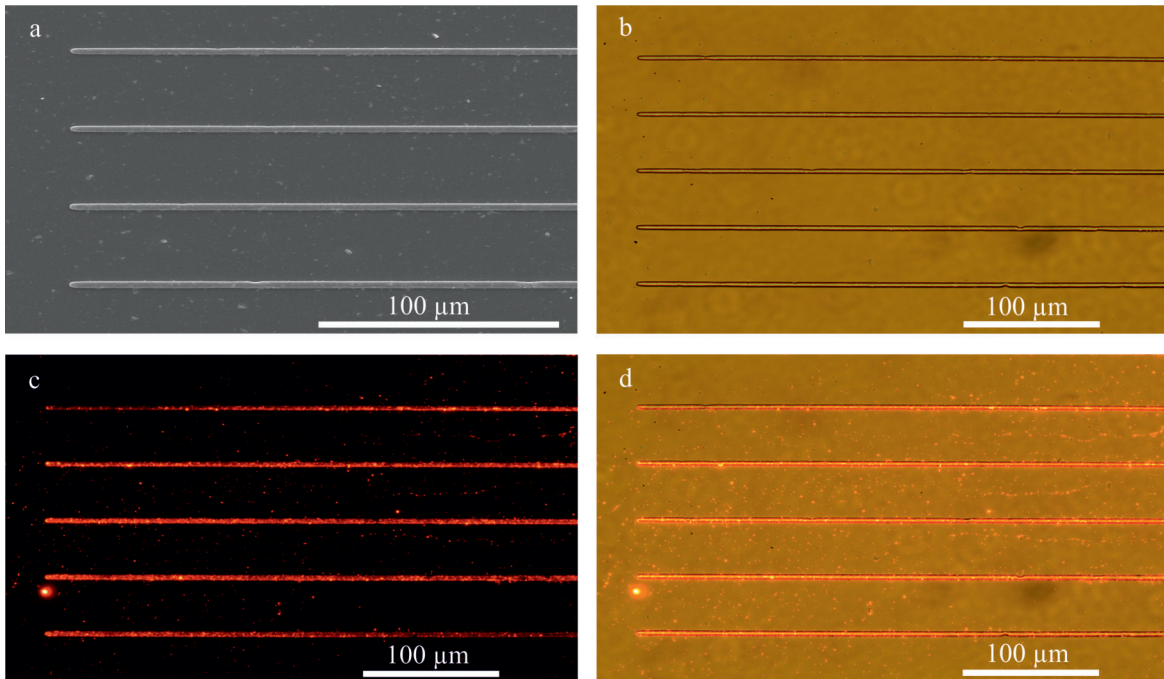
Fig. 6.24 (a) SEM image of the synthesised waveguide. (b) The same waveguide under the light microscope. (c) The darkfield view image of the illuminated waveguide. (d) The brightfield view image of the illuminated waveguide.

To understand the properties of the waveguide in Fig. 6.24, intensity of a single waveguide was measured by an optical fibre as shown in Fig. 6.25. The measurement was carried out by exciting the Ormocore-CdSe/CdS core/shell QRs waveguide with the pump diode wavelength of 450 nm. The figure represents high degree of fluorescence ability at the peak wavelength of $\approx$625 nm. This confirms the adaptability of the NPs into the polymer. However, considering the higher absorption spectrum of this material from Fig. 6.23 until the wavelength of 355 nm, limited amount of light is expected to pass through the waveguides. Therefore, new procedure is introduced in order to get more homogeneous solution.
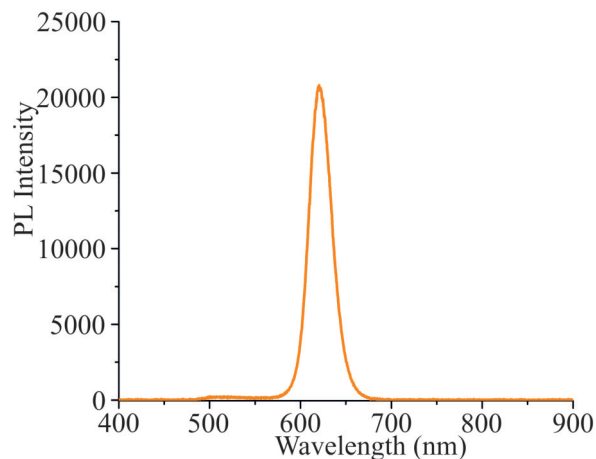
Fig. 6.25 Intensity profile of Ormocore-CdSe/CdS core/shell QRs waveguide observes high fluoresensing ability of the materials.

In new procedure, the stage of centrifugation is avoided. The NPs were used as it was dispersed in toluene. Instead, some amount of toluene was added into ormocore. This process makes the two system in similar environment. The solution was stirred until they were clear, which took few hours. Afterwards, the NPs/toluene solution was added into the Ormocore/toluene solution. Immediately after the mixture, the solution becomes milky. Therefore, the next stage is to stir it overnight. To understand the capability of this solution, the mixture was spin-coated on the glass slide and the ASE measurement was carried out with nanosecond pumping (Table 4.4). The varied energies are shown in Fig. 6.26. As demonstrated in the figure, from 15-60 μJ, only fluorescence was detect. When the energy was increased up to 900 μJ, ASE was discovered at the peak wavelength of 589 nm, yielding the FWHM of ≈4 nm.
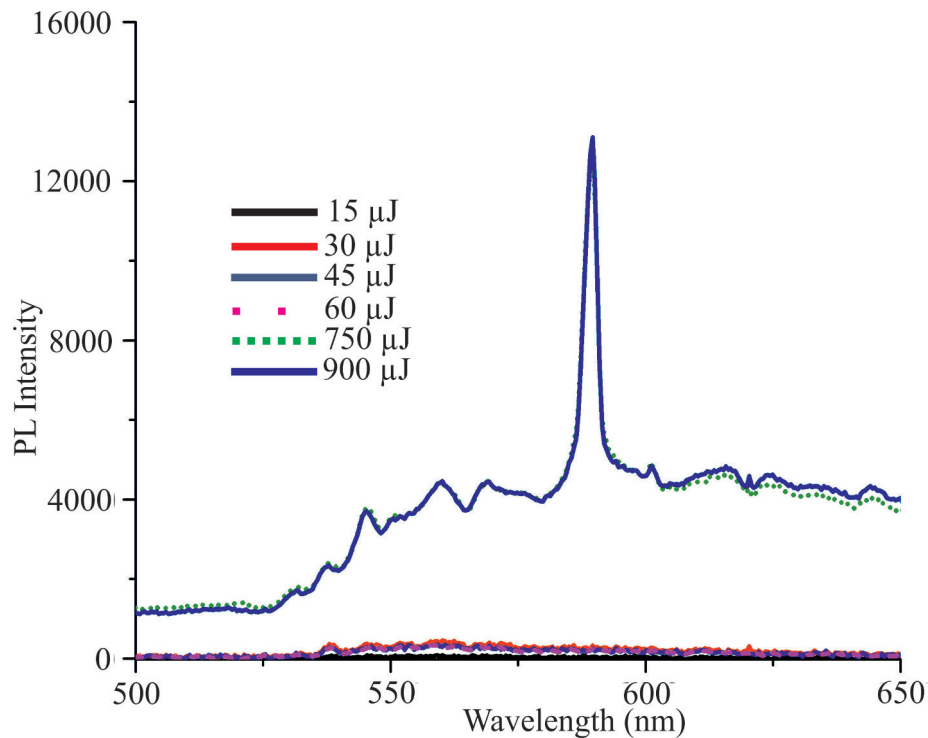
Fig. 6.26 The ASE measurement on polymer/QWs mixture. The amplification is observed at the energy of 750 μJ.

The conception of polymer/NPs hybrid has huge potential in sensor applications when they have compact 2-D or 3-D structures. To address this objective, small and large 2-D waveguides were synthesised as demonstrated in Fig. 6.27. To open the possibility of multiple choices in polymer as well to understand the possible dimensions of the waveguide, they were synthesised with different materials. Fig.6.27(a-b) represents the small sized waveguides prepared with ormosil. These waveguides are ≈150 nm in width and ≈20 μm in length. The largest sized waveguides achieved in this thesis is demonstrated in Fig.6.27(c-d). These waveguides are ≈7 μm in width with the length similar to the small sized waveguides, which is ≈20 μm. Fig.6.27(c) represents the waveguide synthesised with hybrid Ormoclear/QRs, whereas Fig.6.27(d) represents the neodymium doped ormosil waveguide.
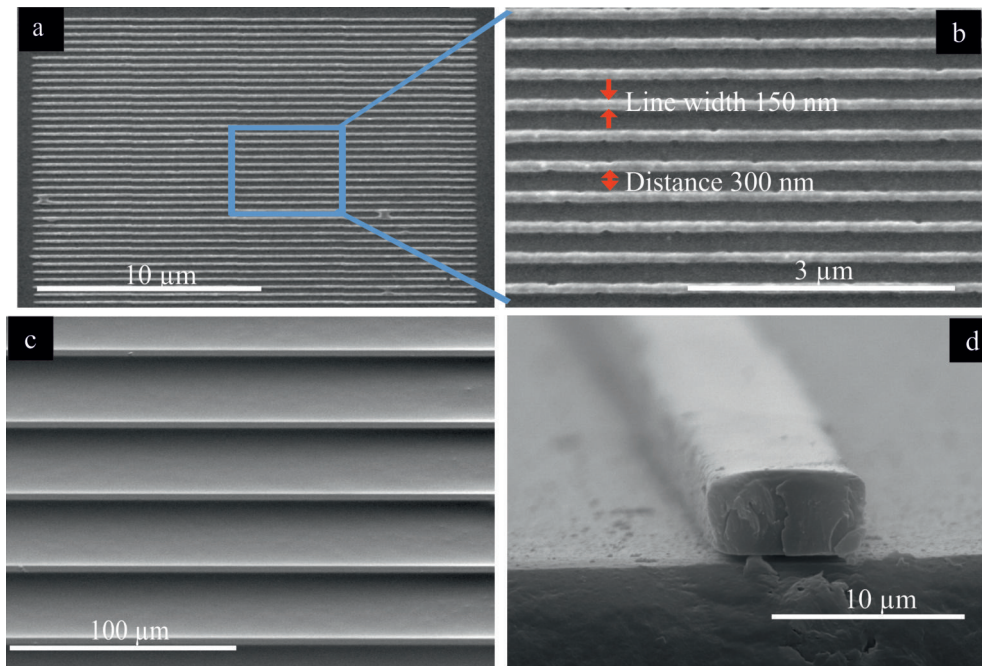
Fig. 6.27 Large waveguides, tested with (a) Ormoclear/QRs and (b) Ormosil/Nd crystals.

In summary, more detailed investigation on the energy bandgaps of the chosen NPs were studied. The spin-coated thin films in the thickness range of 150-200 nm for all three NPs were produced and the PL intensity were measured by single-photon and two-photon excitation. The single photon excitation was carried out in UV/Vis spectrometer and two-photon was observed by Ti:Sa tunable (705 nm-980 nm). With the observed intensity at the interval of each 5 nm wavelength, their behaviour was analysed with respect to the intensity measured. The peak wavelength with respect to two-photon absorptions for QDs, QRs and QWs were 395 nm 372.5 nm and 372.7 nm, respectively. At these peak wavelengths, the power variation measurement was done to cross-check the intensity profile with respect to each power.

Afterwards, an ability of these NPs to embed into the photocurable polymer was investigated. It was observed that once they were mixed, the absorption properties of the materials altered. To avoid the agglomeration problem, further investigation was carried out to make the solution a clear mixture of polymer/NPs. With this solution, the NPs, which has an ability to give lowest ASE threshold, i.e QWs was investigated under nanosecond for gain measurement. As a result, ASE was observed at pump fluence of 1.11 Jcm^{-2}. This demonstrates the potential combination of NPs/polymer to synthesis complicated 2-D and 3-D sensor systems and optical waveguide.

Conclusion

The prospect of using metals and semiconductor nanoparticles (NPs) in the development of optical sensor materials has been studied with respect to their optical properties. The thesis was divided into two parts; choosing two different approaches.

The **surface plasmon polaritons** (SPPs) investigation was carried out based on achieving longer propagation length (L_{SPP}). The different properties that affects the SPPs propagation length, such as deposition methods, types of metals, thickness of the metals and the measurement methods were considered. The primary choice of the metals were polycrystalline gold and silver. Evaporation and sputtering were chosen as the deposition methods. The chosen characterisation methods consist of microscope projection photolithography (MPP), grating-coupling method and the leakage radiation microscopy (LRM). The subwavelength scattering lines as grids were synthesised on glass slides with MPP to excite the plasmons. On top of the grids, gold and silver of different thicknesses were separately deposited with evaporation and sputtering techniques. The evaluation was first carried out with grating-coupling method and the metal with optimum thickness ($\approx$50 nm) was characterised also with LRM. The comparison between different metals claimed silver to have longer L_{SPP} due to their lower absorption effects. With regards to different fabrication process, the dependence of L_{SPP} on different deposition methods was minimal. The thickness variation of the metals also showed similar L_{SPP} for thin metals films. However, thick gold films produced longer L_{SPP} with sputtering method whereas evaporation method was observed prominent for thick silver films. In comparison between both metals, silver films showed better propagation properties though their performance was limited by their sensitive surfaces. Additionally, atomically flat crystalline gold flakes (Au^F) were produced and grooves (130 nm x 1 μm) were milled into them. The L_{SPP} on the flakes were evaluated with the incident light of 633 nm and 800 nm. The acquired values were compared with polycrystalline gold flakes (PAu^F), synthesised by lift-off process. The chapter concludes that grating-coupling method is suitable for investigating thicker metals whereas LRM is more applicable for investigating thin metal films based on the leaked radiation.

The evaluation of optical properties of **semiconductor nanoparticles** (NPs) to understand their prospectus in sensing devices were examined. Cadmium selenide/cadmium sulphide (CdSe/CdS) core/shell quantum dots (QDs), quantum rods (QRs) and 5 monolayer thick core/crown quantum wells (QWs) at ambient temperature were considered and amplified spontaneous emission (ASE) comparison was carried out based on threshold values achieved by different NPs. The ASE evaluations were carried out under femtosecond 2ω (400 nm) and ω (800 nm) at a repetition rate of 20 Hz and 50 Hz respectively with 50-fs pulse duration. The comparison between three NPs confirmed QWs to have a lowest threshold, using femtosecond pumping. The nanosecond pumping showed similar threshold for both QRs and QWs but no ASE emission for QDs.

In addition, an insight on dependence of ASE on QWs while influenced by change in temperature was addressed. The investigation emphasised on observation on change in full width half maximum (FWHM) and red-shifted wavelengths as the temperature was changed. It was observed that as the temperature increased, the emission decreased, yielding just about fluorescence at higher temperature.

Later in this chapter, the study on the energy bandgaps of respective NPs were conducted with one-photon and two-photon absorption. The outcome demonstrated that QWs consisted of more distinct peaks in comparison to all three NPs. In terms of the QRs, there were no definite peaks in both cases. The trendline of one-photon absorption on QDs showed slight similarities with one-photon absorption peak of QWs whereas two-photon absorption of QDs matched slightly with two-photon absorption of QRs. The energy diagram of QDs was schematically drawn from the information achieved from the trendline of one-photon and two-photon absorption. The final section in this chapter investigated a procedure to generate inorganic semiconductor NPs doped polymer waveguides. The CdSe/Cds quantum NPs based on different sizes, such as QDs, QRs and 5-monolayer QWs were embedded into the photocurable polymer, ormocore in order to produce waveguides using two-step photolithography process.

Scientific Perspectives

The investigation on SPPs could be extended into further metals, such as Copper and Aluminium. The SPPs L_{SPP} in these metals are expected to be highly influenced by oxidation, however, the quantitative measurement would be favourable demonstration for proper comparison. Since the efficiency of SPPs propagation enormously depend on the dimensions and quality of the subwavelength scattering lines, SPPs investigation with grating-coupling method could be further continued by modifying these properties.

In semiconductor NPs, the ASE measurement with length interaction method was carried out only for nanosecond pumping since the emphasis was done to measure the lowest ASE threshold. This investigation could be extended further to measure gain, using femtosecond laser as well. The increase in temperature observed the disappearance of amplification emission, and indeed regeneration as the temperature was decreased. This declaration could be further implied into cryogenic temperatures.

The ASE measurement on NPs/polymer can be extended into different kind of NPs. The optical amplification property was only observed with QWs embedded into ormocore. The experiment could be extended also to QDs and QRs. Additionally, the waveguide synthesis from QRs/polymer hybrid could be prolonged to understand the possibility of guiding light through it. The waveguide could be synthesised and evaluated by coupling in the light from one end, measuring at the other end. This provides the efficiency of the synthesised waveguides.

References

[1] R. P. Feynman, *The pleasure of finding things out: The best short works of Richard P. Feynman.* Helix Books, 2005.

[2] R. P. Feynman, "There's plenty of room at the bottom [data storage]," *Microelectrome-chanical Systems, Journal of*, vol. 1, no. 1, pp. 60–66, 1992.

[3] C. Buzea, I. I. Pacheco, and K. Robbie, "Nanomaterials and nanoparticles: Sources and toxicity," *Biointerphases*, vol. 2, no. 4, pp. MR17–MR71, 2007.

[4] N. Taniguchi *et al.*, "On the basic concept of nanotechnology," in *Proc. Intl. Conf. Prod. Eng. Tokyo, Part II, Japan Society of Precision Engineering*, pp. 18–23, 1974.

[5] K. E. Drexler, "Engines of creation 2.0: the coming era of nanotechnology," 2006.

[6] T. Hanemann and D. V. Szabó, "Polymer-nanoparticle composites: from synthesis to modern applications," *Materials*, vol. 3, no. 6, pp. 3468–3517, 2010.

[7] I. Freestone, N. Meeks, M. Sax, and C. Higgitt, "The lycurgus cup—a roman nanotechnology," *Gold Bulletin*, vol. 40, no. 4, pp. 270–277, 2007.

[8] C. Rhodes, S. Franzen, J.-P. Maria, M. Losego, D. N. Leonard, B. Laughlin, G. Duscher, and S. Weibel, "Surface plasmon resonance in conducting metal oxides," *Journal of Applied Physics*, vol. 100, no. 5, p. 054905, 2006.

[9] A. V. Zayats and I. I. Smolyaninov, "Near-field photonics: surface plasmon polaritons and localized surface plasmons," *Journal of Optics A: Pure and Applied Optics*, vol. 5, no. 4, p. S16, 2003.

[10] S. A. Maier, *Plasmonics: fundamentals and applications.* Springer Science & Business Media, 2007.

[11] T. Birr, U. Zywietz, P. Chhantyal, B. N. Chichkov, and C. Reinhardt, "Ultrafast surface plasmon-polariton logic gates and half-adder," *Optics express*, vol. 23, no. 25, pp. 31755–31765, 2015.

[12] A. B. Evlyukhin and S. I. Bozhevolnyi, "Surface plasmon polariton scattering by small ellipsoid particles," *Surface science*, vol. 590, no. 2, pp. 173–180, 2005.

[13] A. Evlyukhin and S. Bozhevolnyi, "Surface plasmon polariton guiding by chains of nanoparticles," *Laser Physics Letters*, vol. 3, no. 8, p. 396, 2006.

[14] I. P. Radko, S. I. Bozhevolnyi, A. B. Evlyukhin, and A. Boltasseva, "Surface plasmon polariton beam focusing with parabolic nanoparticle chains," *Optics express*, vol. 15, no. 11, pp. 6576–6582, 2007.

[15] W. C. Chan, D. J. Maxwell, X. Gao, R. E. Bailey, M. Han, and S. Nie, "Luminescent quantum dots for multiplexed biological detection and imaging," *Current opinion in biotechnology*, vol. 13, no. 1, pp. 40–46, 2002.

[16] E. O. Chukwuocha, M. C. Onyeaju, and T. S. Harry, "Theoretical studies on the effect of confinement on quantum dots using the brus equation," 2012.

[17] Y. Gogotsi, *Nanomaterials handbook*. CRC press, 2006.

[18] T. Hanemann and D. V. Szabó, "Polymer-nanoparticle composites: from synthesis to modern applications," *Materials*, vol. 3, no. 6, pp. 3468–3517, 2010.

[19] V. I. Klimov, A. Mikhailovsky, S. Xu, A. Malko, J. Hollingsworth, C. Leatherdale, H.-J. Eisler, and M. Bawendi, "Optical gain and stimulated emission in nanocrystal quantum dots," *Science*, vol. 290, no. 5490, pp. 314–317, 2000.

[20] J. Pitarke, V. Silkin, E. Chulkov, and P. Echenique, "Theory of surface plasmons and surface-plasmon polaritons," *Reports on progress in physics*, vol. 70, no. 1, p. 1, 2006.

[21] R. W. Wood, "On a remarkable case of uneven distribution of light in a diffraction grating spectrum," *Proceedings of the Physical Society of London*, vol. 18, no. 1, p. 269, 1902.

[22] I. Newton, "Opticks: or a treatise of the reflexions, refractions, inflexions and colours of light," 1704.

[23] G. Mie, "Beiträge zur optik trüber medien, speziell kolloidaler metallösungen," *Annalen der physik*, vol. 330, no. 3, pp. 377–445, 1908.

[24] J. Zenneck, "Über die fortpflanzung ebener elektromagnetischer wellen längs einer ebenen leiterfläche und ihre beziehung zur drahtlosen telegraphie," *Annalen der Physik*, vol. 328, no. 10, pp. 846–866, 1907.

[25] A. Sommerfeld, "Über die ausbreitung der wellen in der drahtlosen telegraphie," *Annalen der Physik*, vol. 333, no. 4, pp. 665–736, 1909.

[26] U. Fano, "Some theoretical considerations on anomalous diffraction gratings," *Physical Review*, vol. 50, no. 6, p. 573, 1936.

[27] R. Ritchie, "Plasma losses by fast electrons in thin films," *Physical Review*, vol. 106, no. 5, p. 874, 1957.

[28] C. Powell and J. Swan, "Origin of the characteristic electron energy losses in magnesium," *Physical Review*, vol. 116, no. 1, p. 81, 1959.

[29] E. Stern and R. Ferrell, "Surface plasma oscillations of a degenerate electron gas," *Physical Review*, vol. 120, no. 1, p. 130, 1960.

[30] C. L. Haynes, A. D. McFarland, and R. P. V. Duyne, "Surface-enhanced raman spectroscopy," *Analytical Chemistry*, vol. 77, no. 17, pp. 338–A, 2005.

[31] D. K. Gramotnev and S. I. Bozhevolnyi, "Plasmonics beyond the diffraction limit," *Nature photonics*, vol. 4, no. 2, pp. 83–91, 2010.

[32] C. Lemke, C. Schneider, T. Leißner, D. Bayer, J. W. Radke, A. Fischer, P. Melchior, A. B. Evlyukhin, B. N. Chichkov, C. Reinhardt, *et al.*, "Spatiotemporal characterization of spp pulse propagation in two-dimensional plasmonic focusing devices," *Nano letters*, vol. 13, no. 3, pp. 1053–1058, 2013.

[33] P. Chhantyal, T. Birr, D. Hinrichs, U. Zywietz, D. Dorfs, B. Glasmacher, A. B. Evlyukhin, and C. Reinhardt, "Influence of fabrication methods of gold and silver layers on surface plasmon polaritons propagation length," *Plasmonics*, pp. 1–8, 2017.

[34] T. W. Ebbesen, C. Genet, and S. I. Bozhevolnyi, "Surface-plasmon circuitry," *Physics Today*, vol. 61, no. 5, p. 44, 2008.

[35] Y. Fang and M. Sun, "Nanoplasmonic waveguides: towards applications in integrated nanophotonic circuits," *Light: Science & Applications*, vol. 4, no. 6, p. e294, 2015.

[36] S. Kawata, Y. Inouye, and P. Verma, "Plasmonics for near-field nano-imaging and superlensing," *Nature Photonics*, vol. 3, no. 7, pp. 388–394, 2009.

[37] J. N. Anker, W. P. Hall, O. Lyandres, N. C. Shah, J. Zhao, and R. P. Van Duyne, "Biosensing with plasmonic nanosensors," *Nature materials*, vol. 7, no. 6, pp. 442–453, 2008.

[38] C. Reinhardt, R. Kiyan, S. Passinger, A. Stepanov, A. Ostendorf, and B. Chichkov, "Rapid laser prototyping of plasmonic components," *Applied Physics A*, vol. 89, no. 2, pp. 321–325, 2007.

[39] C. Reinhardt, A. Seidel, A. B. Evlyukhin, W. Cheng, and B. N. Chichkov, "Mode-selective excitation of laser-written dielectric-loaded surface plasmon polariton waveguides," *JOSA B*, vol. 26, no. 12, pp. B55–B60, 2009.

[40] C. Reinhardt, A. Seidel, A. Evlyukhin, W. Cheng, R. Kiyan, and B. Chichkov, "Direct laser-writing of dielectric-loaded surface plasmon–polariton waveguides for the visible and near infrared," *Applied Physics A*, vol. 100, no. 2, pp. 347–352, 2010.

[41] C. Reinhardt, A. B. Evlyukhin, W. Cheng, T. Birr, A. Markov, B. Ung, M. Skorobogatiy, and B. N. Chichkov, "Bandgap-confined large-mode waveguides for surface plasmon-polaritons," *JOSA B*, vol. 30, no. 11, pp. 2898–2905, 2013.

[42] R. F. Oulton, V. J. Sorger, D. Genov, D. Pile, and X. Zhang, "A hybrid plasmonic waveguide for subwavelength confinement and long-range propagation," *Nature Photonics*, vol. 2, no. 8, pp. 496–500, 2008.

[43] Y. Ma, "Surface plasmon polaritons based nanophotonic devices and their applications," 2015.

[44] P. Yeh, *Optical waves in layered media*, vol. 61. Wiley-Interscience, 2005.

[45] G. V. Naik, V. M. Shalaev, and A. Boltasseva, "Alternative plasmonic materials: beyond gold and silver," *Advanced Materials*, vol. 25, no. 24, pp. 3264–3294, 2013.

[46] P. Drude, "Zur elektronentheorie der metalle," *Annalen der Physik*, vol. 306, no. 3, pp. 566–613, 1900.

[47] P. Drude, "Zur elektronentheorie der metalle; ii. teil. galvanomagnetische und thermomagnetische effecte," *Annalen der Physik*, vol. 308, no. 11, pp. 369–402, 1900.

[48] C. Powell, "Analysis of optical-and inelastic-electron-scattering data. ii. application to al*," *JOSA*, vol. 60, no. 1, pp. 78–93, 1970.

[49] A. D. Rakić, A. B. Djurišić, J. M. Elazar, and M. L. Majewski, "Optical properties of metallic films for vertical-cavity optoelectronic devices," *Applied optics*, vol. 37, no. 22, pp. 5271–5283, 1998.

[50] P. B. Johnson and R.-W. Christy, "Optical constants of the noble metals," *Physical review B*, vol. 6, no. 12, p. 4370, 1972.

[51] E. D. Palik, *Handbook of optical constants of solids*, vol. 3. Academic press, 1998.

[52] R. L. Olmon, B. Slovick, T. W. Johnson, D. Shelton, S.-H. Oh, G. D. Boreman, and M. B. Raschke, "Optical dielectric function of gold," *Physical Review B*, vol. 86, no. 23, p. 235147, 2012.

[53] M.-L. Thèye, "Investigation of the optical properties of au by means of thin semitransparent films," *Physical Review B*, vol. 2, no. 8, p. 3060, 1970.

[54] P. Winsemius, F. Van Kampen, H. Lengkeek, and C. Van Went, "Temperature dependence of the optical properties of au, ag and cu," *Journal of Physics F: Metal Physics*, vol. 6, no. 8, p. 1583, 1976.

[55] A. Otto, "Excitation of nonradiative surface plasma waves in silver by the method of frustrated total reflection," *Zeitschrift für Physik*, vol. 216, no. 4, pp. 398–410, 1968.

[56] E. Kretschmann and H. Raether, "Notizen: radiative decay of non radiative surface plasmons excited by light," *Zeitschrift für Naturforschung A*, vol. 23, no. 12, pp. 2135–2136, 1968.

[57] H. Raether, *Surface plasmons on smooth surfaces*. Springer, 1988.

[58] W. Kern, *Thin film processes II*, vol. 2. Academic press, 2012.

[59] K. Tai, P. Turner, and D. Bacon, "The structure of evaporated-and dc-sputtered films of gold and silver deposited on glass," *Journal of Vacuum Science & Technology*, vol. 6, no. 4, pp. 687–689, 1969.

[60] M. Kuttge, E. Vesseur, J. Verhoeven, H. Lezec, H. Atwater, and A. Polman, "Loss mechanisms of surface plasmon polaritons on gold probed by cathodoluminescence imaging spectroscopy," *Applied Physics Letters*, vol. 93, no. 11, p. 113110, 2008.

[61] T. Gupta, *Copper interconnect technology*. Springer Science & Business Media, 2010.

[62] N. Sardana, T. Birr, S. Schlenker, C. Reinhardt, and J. Schilling, "Surface plasmons on ordered and bi-continuous spongy nanoporous gold," *New Journal of Physics*, vol. 16, no. 6, p. 063053, 2014.

[63] R. Parsons, "Sputter deposition processes," *Thin film processes II*, pp. 177–208, 1991.

[64] J. A. Thornton, "The microstructure of sputter-deposited coatings," *Journal of Vacuum Science & Technology A*, vol. 4, no. 6, pp. 3059–3065, 1986.

[65] V. Švorčík, P. Slepička, J. Švorčíková, M. Špírková, J. Zehentner, and V. Hnatow-icz, "Characterization of evaporated and sputtered thin au layers on poly (ethylene terephtalate)," *Journal of applied polymer science*, vol. 99, no. 4, pp. 1698–1704, 2006.

[66] D. A. Svintsov, A. V. Arsenin, and D. Y. Fedyanin, "Full loss compensation in hybrid plasmonic waveguides under electrical pumping," *Optics express*, vol. 23, no. 15, pp. 19358–19375, 2015.

[67] A. Kolomenski, A. Kolomenskii, J. Noel, S. Peng, and H. Schuessler, "Propagation length of surface plasmons in a metal film with roughness," *Applied optics*, vol. 48, no. 30, pp. 5683–5691, 2009.

[68] D. E. Gray, *American institute of physics handbook*. McGraw-Hill, 1982.

[69] U. Schröder, "Der einfluss dünner metallischer deckschichten auf die dispersion von oberflaechenplasmaschwingungen in gold-silber-schichtsystemen," *Surface Science*, vol. 102, no. 1, pp. 118–130, 1981.

[70] S. Szunerits and R. Boukherroub, *Introduction to Plasmonics: Advances and Applications*. CRC Press, 2015.

[71] J. Zhu, Z. Xu, W. Xu, D. Fu, and S. Song, "New surface plasmon polariton waveguide based on gan nanowires," *Results in Physics*, vol. 7, pp. 381–384, 2017.

[72] K. Q. Le and A. Alù, "Plasmonic gratings for enhanced light-trapping in thin-film organic solar cells," in *CLEO: Science and Innovations*, pp. CF3J–5, Optical Society of America, 2012.

[73] K. A. Willets and R. P. Van Duyne, "Localized surface plasmon resonance spectroscopy and sensing," *Annu. Rev. Phys. Chem.*, vol. 58, pp. 267–297, 2007.

[74] K. Q. Le, A. Abass, B. Maes, P. Bienstman, and A. Alù, "Comparing plasmonic and dielectric gratings for absorption enhancement in thin-film organic solar cells," *Optics express*, vol. 20, no. 101, pp. A39–A50, 2012.

[75] Y. Arakawa and H. Sakaki, "Multidimensional quantum well laser and temperature dependence of its threshold current," *Applied Physics Letters*, vol. 40, no. 11, pp. 939–941, 1982.

[76] V. A. Kharchenko and M. Rosen, "Auger relaxation processes in semiconductor nanocrystals and quantum wells," *Journal of luminescence*, vol. 70, no. 1, pp. 158–169, 1996.

[77] H. Htoon, J. Hollingsworth, R. Dickerson, and V. I. Klimov, "Effect of zero-to one-dimensional transformation on multiparticle auger recombination in semiconductor quantum rods," *Physical review letters*, vol. 91, no. 22, p. 227401, 2003.

[78] D. Chepic, A. L. Efros, A. Ekimov, M. Ivanov, V. Kharchenko, I. Kudriavtsev, and T. Yazeva, "Auger ionization of semiconductor quantum drops in a glass matrix," *Journal of Luminescence*, vol. 47, no. 3, pp. 113–127, 1990.

[79] R. G. Driggers, *Encyclopedia of Optical Engineering: Las-Pho, pages 1025-2048*, vol. 2. CRC press, 2003.

[80] M. Kazes, D. Oron, I. Shweky, and U. Banin, "Temperature dependence of optical gain in cdse/zns quantum rods," *The Journal of Physical Chemistry C*, vol. 111, no. 22, pp. 7898–7905, 2007.

[81] C. She, I. Fedin, D. S. Dolzhnikov, A. Demortière, R. D. Schaller, M. Pelton, and D. V. Talapin, "Low-threshold stimulated emission using colloidal quantum wells," *Nano letters*, vol. 14, no. 5, pp. 2772–2777, 2014.

[82] B. Guilhabert, C. Foucher, A.-M. Haughey, E. Mutlugun, Y. Gao, J. Herrnsdorf, H. Sun, H. Demir, M. Dawson, and N. Laurand, "Nanosecond colloidal quantum dot lasers for sensing," *Optics express*, vol. 22, no. 6, pp. 7308–7319, 2014.

[83] L. Brus, "Electronic wave functions in semiconductor clusters: experiment and theory," *The Journal of Physical Chemistry*, vol. 90, no. 12, pp. 2555–2560, 1986.

[84] L.-s. Li, J. Hu, W. Yang, and A. P. Alivisatos, "Band gap variation of size-and shape-controlled colloidal cdse quantum rods," *Nano Letters*, vol. 1, no. 7, pp. 349–351, 2001.

[85] D. Lincot and G. Hodes, "Chemical solution deposition of semiconducting and non-metallic films: Proceedings of the international symposium," The Electrochemical Society, 2006.

[86] R. Koole, E. Groeneveld, D. Vanmaekelbergh, A. Meijerink, and C. de Mello Donegá, "Size effects on semiconductor nanoparticles," in *Nanoparticles*, pp. 13–51, Springer, 2014.

[87] A. Shabaev and A. L. Efros, "1d exciton spectroscopy of semiconductor nanorods," *Nano letters*, vol. 4, no. 10, pp. 1821–1825, 2004.

[88] M. Achermann, A. P. Bartko, J. A. Hollingsworth, and V. I. Klimov, "The effect of auger heating on intraband carrier relaxation in semiconductor quantum rods," *Nature Physics*, vol. 2, no. 8, pp. 557–561, 2006.

[89] H. Talaat, T. Abdallah, M. Mohamed, S. Negm, and M. A. El-Sayed, "The sensitivity of the energy band gap to changes in the dimensions of the cdse quantum rods at room temperature: Stm and theoretical studies," *Chemical Physics Letters*, vol. 473, no. 4, pp. 288–292, 2009.

[90] J. Xu, D. Battaglia, X. Peng, and M. Xiao, "Photoluminescence from colloidal cds-cdse-cds quantum wells," *JOSA B*, vol. 22, no. 5, pp. 1112–1116, 2005.

[91] J. Butty, Y. Hu, N. Peyghambarian, Y. Kao, and J. Mackenzie, "Quasicontinuous gain in sol-gel derived cds quantum dots," *Applied physics letters*, vol. 67, no. 18, pp. 2672–2674, 1995.

[92] Y. Hu, H. Gie, N. Peyghambarian, S. W. Koch, *et al.*, "Microscopic theory of optical gain in small semiconductor quantum dots," *Physical Review B*, vol. 53, no. 8, p. 4814, 1996.

[93] C. Dang, J. Lee, C. Breen, J. S. Steckel, S. Coe-Sullivan, and A. Nurmikko, "Red, green and blue lasing enabled by single-exciton gain in colloidal quantum dot films," *Nature nanotechnology*, vol. 7, no. 5, pp. 335–339, 2012.

[94] A. L. EFROS and A. Efros, "Interband absorption of light in a semiconductor sphere," *SPIE milestone series*, vol. 180, pp. 71–74, 2005.

[95] V. Dneprovskii, V. I. Klimov, D. Okorokov, and Y. V. Vandyshev, "Strong optical nonlinearities and laser emission of semiconductor microcrystals," *Solid state communications*, vol. 81, no. 3, pp. 227–230, 1992.

[96] I. D. Samuel, E. B. Namdas, and G. A. Turnbull, "How to recognize lasing," *Nature Photonics*, vol. 3, no. 10, pp. 546–549, 2009.

[97] G. Bjork and Y. Yamamoto, "Analysis of semiconductor microcavity lasers using rate equations," *IEEE Journal of Quantum Electronics*, vol. 27, no. 11, pp. 2386–2396, 1991.

[98] P. R. Rice and H. Carmichael, "Photon statistics of a cavity-qed laser: A comment on the laser–phase-transition analogy," *Physical Review A*, vol. 50, no. 5, p. 4318, 1994.

[99] D. Elvira, X. Hachair, V. B. Verma, R. Braive, G. Beaudoin, I. Robert-Philip, I. Sagnes, B. Baek, S. W. Nam, E. A. Dauler, *et al.*, "Higher-order photon correlations in pulsed photonic crystal nanolasers," *Physical Review A*, vol. 84, no. 6, p. 061802, 2011.

[100] M. Facao, A. Lopes, A. Silva, and P. Silva, "Computer simulation for calculating the second-order correlation function of classical and quantum light," *European Journal of Physics*, vol. 32, no. 4, p. 925, 2011.

[101] W. W. Chow, F. Jahnke, and C. Gies, "Emission properties of nanolasers during the transition to lasing," *Light: Science & Applications*, vol. 3, no. 8, p. e201, 2014.

[102] M. G. Ramirez, M. Morales-Vidal, V. Navarro-Fuster, P. G. Boj, J. A. Quintana, J. M. Villalvilla, A. Retolaza, S. Merino, and M. A. Díaz-García, "Improved performance of perylenediimide-based lasers," *Journal of Materials Chemistry C*, vol. 1, no. 6, pp. 1182–1191, 2013.

[103] V. Bulović, V. Kozlov, V. Khalfin, and S. Forrest, "Transform-limited, narrow-linewidth lasing action in organic semiconductor microcavities," *Science*, vol. 279, no. 5350, pp. 553–555, 1998.

[104] L. Persano, P. D. Carro, E. Mele, R. Cingolani, D. Pisignano, M. Zavelani-Rossi, S. Longhi, and G. Lanzani, "Monolithic polymer microcavity lasers with on-top evaporated dielectric mirrors," *Applied physics letters*, vol. 88, no. 12, p. 121110, 2006.

[105] C. She, I. Fedin, D. S. Dolzhnikov, P. D. Dahlberg, G. S. Engel, R. D. Schaller, and D. V. Talapin, "Red, yellow, green, and blue amplified spontaneous emission and lasing using colloidal cdse nanoplatelets," *ACS nano*, vol. 9, no. 10, pp. 9475–9485, 2015.

[106] Z. Deutsch, A. Avidan, I. Pinkas, and D. Oron, "Energetics and dynamics of exciton–exciton interactions in compound colloidal semiconductor quantum dots," *Physical Chemistry Chemical Physics*, vol. 13, no. 8, pp. 3210–3219, 2011.

[107] C. Zhong, P. Fei-peng, H. Xiang-wei, L. Tian-shu, X. Geng, M. Dang, and L. Wei-zhu, "Effects of bandgap shrinkage in femtosecond absorption saturation measurements of gaas film," *Acta Physica Sinica (Overseas Edition)*, vol. 5, no. 9, p. 705, 1996.

[108] Y. P. Varshni, "Temperature dependence of the energy gap in semiconductors," *Physica*, vol. 34, no. 1, pp. 149–154, 1967.

[109] J. Bardeen and W. Shockley, "Deformation potentials and mobilities in non-polar crystals," *Physical Review*, vol. 80, no. 1, p. 72, 1950.

[110] S. Adachi, *Properties of semiconductor alloys: group-IV, III-V and II-VI semiconductors*, vol. 28. John Wiley & Sons, 2009.

[111] J. Fan, Z. Han, Y. Kang, and X. Peng, "A two-photon fluorescent probe for lysosomal thiols in live cells and tissues," *Scientific reports*, vol. 6, 2016.

[112] M. Göppert-Mayer, "Über elementarakte mit zwei quantensprüngen," *Annalen der Physik*, vol. 401, no. 3, pp. 273–294, 1931.

[113] W. Kaiser and C. Garrett, "Two-photon excitation in ca f 2: Eu 2+," *Physical review letters*, vol. 7, no. 6, p. 229, 1961.

[114] P. T. So, C. Y. Dong, B. R. Masters, and K. M. Berland, "Two-photon excitation fluorescence microscopy," *Annual review of biomedical engineering*, vol. 2, no. 1, pp. 399–429, 2000.

[115] W. Denk, J. H. Strickler, W. W. Webb, *et al.*, "Two-photon laser scanning fluorescence microscopy," *Science*, vol. 248, no. 4951, pp. 73–76, 1990.

[116] B.-H. Zhu, H.-C. Zhang, Z.-Y. Zhang, Y.-P. Cui, and J.-Y. Zhang, "Effect of shell thickness on two-photon absorption and refraction of colloidal cdse/cds core/shell nanocrystals," *Applied Physics Letters*, vol. 99, no. 23, p. 231903, 2011.

[117] P. Sorokin and J. Lankard, "Stimulated emission observed from an organic dye, chloro-aluminum phthalocyanine," *IBM Journal of Research and Development*, vol. 10, no. 2, pp. 162–163, 1966.

[118] F. P. Schäfer, W. Schmidt, and J. Volze, "Organic dye solution laser," *Applied Physics Letters*, vol. 9, no. 8, pp. 306–309, 1966.

[119] P. Jing, J. Zheng, M. Ikezawa, X. Liu, S. Lv, X. Kong, J. Zhao, and Y. Masumoto, "Temperature-dependent photoluminescence of cdse-core cds/cdzns/zns-multishell quantum dots," *The Journal of Physical Chemistry C*, vol. 113, no. 31, pp. 13545–13550, 2009.

[120] S. C. Farmer and T. E. Patten, "Photoluminescent polymer/quantum dot composite nanoparticles," *Chemistry of materials*, vol. 13, no. 11, pp. 3920–3926, 2001.

[121] H. Gordillo, I. Suárez, R. Abargues, P. Rodríguez-Cantó, S. Albert, and J. Martínez-Pastor, "Polymer/qds nanocomposites for waveguiding applications," *Journal of Nanomaterials*, vol. 2012, p. 33, 2012.

[122] H. Althues, P. Pötschke, G.-M. Kim, and S. Kaskel, "Structure and mechanical properties of transparent zno/pbdma nanocomposites," *Journal of nanoscience and nanotechnology*, vol. 9, no. 4, pp. 2739–2745, 2009.

[123] D. Sun and H.-J. Sue, "Tunable ultraviolet emission of zno quantum dots in transparent poly (methyl methacrylate)," *Applied Physics Letters*, 2009.

[124] C. M. Tyrakowski and P. T. Snee, "Ratiometric cdse/zns quantum dot protein sensor," *Analytical chemistry*, vol. 86, no. 5, pp. 2380–2386, 2014.

[125] D. Pugh-Thomas, B. M. Walsh, and M. C. Gupta, "Cdse (zns) nanocomposite luminescent high temperature sensor," *Nanotechnology*, vol. 22, no. 18, p. 185503, 2011.

[126] N. Irawati, S. W. Harun, H. A. Rahman, S. S. Chong, N. A. Hamizi, and H. Ahmad, "Temperature sensing using cdse quantum dot doped poly (methyl methacrylate) microfiber," *Applied Optics*, vol. 56, no. 16, pp. 4675–4679, 2017.

[127] C.-S. Wang, T.-Y. Chang, T.-Y. Lin, and Y.-F. Chen, "Biologically inspired flexible quasi-single-mode random laser: An integration of pieris canidia butterfly wing and semiconductors," *Scientific reports*, vol. 4, 2014.

[128] A. Evlyukhin, S. Bozhevolnyi, A. Stepanov, R. Kiyan, C. Reinhardt, S. Passinger, and B. Chichkov, "Focusing and directing of surface plasmon polaritons by curved chains of nanoparticles," *Optics express*, vol. 15, no. 25, pp. 16667–16680, 2007.

[129] V. Kresin and S. Wolf, "Colloquium: electron-lattice interaction and its impact on high t c superconductivity," *Reviews of modern physics*, vol. 81, no. 2, p. 481, 2009.

[130] M. D. Levenson, N. Viswanathan, and R. A. Simpson, "Improving resolution in photolithography with a phase-shifting mask," *IEEE Transactions on electron devices*, vol. 29, no. 12, pp. 1828–1836, 1982.

[131] P. M. Mendes, S. Jacke, K. Critchley, J. Plaza, Y. Chen, K. Nikitin, R. E. Palmer, J. A. Preece, S. D. Evans, and D. Fitzmaurice, "Gold nanoparticle patterning of silicon wafers using chemical e-beam lithography," *Langmuir*, vol. 20, no. 9, pp. 3766–3768, 2004.

[132] A. Heuberger, "X-ray lithography," *Journal of Vacuum Science & Technology B: Microelectronics Processing and Phenomena*, vol. 6, no. 1, pp. 107–121, 1988.

[133] H. T. Soh, K. W. Guarini, and C. F. Quate, *Scanning probe lithography*, vol. 7. Springer Science & Business Media, 2013.

[134] A. Bardea and R. Naaman, "Magnetolithography: From bottom-up route to high throughput," *Small*, vol. 5, no. 3, pp. 316–319, 2009.

[135] C. W. Gwyn, R. Stulen, D. Sweeney, and D. Attwood, "Extreme ultraviolet lithography," *Journal of Vacuum Science & Technology B: Microelectronics and Nanometer Structures Processing, Measurement, and Phenomena*, vol. 16, no. 6, pp. 3142–3149, 1998.

[136] S. Y. Chou, P. R. Krauss, and P. J. Renstrom, "Nanoimprint lithography," *Journal of Vacuum Science & Technology B: Microelectronics and Nanometer Structures Processing, Measurement, and Phenomena*, vol. 14, no. 6, pp. 4129–4133, 1996.

[137] H. H. Solak, C. David, J. Gobrecht, V. Golovkina, F. Cerrina, S. Kim, and P. Nealey, "Sub-50 nm period patterns with euv interference lithography," *Microelectronic Engineering*, vol. 67, pp. 56–62, 2003.

[138] V. R. Manfrinato, L. Zhang, D. Su, H. Duan, R. G. Hobbs, E. A. Stach, and K. K. Berggren, "Resolution limits of electron-beam lithography toward the atomic scale," *Nano letters*, vol. 13, no. 4, pp. 1555–1558, 2013.

[139] B. D. Gates, Q. Xu, M. Stewart, D. Ryan, C. G. Willson, and G. M. Whitesides, "New approaches to nanofabrication: molding, printing, and other techniques," *Chemical reviews*, vol. 105, no. 4, pp. 1171–1196, 2005.

[140] H. Kawata, J. M. Carter, A. Yen, and H. I. Smith, "Optical projection lithography using lenses with numerical apertures greater than unity," *Microelectronic Engineering*, vol. 9, no. 1, pp. 31–36, 1989.

[141] J. C. Love, D. B. Wolfe, H. O. Jacobs, and G. M. Whitesides, "Microscope projection photolithography for rapid prototyping of masters with micron-scale features for use in soft lithography," *Langmuir*, vol. 17, no. 19, pp. 6005–6012, 2001.

[142] T. Birr, U. Zywietz, T. Fischer, P. Chhantyal, A. B. Evlyukhin, B. N. Chichkov, and C. Reinhardt, "Ultrafast surface plasmon-polariton interference and switching in multiple crossing dielectric waveguides," *Applied Physics B*, vol. 122, no. 6, pp. 1–9, 2016.

[143] U. Zywietz, A. B. Evlyukhin, C. Reinhardt, and B. N. Chichkov, "Laser printing of silicon nanoparticles with resonant optical electric and magnetic responses," *Nature communications*, vol. 5, 2014.

[144] U. Zywietz, C. Reinhardt, A. Evlyukhin, T. Birr, and B. Chichkov, "Generation and patterning of si nanoparticles by femtosecond laser pulses.," *Applied Physics A: Materials Science & Processing*, vol. 114, no. 1, 2014.

[145] U. Zywietz, M. K. Schmidt, A. B. Evlyukhin, C. Reinhardt, J. Aizpurua, and B. N. Chichkov, "Electromagnetic resonances of silicon nanoparticle dimers in the visible," *ACS Photonics*, vol. 2, no. 7, pp. 913–920, 2015.

[146] A. P. Hibbins, *Grating coupling of surface plasmon polaritons at visible and microwave frequencies.* PhD thesis, University of Exeter, 2000.

[147] A. Drezet, A. Hohenau, D. Koller, A. Stepanov, H. Ditlbacher, B. Steinberger, F. Aussenegg, A. Leitner, and J. Krenn, "Leakage radiation microscopy of surface plasmon polaritons," *Materials science and engineering: B*, vol. 149, no. 3, pp. 220–229, 2008.

[148] J. J. Serbin, *Fabrication of photonic structures by two-photon polymerization*. Cuvillier Verlag, 2004.

[149] A. Ovsianikov, J. Viertl, B. Chichkov, M. Oubaha, B. MacCraith, I. Sakellari, A. Giakoumaki, D. Gray, M. Vamvakaki, M. Farsari, *et al.*, "Ultra-low shrinkage hybrid photosensitive material for two-photon polymerization microfabrication," *Acs Nano*, vol. 2, no. 11, pp. 2257–2262, 2008.

[150] R. M. Azzam and N. M. Bashara, *Ellipsometry and polarized light*. North-Holland. sole distributors for the USA and Canada, Elsevier Science Publishing Co., Inc., 1987.

[151] A. Ovsianikov, *Investigation of two-photon polymerization technique for applications in photonics and biomedicine*. Cuvillier, 2009.

[152] X. Wu, R. Kullock, E. Krauss, and B. Hecht, "Single-crystalline gold microplates grown on substrates by solution-phase synthesis," *Crystal Research and Technology*, vol. 50, no. 8, pp. 595–602, 2015.

[153] M. A. Hines and P. Guyot-Sionnest, "Synthesis and characterization of strongly luminescing zns-capped cdse nanocrystals," *The Journal of Physical Chemistry*, vol. 100, no. 2, pp. 468–471, 1996.

[154] X. Peng, M. C. Schlamp, A. V. Kadavanich, and A. P. Alivisatos, "Epitaxial growth of highly luminescent cdse/cds core/shell nanocrystals with photostability and electronic accessibility," *Journal of the American Chemical Society*, vol. 119, no. 30, pp. 7019–7029, 1997.

[155] B. O. Dabbousi, J. Rodriguez-Viejo, F. V. Mikulec, J. R. Heine, H. Mattoussi, R. Ober, K. F. Jensen, and M. G. Bawendi, "(cdse) zns core- shell quantum dots: synthesis and characterization of a size series of highly luminescent nanocrystallites," *The Journal of Physical Chemistry B*, vol. 101, no. 46, pp. 9463–9475, 1997.

[156] J. J. Li, Y. A. Wang, W. Guo, J. C. Keay, T. D. Mishima, M. B. Johnson, and X. Peng, "Large-scale synthesis of nearly monodisperse cdse/cds core/shell nanocrystals using air-stable reagents via successive ion layer adsorption and reaction," *Journal of the American Chemical Society*, vol. 125, no. 41, pp. 12567–12575, 2003.

[157] W. Guo, J. J. Li, Y. A. Wang, and X. Peng, "Luminescent cdse/cds core/shell nanocrystals in dendron boxes: superior chemical, photochemical and thermal stability," *Journal of the American Chemical Society*, vol. 125, no. 13, pp. 3901–3909, 2003.

[158] M. A. Hines and P. Guyot-Sionnest, "Bright uv-blue luminescent colloidal znse nanocrystals," *The Journal of Physical Chemistry B*, vol. 102, no. 19, pp. 3655–3657, 1998.

[159] M. Bruchez, M. Moronne, P. Gin, S. Weiss, and A. P. Alivisatos, "Semiconductor nanocrystals as fluorescent biological labels," *science*, vol. 281, no. 5385, pp. 2013–2016, 1998.

[160] M. Han, X. Gao, J. Z. Su, and S. Nie, "Quantum-dot-tagged microbeads for multi-plexed optical coding of biomolecules," *Nature biotechnology*, vol. 19, no. 7, p. 631, 2001.

[161] P. Lippens and M. Lannoo, "Calculation of the band gap for small cds and zns crystallites," *Physical Review B*, vol. 39, no. 15, p. 10935, 1989.

[162] M. D. Tessier, P. Spinicelli, D. Dupont, G. Patriarche, S. Ithurria, and B. Dubertret, "Efficient exciton concentrators built from colloidal core/crown cdse/cds semiconductor nanoplatelets," *Nano letters*, vol. 14, no. 1, pp. 207–213, 2013.

[163] L. Carbone, C. Nobile, M. De Giorgi, F. D. Sala, G. Morello, P. Pompa, M. Hytch, E. Snoeck, A. Fiore, I. R. Franchini, *et al.*, "Synthesis and micrometer-scale assembly of colloidal cdse/cds nanorods prepared by a seeded growth approach," *Nano letters*, vol. 7, no. 10, pp. 2942–2950, 2007.

[164] T. J. Hughes, L. P. Franca, and G. M. Hulbert, "A new finite element formulation for computational fluid dynamics: Viii. the galerkin/least-squares method for advective-diffusive equations," *Computer Methods in Applied Mechanics and Engineering*, vol. 73, no. 2, pp. 173–189, 1989.

[165] H. Libardi and H. Grieneisen, "Guided-mode resonance absorption in partly oxidized thin silver films," *Thin Solid Films*, vol. 333, no. 1, pp. 82–87, 1998.

[166] A. Schmidt, J. Offermann, and R. Anton, "The role of neutral oxygen radicals in the oxidation of ag films," *Thin Solid Films*, vol. 281, pp. 105–107, 1996.

[167] W. Zhang, S. Brongersma, O. Richard, B. Brijs, R. Palmans, L. Froyen, and K. Maex, "Influence of the electron mean free path on the resistivity of thin metal films," *Microelectronic engineering*, vol. 76, no. 1, pp. 146–152, 2004.

[168] Q. Wei, K.-D. Li, J. Lian, and L. Wang, "Angular dependence of sputtering yield of amorphous and polycrystalline materials," *Journal of Physics D: Applied Physics*, vol. 41, no. 17, p. 172002, 2008.

[169] J. J. Foley IV, H. Harutyunyan, D. Rosenmann, R. Divan, G. P. Wiederrecht, and S. K. Gray, "When are surface plasmon polaritons excited in the kretschmann-raether configuration?," *Scientific reports*, vol. 5, 2015.

[170] F. Lacy, "Developing a theoretical relationship between electrical resistivity, temperature, and film thickness for conductors," *Nanoscale research letters*, vol. 6, no. 1, p. 636, 2011.

[171] C. Kan, X. Zhu, and G. Wang, "Single-crystalline gold microplates: synthesis, characterization, and thermal stability," *The Journal of Physical Chemistry B*, vol. 110, no. 10, pp. 4651–4656, 2006.

[172] J.-S. Huang, V. Callegari, P. Geisler, C. Brüning, J. Kern, J. C. Prangsma, X. Wu, T. Feichtner, J. Ziegler, P. Weinmann, *et al.*, "Atomically flat single-crystalline gold nanostructures for plasmonic nanocircuitry," *Nature communications*, vol. 1, p. 150, 2010.

[173] A. V. Krasavin and A. V. Zayats, "Silicon-based plasmonic waveguides," *Optics express*, vol. 18, no. 11, pp. 11791–11799, 2010.

[174] M. Kuttge, F. J. G. de Abajo, and A. Polman, "How grooves reflect and confine surface plasmon polaritons," *Optics express*, vol. 17, no. 12, pp. 10385–10392, 2009.

[175] Z. Xu, T. Li, D.-H. Zhang, C. Yan, D. Li, L. Y. Tobing, F. Qin, Y. Wang, X. Shen, and T. Yu, "Groove-structured metasurfaces for modulation of surface plasmon propagation," *Applied Physics Express*, vol. 7, no. 5, p. 052001, 2014.

[176] S. I. Bozhevolnyi, V. S. Volkov, E. Devaux, and T. W. Ebbesen, "Channel plasmon-polariton guiding by subwavelength metal grooves," *Physical review letters*, vol. 95, no. 4, p. 046802, 2005.

[177] S. I. Bozhevolnyi, V. S. Volkov, E. Devaux, J.-Y. Laluet, and T. W. Ebbesen, "Channel plasmon subwavelength waveguide components including interferometers and ring resonators," *Nature*, vol. 440, no. 7083, pp. 508–511, 2006.

[178] I. Gryczynski, J. Malicka, W. Jiang, H. Fischer, W. C. Chan, Z. Gryczynski, W. Grudzinski, and J. R. Lakowicz, "Surface-plasmon-coupled emission of quantum dots," *The Journal of Physical Chemistry B*, vol. 109, no. 3, pp. 1088–1093, 2005.

[179] A. M. Lakhani, K. Yu, and M. C. Wu, "Lasing in subwavelength semiconductor nanopatches," *Semiconductor Science and Technology*, vol. 26, no. 1, p. 014013, 2010.

[180] M. Marceddu, M. Saba, F. Quochi, A. Lai, J. Huang, D. V. Talapin, A. Mura, and G. Bongiovanni, "Charged excitons, auger recombination and optical gain in cdse/cds nanocrystals," *Nanotechnology*, vol. 23, no. 1, p. 015201, 2011.

[181] F. Todescato, I. Fortunati, S. Gardin, E. Garbin, E. Collini, R. Bozio, J. J. Jasieniak, G. Della Giustina, G. Brusatin, S. Toffanin, *et al.*, "Soft-lithographed up-converted distributed feedback visible lasers based on cdse–cdzns–zns quantum dots," *Advanced Functional Materials*, vol. 22, no. 2, pp. 337–344, 2012.

[182] F. Fan, O. Voznyy, R. P. Sabatini, K. T. Bicanic, M. M. Adachi, J. R. McBride, K. R. Reid, Y.-S. Park, X. Li, A. Jain, *et al.*, "Continuous-wave lasing in colloidal quantum dot solids enabled by facet-selective epitaxy," *Nature*, 2017.

[183] H. Kim, K.-S. Cho, H. Jeong, J. Kim, C.-W. Lee, W.-k. Koh, Y.-G. Roh, S. W. Hwang, and Y. Park, "Single-mode lasing from a monolithic microcavity with few-monolayer-thick quantum dot films," *ACS Photonics*, vol. 3, no. 9, pp. 1536–1541, 2016.

[184] N. Tschirner, H. Lange, A. Schliwa, A. Biermann, C. Thomsen, K. Lambert, R. Gomes, and Z. Hens, "Interfacial alloying in cdse/cds heteronanocrystals: A raman spectroscopy analysis," *Chemistry of Materials*, vol. 24, no. 2, pp. 311–318, 2012.

[185] V. Kumar, V. Kumar, S. Som, J. Neethling, E. Olivier, O. Ntwaeaborwa, and H. Swart, "The role of surface and deep-level defects on the emission of tin oxide quantum dots," *Nanotechnology*, vol. 25, no. 13, p. 135701, 2014.

[186] J. Ehrlich, X. Wu, I.-Y. Lee, Z.-Y. Hu, H. Röckel, S. Marder, and J. Perry, "Two-photon absorption and broadband optical limiting with bis-donor stilbenes," *Optics letters*, vol. 22, no. 24, pp. 1843–1845, 1997.

[187] S. A. Hussain, "An introduction to fluorescence resonance energy transfer (fret)," *arXiv preprint arXiv:0908.1815*, 2009.

[188] O. Mandelung, "Data in science and technology: Semiconductors other than group iv elements and iii-v compounds," 1992.

[189] M. Molnár, Y. Fu, P. Friberg, and Y. Chen, "Optical characterization of colloidal cdse quantum dots in endothelial progenitor cells," *Journal of nanobiotechnology*, vol. 8, no. 1, p. 2, 2010.

[190] L.-J. Tzeng, C.-L. Cheng, and Y.-F. Chen, "Enhancement of band-edge emission induced by defect transition in the composite of zno nanorods and cdse/zns quantum dots," *Optics letters*, vol. 33, no. 6, pp. 569–571, 2008.

[191] V. Vermeeren, S. Wenmackers, P. Wagner, and L. Michiels, "Dna sensors with diamond as a promising alternative transducer material," *Sensors*, vol. 9, no. 7, pp. 5600–5636, 2009.

[192] O. Peterson, S. Tuccio, and B. Snavely, "Cw operation of an organic dye solution laser," *Applied Physics Letters*, vol. 17, no. 6, pp. 245–247, 1970.

[193] V. K. Goncharov, L. Y. Min'ko, and S. Mikhnov, "Some effects of the rhodamine laser radiation on absorbing materials," *Kvantovaya Elektronika*, no. 5, pp. 112–116, 1971.

[194] W. Sha, C.-H. Liu, and R. Alfano, "Spectral and temporal measurements of laser action of rhodamine 640 dye in strongly scattering media," *Optics letters*, vol. 19, no. 23, pp. 1922–1924, 1994.

Appendix A

Surface Plasmon Polaritons

A.1 Values of Lorentz-Drude model parameters

Table A.1 Values of Lorentz-Drude model parameters

Parameters	Silver	Gold
f_0	0.845	0.760
γ_0	0.048	0.053
f_1	0.065	0.024
γ_1^{α}	3.886	0.241
ω_1^{α}	0.816	0.415
f_2	0.124	0.010
γ_2	0.452	0.345
ω_2	4.481	0.830
f_3	0.011	0.071
γ_3	0.065	0.870
ω_3	8.185	2.969
f_4	0.840	0.601
γ_4	0.916	2.494
ω_4	9.083	4.304
f_5	5.646	4.384
γ_5	2.419	2.214
ω_5	20.29	13.32

A.2 Python code for calculating Propagation Length on air/metal interface

The following code is an example of calculation of L_{SPP} for gold (Air/Metal Interface). The outcome is shown in Fig. 2.5. Similar code was used for silver, using dielectric constants from [50, 51].

```python
>>> from __future__ import division
>>> import math
>>> import numpy as np
>>> import pandas as pd
>>> import matplotlib.pyplot as plt
>>> from matplotlib.font_manager import FontProperties
>>> hfont = {'fontname':'Times_New_Roman', 'size':'22'} #
    font_and_size_for_graph
>>> plt.rcParams["font.family"] = "Times_New_Roman"
>>> plt.rcParams["font.size"] = "23"

>>> E_air = 1 #dielectric_constant_of_air
>>> c= 300000000000000000 #unit is in nm/s

>>> df = pd.DataFrame.from_csv('johnson_christy_gold_silver.csv') #
    dielectric constants from [36]
>>> E_gold_real_1 = df['E1(gold)'].values.tolist()
>>> E_gold_imaginary_1 = df['E2(gold)'].values.tolist()
>>> wavelength_1 = list(df.index)

>>> df = pd.DataFrame.from_csv('palik_metal.csv') #dielectric constants
    from [37]
>>> E_gold_real_2 = df['E1(gold)'].values.tolist()
>>> E_gold_imaginary_2 = df['E2(gold)'].values.tolist()
>>> wavelength_2 = list(df.index)

>>> df = pd.DataFrame.from_csv('olmon.csv') #dielectric constants from
    [38]
>>> E_gold_real_3 = df['E1(evaporated_gold)'].values.tolist()
>>> E_gold_imaginary_3 = df['E2(evaporated_gold)'].values.tolist()
>>> wavelength_3 = list(df.index)

>>> def omega():
>>>     result=[]
>>>     for item in wavelength_1:
>>>         x = item #wavelength
```

```
>>>          omega = (2*np.pi*c/x)
>>>          result.append((x, omega))
>>>      return result
>>> result1 = omega()

>>> def cal_kspp_imaginary_gold_1(result1):
>>>      result=[]
>>>      loop = 0
>>>      for item in result1:
>>>          omega= item[1]
>>>          x= item[0]
>>>          kspp_imaginary= (omega/c)*(np.sqrt(((E_gold_real_1[loop]*
    E_air)/(E_gold_real_1[loop]+E_air)))**(3/2))*(E_gold_imaginary_1[loop
    ]/(2*(E_gold_real_1[loop]**2)))
>>>          result.append((omega, kspp_imaginary))
>>>          loop += 1
>>>      return result
>>> result2 = cal_kspp_imaginary_gold_1(result1)

>>> def cal_prop_length_gold_1(result2):
>>>       result=[]
>>>       for position, item in enumerate(result2):
>>>           kspp_imaginary= item[1]
>>>           x= result1[position][0]
>>>           prop_length = (1/(2*kspp_imaginary))/1000
>>>           print x, prop_length
>>>           result.append((x, prop_length))
>>>       return result
>>> result3 = cal_prop_length_gold_1(result2)

>>> def omega():
>>>      result=[]
>>>      for item in wavelength_2:
>>>          x = item #wavelength
>>>          omega = (2*np.pi*c/x)
>>>          result.append((x, omega))
>>>      return result
>>> result4 = omega()

>>> def cal_kspp_imaginary_gold_2(result4):
>>>      result=[]
>>>      loop = 0
>>>      for item in result4:
>>>          omega= item[1]
```

```python
>>>          x= item [0]
>>>          kspp_imaginary= (omega/c)*(np.sqrt((( E_gold_real_2[loop]*
   E_air)/(E_gold_real_2[loop]+E_air)))**(3/2))*(E_gold_imaginary_2[loop
   ]/(2*(E_gold_real_2[loop]**2)))
>>>          result.append((omega, kspp_imaginary))
>>>          loop += 1
>>>     return result
>>> result5 = cal_kspp_imaginary_gold_2(result4)

>>> def cal_prop_length_gold_2(result5):
>>>     result =[]
>>>     for position, item in enumerate(result5):
>>>          kspp_imaginary= item[1]
>>>          x= result4[position][0]
>>>          prop_length = (1/(2*kspp_imaginary))/1000
>>>          print x, prop_length
>>>          result.append((x, prop_length))
>>>     return result
>>> result6 = cal_prop_length_gold_2(result5)

>>> def omega():
>>>     result =[]
>>>     for item in wavelength_3:
>>>          x = item #wavelength
>>>          omega = (2*np.pi*c/x)
>>>          result.append((x, omega))
>>>     return result
>>> result7 = omega()

>>> def cal_kspp_imaginary_gold_3(result7):
>>>     result =[]
>>>     loop = 0
>>>     for item in result7:
>>>          omega= item[1]
>>>          x= item[0] #wavelength
>>>          kspp_imaginary= (omega/c)*(np.sqrt((( E_gold_real_3[loop]*
   E_air)/(E_gold_real_3[loop]+E_air)))**(3/2))*(E_gold_imaginary_3[loop
   ]/(2*(E_gold_real_3[loop]**2)))
>>>          result.append((omega, kspp_imaginary))
>>>          loop += 1
>>>     return result
>>> result8 = cal_kspp_imaginary_gold_3(result7)

>>> def cal_prop_length_gold_3(result8):
```

```
>>>        result =[]
>>>        for position , item in enumerate(result8):
>>>            kspp_imaginary= item[1]
>>>            x= result7[position][0]
>>>            prop_length = (1/(2*kspp_imaginary))/1000
>>>            print x, prop_length
>>>            result.append((x, prop_length))
>>>        return result
>>> result9 = cal_prop_length_gold_3(result8)

>>> x1 = [item[0] for item in result3]
>>> y1 = [item[1] for item in result3]
>>> x2 = [item[0] for item in result6]
>>> y2 = [item[1] for item in result6]
>>> x3 = [item[0] for item in result9]
>>> y3 = [item[1] for item in result9]
>>> plt.xlim([500, 900])
>>> plt.ylim([1, 100])
>>> plt.plot(x1,y1,'bo—', linewidth=3,label ='Johnson_&_Christy')
>>> plt.plot(x2,y2,'r—', linewidth=3,label ='Palik')
>>> plt.plot(x3,y3,color='darkgreen', linewidth=3,label ='Olmon_et.al')
>>> plt.xlabel('Wavelength_(nm)', **hfont)
>>> plt.ylabel('L$_{SPP}$_($\mu$m)', **hfont)
>>> plt.gcf().subplots_adjust(bottom=0.15)

>>> plt.legend(loc='upper_left', bbox_to_anchor=(0,1), frameon=False)

>>> plt.show()
```

A.3   Python code for calculating transmittance dependence thickness of metal

The following code is an example calculation of silver. The outcome is shown in Fig. 5.3(b). Same code was used for calculating for gold (Fig. 5.3(a)), using dielectric constants [50] of gold at 600 nm.

```
>>> from __future__ import division
>>> import cmath
>>> import math
>>> from math import sin, cos, tan
>>> import numpy as np
>>> import scipy as sp
```

```python
>>> import matplotlib.pyplot as plt

>>> n1 = 1.0
>>> n3 = 1.52
>>> n2 = 0.055159 + 4.0097j #for_silver
>>> x = 600 #chosen_wavelength_in_nm
>>> P_degree = 0
>>> P_radians = (P_degree)*math.pi/180 #angle of incidence in radians

>>> def reflectance_p_12(n1, n2):
>>>     Q1 = np.cos(P_radians)
>>>     Q2 = np.cos(sp.arcsin(np.real_if_close(n1/n2*np.sin(P_radians))))
>>>     r_p_12 = ((n2*Q1)-(n1*Q2))/((n2*Q1)+(n1*Q2))
>>>     print r_p_12
>>>     return r_p_12
>>> result1 = reflectance_p_12(n1, n2)

>>> def reflectance_p_23(n2, n3):
>>>     Q2_1 = sp.arcsin(np.real_if_close(n1/n2*np.sin(P_radians)))
>>>     Q2 = np.cos(Q2_1)
>>>     Q3 = np.cos(sp.arcsin(np.real_if_close(n2/n3*np.sin(Q2_1))))
>>>     r_p_23 = ((n3*Q2)-(n2*Q3))/((n3*Q2)+(n2*Q3))
>>>     print r_p_23
>>>     return r_p_23
>>> result2 = reflectance_p_23(n2, n3)

>>> def transmittance_p_12(n1, n2):
>>>     Q1 = np.cos(P_radians)
>>>     Q2 = np.cos(sp.arcsin(np.real_if_close(n1/n2*np.sin(P_radians))))
>>>     t_p_12 = 2*n1*Q1/((n1*Q2)+(n2*Q1))
>>>     print t_p_12
>>>     return t_p_12
>>> result3 = transmittance_p_12(n1, n2)

>>> def transmittance_p_23(n2, n3):
>>>     Q2_1 = sp.arcsin(np.real_if_close(n1/n2*np.sin(P_radians)))
>>>     Q2 = np.cos(Q2_1)
>>>     Q3 = np.cos(sp.arcsin(np.real_if_close(n2/n3*np.sin(Q2_1))))
>>>     t_p_23 = 2*n2*Q2/((n2*Q3)+(n3*Q2))
>>>     print t_p_23
>>>     return t_p_23
>>> result4 = transmittance_p_23(n2, n3)
```

```
>>> def calculate_thickness_phase():
>>>     result = []
>>>     for d in range(1, 200, 1):
>>>         Q2_1 = sp.arcsin(np.real_if_close(n1/n2*np.sin(P_radians)))
>>>         Q2 = np.cos(Q2_1)
>>>         B = (2*np.pi*d*n2*Q2)/(x)
>>>         print B
>>>         result.append((d, B))
>>>     return result
>>> result5 = calculate_thickness_phase()


>>> def transmittance_coeff(): #r
>>>     result = []
>>>     for item in result5:
>>>         position = item[0]
>>>         B = item[1]
>>>         t_p_12 = result3
>>>         t_p_23 = result4
>>>         r_p_12 = result1
>>>         r_p_23 = result2
>>>         t = (t_p_12*t_p_23*np.exp(B*1j))/(1+(r_p_12*r_p_23*np.exp(B
   *2j)))
>>>         print ('The transmittance coefficient is', t)
>>>         result.append((position, t))
>>>     return result
>>> result6 = transmittance_coeff()


>>> def calculate_total_transmittance(n1, n3):
>>>     result = []
>>>     for position, item in enumerate(result6):
>>>         B = item[0]
>>>         t = item[1]
>>>         d = result5[position][0]
>>>         Q1 = np.cos(P_radians)
>>>         Q2_1 = sp.arcsin(np.real_if_close(n1/n2*np.sin(P_radians)))
>>>         Q3 = np.cos(sp.arcsin(np.real_if_close(n2/n3*np.sin(Q2_1))))
>>>         T = (((abs(t))**2)*((np.conjugate(n3)*Q3)/(np.conjugate(n1)*
   Q1)))*100
>>>         print ('The total transmittance at %s nm is %s' %(d, T))
>>>         result.append((B, T))
>>>     return result
>>> result7 = calculate_total_transmittance(n1, n3)
```

```
>>> x = [item[0] for item in result7]
>>> y = [item[1] for item in result7]
>>> plt.xlim([0, 100])
>>> plt.ylim([1, 100])
>>> plt.plot(x,y, color='darkgrey', linewidth=5)
>>> plt.xlabel('Thickness[nm]')
>>> plt.ylabel('Transmittance[%]')
>>> plt.grid()
>>> plt.show()
```

A.4   Chemicals for Au^F synthesis

Table A.2 Chemicals required for the atomically flat crystalline gold flakes

Chemicals	Specialty Companies
Gold(III)chloride hydrate (> 49 % Au basis)	Sigma Aldrich
Ethylene glycol (99 %)	ABCR
Aniline (99.5%)	Sigma Aldrich
Acetone (99 %),	Sigma Aldrich

Appendix B

Semiconductor Nanoparticles

B.1 Atomic absorption spectroscopy

Atomic absorption spectroscopy: The Cd ion concentration of the samples was determined by atomic absorption spectroscopic technique. Briefly, in a 3 mL glass vile, 100 μL of the samples were digested with aqua regia (50 μL of HNO3 and 150 μL of HCl) and finally dissolved in 50 mL deionised water in a volumetric flask. The measurements were carried out using a Varian AA- 140 Atomic Absorption Spectrometer. A calibration curve was obtained using a series of standard aqueous solutions of cadmium ranging from 0 to 2.5 ppm. Cd ion concentrations of the samples were determined from the calibration curve.

B.2 Optical characterisations

The absorbance spectra were measured using an Agilent Cary 5000 absorption spectrophotometer in transmission mode. The photoluminescence emission spectra of the samples were recorded using a Horiba Fluoromax-4 spectrometer. The photoluminescence quantum yield (PLQYs in absolute mode) of the samples in solution was measured with a Horiba-DUAL FL spectrophotometer equipped with a Quanta-ϕ integrating sphere (Horiba). All the absorbance and emission spectra of the samples were measured in a 1 cm quartz cuvette using hexane, toluene (UV-vis spectroscopy grade).

Table B.1 Chemicals required for the semiconductor nanoparticles

Chemicals	Specialty Companies
Cadmium oxide (CdO,99.99%)	Alfa Aesar
selenium powder 200 mesh (99.999%)	Alfa Aesar
Tri-n-octylphosphine oxide (TOPO,99%)	ABCR
Tri-n-octylphosphine (TOP,97%)	ABCR
Cadmium acetate dihydrate (Cd$(OAc)_2$.2H_2O,98.0%)	Sigma Aldrich
Cadmium nitrate tetrahydrate (Cd$(NO_3)_2$.4H_2O,99.99%)	Sigma Aldrich
Sulfur powder (S,99.98%)	Sigma Aldrich
Sodium myristate (>99%)	Sigma Aldrich
Hexamethyldisilazane (99%)	Sigma Aldrich
Hexadecylamine (95%)	Sigma Aldrich
1-Octadecene (ODE, 90%)	Sigma Aldrich
Oleic acid (90%)	Sigma Aldrich
Tributylphosphine (TBP, 97%)	Sigma Aldrich
Ethanol (99.5%)	Sigma Aldrich
Toluene (99.7%)	Sigma Aldrich
n-hexane (>99%)	Sigma Aldrich
Acetone (>99%)	Sigma Aldrich
Octadecylphosphonic acid (ODPA, 99%)	PCI Synthesis
Hexylphosphonic acid (HPA, 99%)	PCI Synthesis
Nitric acid (>69%)	Fluka
Hydrochloric acid (>37%)	Fluka

HERZLICHEN DANK!
THANK YOU!
धन्यवाद!

Completing this PhD has been an incredibly thrilling experience for me and it would not have been possible without the support and guidance from many wonderful people.

- Prof. Dr. Boris N. Chichkov for giving me an opportunity to carry out my research at Laser Zentrum Hannover e.V. and Prof. Dr. Birgit Glasmacher for accepting me as a PhD student.

- Dr. Carsten Reinhardt for his innovative ideas and Dr. Laszlo Sajti for his overwhelming support and discussion, specially helping me done with this thesis.

- Hannover School for Nanotechnology for financial support.

- Dr. Tobias Birr for his enormous time, support, and for being an amazing friend, Dr. Urs Zywietz, Lei Zheng and Tim Fischer for great discussion in scientific and non-scientific fields, especially for being great friends, and Rüvan Dryers for his support during my early days in Germany and great football discussion.

- Dr. Andrey B. Evlyukhin for helping me in paper writing and reviewing my thesis, and Ayman El-Tamer, Kestutis Kuršelis, Dr. Roman Kiyan for great technical discussion.

- Dr. Ulf Hinze for an opportunity to present my results in weekly seminar, and Dr. Elena Fadeeva for being a great office mate and motivating me all the time.

- Dr. Dirk Dorfs, Dr. Nadia C. Bigall, Dominik Henrichs and Dr. Suraj Naskar from the Institute of Physical Chemistry and Electrochemistry in the Leibniz Universität Hannover for fruitful co-operation.

- My parents Tul Chhantyal and Pharam Chhantyal, my brother Jiwan Chhantyal and sister-in-law Amrita Chhantyal with our little princess Jasina Chhantyal, and my younger brother Binod Chhantyal for your incredible support.

- Last but not least, to Nar Kumar Chhantyal, thank you for being so understanding and supporting me actively in my work, and for our marvellous life together in Germany.

Curriculum Vitae

Parva Chhantyal, M.Eng.

▬▬▬ Personal Information

Address: Herrenhäuser Str. 79, 30419, Hannover, Germany
Date of Birth: 7th August 1986
Nationality: British

▬▬▬ Education

10/2013– **PhD in Nanotechnology, Mechanical Engineering**, *Laser Zentrum Hannover e.V.,*
Now *Germany.*

09/2009– **MEng Chemical Engineering with Energy and Environment**, *The University of Manch-*
07/2013 *ester, UK .*

▬▬▬ List of Publications

P. Chhantyal, S. Naskar, T. Birr, T. Fischer, B. N. Chichkov, D. Dorfs, N. C. Bigall, and C. Reinhardt, 'Low Threshold Room Temperature Amplified Spontaneous Emission in 1D, 2D and 3D Quantum Confined Systems' (Submitted)

P. Chhantyal, T. Birr, D. Hinrichs, U. Zywietz, D. Dorfs, B. Glasmacher, A. B. Evlyukhin, and C. Reinhardt, 'Influence of fabrication methods of gold and silver layers on surface plasmon polaritons propagation length', Plasmonics, 2017

T. Birr, U. Zywietz, T. Fischer, P. Chhantyal, A. B. Evlyukhin, B. N. Chichkov, and C. Reinhardt, 'Ultrafast surface plasmon-polariton interference and switching in multiple crossing dielectric waveguides', Applied Physics B, vol. 122, no. 6, pp. 1-9, 2016

T. Birr, U. Zywietz, P. Chhantyal, B. N. Chichkov, and C. Reinhardt, 'Ultrafast surface plasmon-polariton logic gates and half-adder', Optics express, vol. 23, no. 25, pp. 31755-31765, 2015.

▬▬▬ Oral Presentations at Conferences

(1) 'Understanding the Propagation of Surface Plasmon-polaritons on Metallic Films', PIERS 2017, St. Petersburg, Russia.

(2) 'Investigating the influence of quantum nanoparticles in polymer waveguide', NanoDay 2016, Hannover, Germany.

(3) 'Quantum nanoparticles doped polymer waveguides for light propagation', Polymer 2016, New Orleans, USA.

(4) 'Quantum nanoparticles doped polymer waveguides for light propagation', Junior EUROMAT 2016, Lausanne, Switzerland.